U. S. DEPARTMENT OF COMMERCE
W. Averell Harriman, Secretary
NATIONAL BUREAU OF STANDARDS
E. U. Condon, Director

MAY 1948
VOLUME • 40
NUMBER 5

JOURNAL OF RESEARCH

of the

NATIONAL BUREAU OF STANDARDS

Contents

RP		Page
1879	Measurement of the slipperiness of walkway surfaces. Percy A. Sigler, Martin N. Geib, and Thomas H. Boone. (Price 10 cents)	339
1880	Perforated cover plates for steel columns: Summary of compressive properties. Ambrose H. Stang and Martin Greenspan. (Price 10 cents)	347
1881	Changes in the indices of refraction and liquidus of a barium crown glass produced by the partial substitution of some oxides. Edgar H. Hamilton, Oscar H. Grauer, Zeno Zabowsky, and C. H. Hahner. (Price 10 cents)	361
1882	Influence of low temperatures on the mechanical properties of 18:8 chromium-nickel steel. D. J. McAdams, Jr., G. W. Geil, and Frances Jane Cromwell. (Price 15 cents)	375
1883	Absorption of X-rays in air. Frank H. Day and Lauriston S. Taylor. (Price 10 cents)	393
1884	Location of the galvanometer branch for maximum sensitivity of the Wheatstone bridge. F. Ralph Kotter. (Price 10 cents)	401
1885	Second dissociation constant of oxalic acid from 0° to 50° C, and the pH of certain oxalate buffer solutions. Gladys D. Pinching and Roger G. Bates. (Price 10 cents)	405
1886	Pyrolytic fractionation of polystyrene in a high vacuum and mass spectrometer analysis of some of the fractions. Samuel L. Madorsky and Sidney Straus. (Price 10 cents)	417

For sale by the Superintendent of Documents, U. S. Government Printing Office, Washington 25, D. C. - Price 50 cents
$4.50 per year on subscription

UNITED STATES GOVERNMENT PRINTING OFFICE, WASHINGTON : 1948

U. S. Department of Commerce
National Bureau of Standards

Research Paper RP1879
Volume 40, May 1948

Part of the Journal of Research of the National Bureau of Standards

Measurement of the Slipperiness of Walkway Surfaces

By Percy A. Sigler, Martin N. Geib, and Thomas H. Boone

The establishment of a safety code for walkway surfaces has been materially handicapped by the lack of an adequate method of measuring slipperiness. The mechanics of walking as related to slipping and the design of testing instruments are briefly discussed. In order to test floors in actual service a portable slipperiness tester of the pendulum-impact type was designed and constructed. The design is based on the premise that, in the process of ordinary walking, slipping is most likely to occur when the walkway surface is first contacted by the edge of the heel. The instrument and test procedure are described. The effects of varying some of the constants of the instrument, such as the angle of contact between the test heel and the walkway surface, and the pressure between the heel and the walkway, are discussed. Typical results obtained with both rubber and leather test heels and under both dry and wet conditions are given for various flooring and finishing materials.

In general, the traction furnished by dry rubber heels is much better than that obtained with dry leather heels. Many walkway surfaces are hazardous when wet. Good antislip properties under wet conditions are usually associated with rough particles that project through the film of water and thus prevent its action as a lubricant.

I. Introduction

Slippery walkway surfaces are responsible for a large number of serious injures and accidental deaths each year. Haste and carelessness on the part of the users are frequently contributing factors. A survey of accidents in a large Government building in Washington revealed that out of 492 "lost time" injuries reported during a 19-month period, 313, or 64 percent, were due to slips and falls on walkway surfaces. According to the safety engineer who compiled the statistics, a total of 809 slips and falls were reported during the period. Of these, 496 were recorded as "no lost time" injuries. In an endeavor to reduce the frequency of such accidents, a joint research has been undertaken by the National Safety Council and the National Bureau of Standards directed toward developing data that may be used by a representative sectional committee in the preparation of a code for safe walkway surfaces. The Council is conducting a statistical survey of accidents from falls, and the Bureau is engaged in an engineering study of both walkways and footwear materials, which are equally involved in slipping.

The establishment of a safety code for walkway surfaces has been materially handicapped by the lack of an adequate method of measuring slipperiness. The correlation between coefficients of friction as commonly measured, and slipperiness as actually experienced, is not good, especially where wet surfaces are involved. Therefore, one of the first requirements of the project was the development of a suitable instrument and method for measuring slipperiness.

A walkway surface is often thought of as having a single coefficient of friction. Such is not the case. Slipperiness is not a constant of the walkway or of the contact surface of the footwear but is a function of both surfaces and is materially affected by their condition. This would be quite evident to anyone who attempts to dance on a waxed floor with rubber-soled shoes in place of leather-soled shoes. Rubber soles snub, whereas leather soles slide readily. Whether the surfaces are clean or dirty, dry or wet, are also material factors.

II. Human Locomotion

A study of the mechanics of walking was made as an aid in the design of testing instruments.

Slow-motion pictures of people walking were taken with concealed cameras so that the subjects were unaware of being photographed and were thus likely to be walking naturally. These pictures reveal that the leg slows down at the termination of its swing and then appears to vault onto the walkway, the other leg being used as a pole. They also show that the foot is first placed upon the walkway at an angle so that only the rear edge of the heel contacts the walkway surface during the early stages of the retarding phase of a step. The other foot remains in contact with the walkway, thus bearing part of the vertical load, until the heel rocks forward and the foot is fully planted.

A survey of worn heels showed that maximum wear usually occurs at the outside border of the rear portion of a heel. The contour of this worn portion is generally in the form of a curve rather than a straight line.

Probable angles that heels of shoes make with a walkway surface at the first instant of contact were determined from the motion pictures and from the contour of worn heels. For 35 men's shoes, the angle of contact ranged from 11° to 32°, with an average value of 23°. For 16 women's shoes, including both high and low heels, the angle ranged from 12° to 32°, with an average value of 19°. For 38 worn heels, the maximum angle that tangents to the worn portion made with a horizontal plane ranged from 19° to 33°, with an average value of 26°.

According to the literature,[1 2 3] the horizontal component of the force exerted by the leg on a walkway surface reaches a maximum in the forward direction shortly after the heel makes contact with the walkway, decreases rapidly at first and then slowly as the foot deploys, and rapidly reaches a maximum in the backward direction as the ball of the foot prepares to leave the walkway. These horizontal components are the forces that must be counteracted by friction in order to avoid slipping.

III. Slipperiness Tester

The location of a floor relative to exterior doors or manufacturing processes where floors are normally wet, oily, or coated with various types of waste materials determines to a large extent the texture of its worn surface and thus its slipperiness. The surface of a marble or concrete floor may become scratched and roughened to an appreciable degree from wear when located close to a street entrance, whereas the surface of a similar floor may become smooth or even glazed when located some distance from a street entrance or other source of abrasive grit.

It is extremely difficult to reproduce such a variety of surfaces by artificial means. Therefore, it is desirable that a slipperiness tester be so designed that it can be used to test floors in actual service. Such an instrument has been designed and constructed at the National Bureau of Standards (see fig. 1). The design is based on the premise that, in the process of ordinary walking, slipping is most likely to occur when the rear edge of the heel contacts the walkway surface. The instrument is similar in many respects to one previously described.[4]

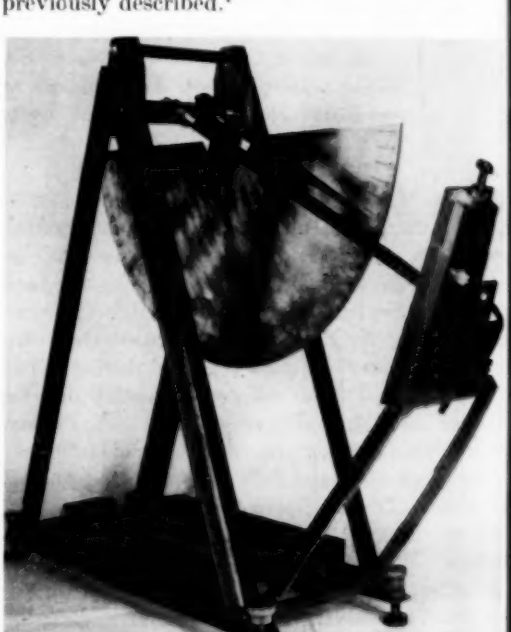

FIGURE 1. *Portable slipperiness tester of the pendulum-impact type.*

By means of a pendulum, a heel material is impacted onto and swept over the walkway surface to be tested. A mechanical heel (see fig. 2) forms

[1] Herbert Elftman, Anat. Record **59,** 481 (1934).
[2] Herbert Elftman and J. Manter, Science **88,** 152 (1938).
[3] Herbert Elftman, Arbeitsphysiol. **10,** 485 (1939).
[4] P. A. Sigler, NBS Building Materials and Structures Report BMS 10 (1943).

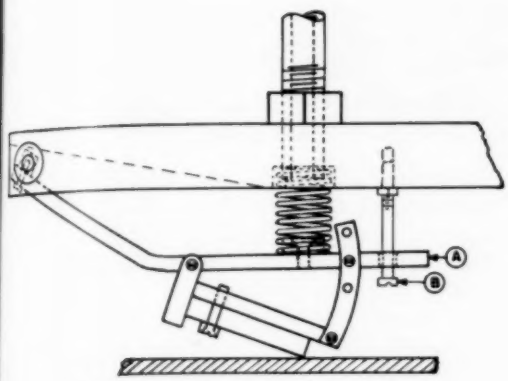

FIGURE 2. *Details of mechanical heel.*

the lower end of the pendulum and is so arranged that a 1½-in.-square test piece of rubber, leather, or other heel material can be attached to the underside at various angles so that only the rear edge of the test piece makes contact with the walkway. A helical spring is used to press the edge of the test piece against the walkway during contact. A pointer attached to the framework indicates on a scale (see fig. 1) the maximum height to which the center of gravity of the pendulum rises above its lowest (plumb) position.

Both the potential energy of the pendulum at the beginning of a swing and its residual energy at the end of a swing can be determined from the known weight and position of the center of gravity of the pendulum. The difference, or loss in energy, is equal to the work done in sliding the mechanical heel over the walkway surface, which is the average frictional force times the distance of contact. By definition the average frictional force is equal to the coefficient of friction times the average force normal to the plane of contact. From these relations an equation can be established for the coefficient of friction, or what we prefer to call the "antislip coefficient", in which all factors except the scale reading at the end of the swing are known constants of the instrument.

The values of these constants for the Bureau's instrument are the weight of the unbalanced portion of the pendulum, W=3.17 lb; the effective height of the center of gravity of the pendulum at the beginning of a swing, H=9.8 in; the distance of contact, D=3.76 in; the force pressing the edge of the heel against the walkway surface ranges from a minimum of 6.1 lb at the beginning and end of contact to a maximum of 7.4 lb at the midpoint of contact, giving an average force, P=6.75 lb.

For theoretical considerations, the average force as an arithmetical mean introduces a slight error because the variation in the force is dependent upon an arc rather than upon its subtended chord. The error has been calculated to be approximately 2 percent and does not effect the relative order of the results.

From the above relations and constants, the equation for the antislip coefficient, U, is found to be

$$U=\frac{W(H-h)}{DP}=1.244-0.125h,$$

where h is the scale reading or height of the center of gravity of the pendulum at the end of the swing when the usual contact between the mechanical heel and walkway surface is made.

In this equation, the assumption is made that during the entire distance of contact between the heel and walkway surface the variation in pressure follows a straight-line relationship. This is not strictly correct as some vibration is set up in the mechanical heel as a result of the impact on the walkway. The vibrations occur mainly during the first portion of the contact and appear to follow a similar pattern for smooth-faced materials. In view of the probable effect on the results of large differences in the amount of vibration, it is felt that the present instrument is not suited for testing very rough or embossed surfaces.

The maximum linear velocity attained by the edge of the heel from a release height of 10 in. is approximately 150 ft/min. The total weight of the instrument, including the two brass weights to keep the instrument from being displaced by the impact of the mechanical heel on the walkway, is approximately 27 lb.

IV. Test Procedure

The test procedure consists in leveling the instrument, by means of screws and a spirit level, in the direction of the swing of the pendulum and so that the edge of the heel is parallel to the walkway surface in the direction perpendicular to the swing. At the same time the edge of the heel must be adjusted to a definite height in relation to the walkway surface. The instrument itself is used to maintain this latter adjustment

constant. With a ⅛-in. spacer, placed between the hinged metal strap, *A*, and the stop, *B* (see (fig. 2), the height of the heel is adjusted so that the scale reading at the end of a swing of the pendulum, released from a scale reading of 10, is lowered by 0.1 in., that is, from 9.8 to 9.7. The normal frictional loss of the instrument, including that of the pointer, is 0.2 in. The ⅛-in. thickness was selected as a suitable control of the distance of contact. A small mirror clamped on the brace at the front of the instrument and a flashlight are used to facilitate the adjusting of the instrument when conducting tests on floors in actual service.

After the required adjustments are made, the edge of the heel material is lightly ground with No. 3/0 abrasive paper and thoroughly brushed so as to maintain it in a uniform condition. With the spacer removed, the pendulum is then released from a definite height, 10 in., and the edge of the heel permitted to sweep over the walkway surface. The height to which the center of gravity of the pendulum swings beyond a plumb position, *h* value, is used to compute the antislip coefficient. The apparatus is then moved to another location and the procedure repeated.

Tests have shown that the surface of a walkway is usually changed by repeated sweeps of the mechanical heel over the same location. In order to be able to duplicate test conditions, separate test pieces or heels are used for testing under wet conditions. The edges are lightly ground, and the test pieces immersed in water for at least ½ hr. prior to making the tests. This is particularly important for absorbent materials such as leather, as the results are influenced by the degree of wetting, being lower with increase in wetting. When testing under wet conditions, a puddle of water is maintained on the floor surface.

It is recognized that the edge of a heel may become coated with wax, dirt, oil, or other foreign material during the process of walking. Likewise, particles of grit may become embedded in the heel and the edge appreciably roughened when walking over rough surfaces. Repeated tests on a waxed asphalt tile corridor without buffing the edge of a leather test heel between sweeps of the mechanical heel showed that the results changed for the first three tests and then became relatively constant. The antislip coefficients for the latter tests were approximately 20 percent lower than for the first test and were approximately 10 percent lower than for the second test.

V. Effects of Varying Constants of the Instrument

Statistical analyses of data obtained with the instrument show that the standard deviations from the means usually range between 0.01 and 0.03. Where fairly uniform walkway surfaces are involved, representative values can be obtained by averaging the results of from three to five individual measurements for each test condition.

The effect of varying the angle of contact between the heel and the walkway surface was investigated. Angles of contact used were 10°, 20°, and 30°. In general, the antislip coefficients were found to decrease slightly with increase in the angle of contact. However, the differences in the results were too small to be considered significant, and an angle of 20° was adopted for general use.

The effect of varying the force and thus the pressure between the heel and the walkway surface was also investigated. The force normal to the walkway surface was varied by installing helical springs of different strength on the mechanical heel. The three springs used exerted an average force of 3.7, 6.7, and 11.2 lb, respectively. Although these forces may seem small, because of the small area of contact, they represent an approximate variation in pressure of from 40 to 120 lb/in^2. Significant differences in the results were observed, especially under dry conditions (see table 1). In general, lower antislip coefficients were obtained with increase in the pressure. For any given pressure, however, the antislip characteristics of the different walkway surfaces tested maintained a similar relative order. A similar tendency for the antislip coefficients to decrease with increasing pressure was also noted from a comparison of results obtained with test heels having appreciably worn and rounded edges and results obtained with test heels having unworn and square edges. Therefore, the antislip coefficients obtained by this method should be considered as relative rather than absolute values, and the establishment of a minimum antislip coefficient for walkway surfaces as a specification or code requirement would have to be based on a definite method of test.

TABLE 1. *Effect of varying the pressure between the mechanical heel and the walkway surface*

Walkway surface and test heel	Antislip coefficient with spring exerting average force of—		
	3.7 lb	6.7 lb	11.2 lb
Tennessee marble:			
Rubber heel, dry	0.81	0.75	(*)
Leather heel, dry	.46	.40	0.35
Asphalt tile:			
Rubber heel, dry	.99	.93	(*)
Leather heel, dry	.64	.56	.54
Rubber tile:			
Rubber heel, dry	.94	.81	.69
Leather heel, dry	.45	.40	.35
Rubber tile containing alundum grit:			
Rubber heel, dry	.88	.81	.69
Leather heel, dry	.52	.44	.38
Linoleum:			
Rubber heel, dry	.95	.84	.69
Leather heel, dry	.49	.39	.30
Felt-backed tile, cellulose nitrate composition:			
Rubber heel, dry	.86	.74	.60
Leather heel, dry	.41	.32	.24

* Pendulum stalled.

VI. Results and Discussion

Typical results obtained with both rubber and leather test heels and under both dry and wet conditions are given in table 2. The standard abrasion compound specified in Federal Specification ZZ–R–601a, Rubber Goods; General Specifications, was used as rubber test heels. The leather test heels conformed to Federal Specification KK–L–261b, Leather; Sole, Vegetable-Tanned, Factory.

All the walkway surfaces gave relatively high antislip coefficients with dry rubber heels, and thus good traction should be experienced with such footwear. In general, much lower coefficients were obtained with dry leather heels, the values ranging from one indicating poor traction, 0.30, to one indicating good traction, 0.50. When wet, many of the surfaces would be classed as potentially hazardous for both rubber and leather footwear. Outstanding exceptions are tests 1, 7, 8, 21, and 22 (see table 2). Good antislip properties under wet conditions are usually associated with asperities that project through the film of water and thus prevent its action as a lubricant. The asperities may represent either the roughened surfaces of the walkway or footwear materials themselves or particles of embedded sand or grit. A smooth terrazzo floor showed poor antislip properties when wet, whereas a soapstone stair tread and a rubber and cotton matting having rough surfaces showed fair antislip properties when wet (see figs. 3, 4, and 5 and tests 4, 7, and 21 in table 2).

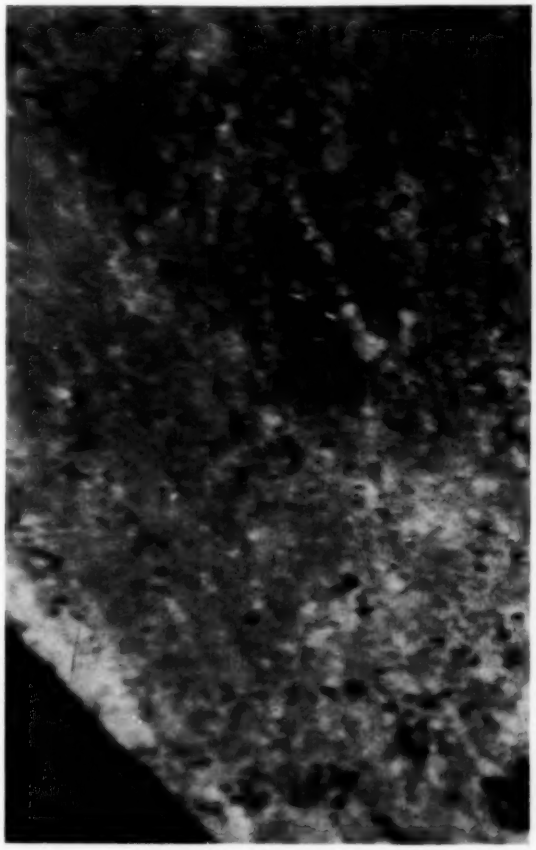

FIGURE 3. *Photomicrograph of terrazzo floor, test 4 in table 2.*

Magnification, ×30.

The results shown for the two concrete floors (tests 1 and 2) and the two vinyl resin floorings (tests 22 and 23) demonstrate the importance of surface condition and the inadvisability of assigning a single coefficient or even a single range of coefficients to one type of flooring.

The antislip properties of terrazzo were improved by the addition of an aggregate containing an abrasive (tests 4 and 5).

A waxed pressed fiberboard was considered to be exceptionally slippery by employees of the

FIGURE 4. *Photomicrograph of soapstone stair tread, test 7 in table 2.*

Magnification, ×30.

establishment where the floor was located. Measurements (test 11) substantiate their experience.

Tests 12 to 15 are representative of a series of tests on panels of brown battleship linoleum treated with different types and brands of floor waxes. Although the tests were made on an actual installation of linoleum, the area was used primarily for test purposes and had been subjected to very little traffic. Thus, the linoleum still retained most of its factory-applied coatings of sealer and wax. The antislip characteristics of the various test panels were found to be quite similar. The lowest antislip coefficient under dry conditions was obtained with a leather heel on the panel treated with a solvent-type wax (text 13). Machine polishing the panels treated with a water-emulsion wax caused a slight increase in the coefficients (tests 14 and 15). A similar tendency was found for other brands tested. The small differences found between one-coat and three-coat applications of the water-emulsion waxes were not consistent for the different brands tested.

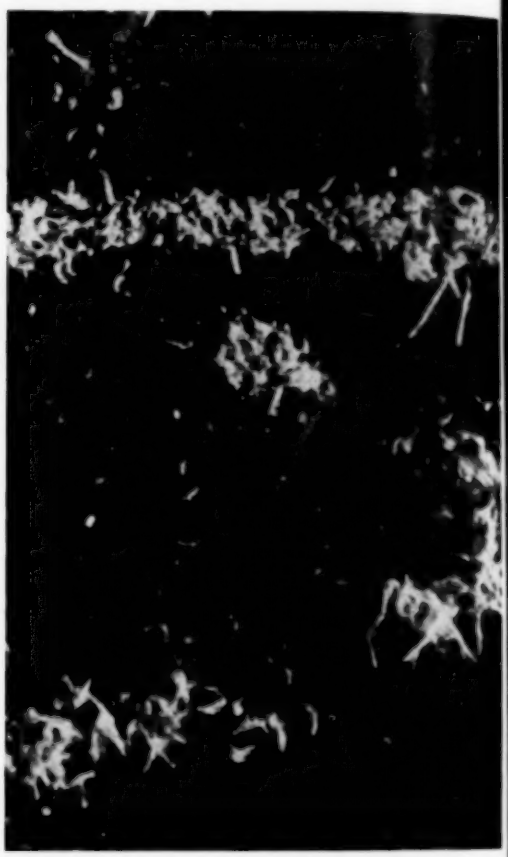

FIGURE 5. *Photomicrograph of rubber and cotton matting, test 21 in table 2.*

Magnification, ×30.

Tests 16, 18, and 19 were made on floors being maintained by a particular method and floor polish, which, according to representatives of the hospital where the tests were conducted, has resulted in a material reduction in accidents due to slippery floors. Although these floors would be considered unsafe when wet, the antislip coefficients obtained with a dry leather heel were higher than frequently found for the types of floors involved.

TABLE 2. *Relative slipperiness of a variety of walkway surfaces*

Test number	Walkway surface	Antislip coefficient			
		Rubber heel		Leather heel	
		Dry	Wet	Dry	Wet
1	Concrete slab, ground with silicon carbide [a]	0.65	0.60	0.37	0.43
2	Cement-mortar topping, worn smooth [b]	.64	.28	.37	.19
3	Paving brick, worn smooth [b]	.68	.38	.27	.27
4	Terrazzo, worn smooth [b]	.53	.25	.35	.16
5	Terrazzo, containing alundum grit, worn smooth [b]	.74	.33	.44	.18
6	Quarry tile, worn smooth [b]	.69	.28	.31	.20
7	Soapstone stair tread, sand rubbed finish [a]	.69	.59	.42	.45
8	Metal plate coated with phenolic resin and No. 46 alundum [a]	.69	.45	.64	.47
9	Yellow pine; sanded (abrasives No. 3, 1½, and 0), sealed (penetrating seal), burnished (steel wool), waxed (water-emulsion type), and polished [b]	.52	.16	.19	.16
10	White-oak, maintained with solvent-type wax (*E*), polished [b]	.49	.19	.24	.17
11	Pressed fiberboard, maintained with solvent-type wax (*E*), polished [b]	.47	.15	.26	.14
12	Linoleum (*M*), scrubbed and cleaned [a]	.68	.19	.32	.10
13	Linoleum (*M*), solvent-type wax (*F*), polished [a]	.62	.19	.25	.13
14	Linoleum (*M*), water-emulsion wax (*G*), one coat [a]:				
	Not polished	.66	.19	.28	.09
	Polished	.68	.16	.34	.11
15	Linoleum (*M*), water-emulsion wax (*G*), three coats [a]:				
	Not polished	.70	.14	.31	.07
	Polished	.71	.16	.34	.10
16	Linoleum (*N*), maintained with water-emulsion wax (*H*), polished [b]	.67	.21	.40	.20
17	Rubber tile (*O*), maintained with solvent-type wax (*E*), polished [b]	.61	.17	.29	.16
18	Rubber tile (*P*), maintained with water-emulsion wax (*H*), polished [b]	.80	.32	.42	.20
19	Asphalt tile (*R*), maintained with water-emulsion wax (*H*), polished [b]	.82	.29	.48	.24
20	Asphalt tile (*S*), maintained with water-emulsion wax (*I*), polished [b]	.76	.22	.37	.15
21	Rubber-and-cotton matting, corrugated, [c] worn rough [b]	.61	.38	.48	.32
22	Vinyl resin flooring (*T*), worn rough [b]	.59	.35	.48	.30
23	Vinyl resin flooring (*U*), smooth molded surface [a]	.47	.22	.25	.21

[a] Laboratory specimens in an unworn condition.
[b] Floor areas in actual service.
[c] Tested parallel to corrugations.

A summary of the results of a rather extensive investigation of untreated and waxed asphalt-tile corridors in a large Government building in Washington is presented graphically in figure 6. Approximately 800 measurements were involved, with the standard deviations [5] from the means averaging about 0.02. The tests were made on four different corridors. The floor area of each corridor was approximately 5,200 ft², and thus, measurements could be made at widely spaced, random locations. Each corridor was thoroughly scrubbed and cleaned at night by the building maintenance crew so as to remove surface coatings. Slipperiness tests were made the following day on each of the cleaned corridors with both rubber and leather test heels and under both dry and wet conditions.

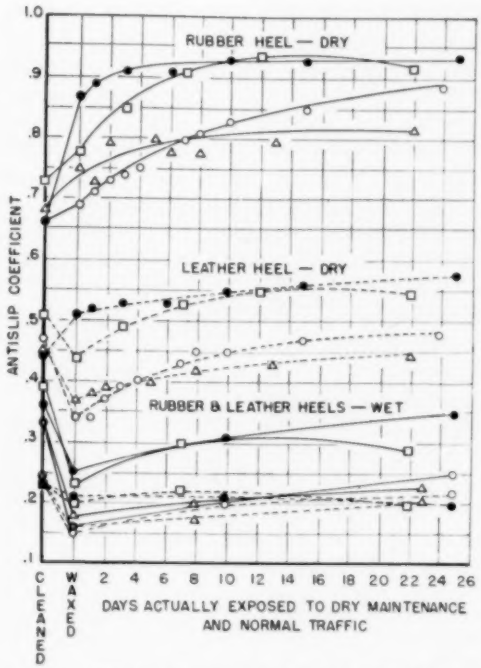

FIGURE 6. *Relative slipperiness of untreated and variously waxed asphalt tile corridors.*

—, Rubber heel; ·····, leather heel; ○, wax A; △, wax B; ●, wax C; □, wax D.

Each corridor was then given a specific waxing treatment at night and again tested the following day. All of the waxes were of the water-emulsion type. Two coats of waxes *A*, *B*, and *C* were applied and the floors machine polished after each coat. Three coats of wax *D* were applied and the floor machine polished only after the last coat.

Measurements were repeated on each of the corridors at various time intervals in order to determine what changes occurred in the slipperiness of the waxed floors when exposed to normal maintenance and traffic. The maintenance consisted in dry bushing and machine polishing the floors at the end of each work day. In figure 6, only work days were counted as days of exposure.

[5] Statistical measure of scattering.

781956—48——2

The relative order of the antislip coefficients obtained with the pendulum, impact-type slipperiness tester for the different corridors correlated very well with their relative slipperiness as actually experienced. Two of the asphalt tile corridors when freshly waxed (waxes *A* and *B*) were decidedly slippery to leather footwear, even when dry. One (wax *A*) became definitely less slippery with time, whereas the other (wax *B*) improved only slightly. Under dry conditions, the antislip properties of the other two corridors when freshly waxed (waxes *C* and *D*) were satisfactory with leather footwear. All the corridors when dry gave very good traction with rubber footwear both before and after waxing.

Higher antislip coefficients were obtained for the waxed asphalt tiles than for the untreated tiles when tested with a rubber heel under dry conditions. With a leather heel the opposite was found except for one wax (wax *C*). Under wet conditions all of the corridors would be considered hazardous for both rubber and leather footwear and especially so when waxed.

In general, the antislip properties of the waxed asphalt tile corridors improved with continued exposure to dry maintenance and normal traffic. Measurements made on the corridors after they were scrubbed with plain water and machine polished were too varied to warrant any generalized conclusions.

The results of these tests, considered in relation to slipperiness as actually experienced, indicate that a slippery condition does or does not exist, according to whether the measured coefficient is less or greater than 0.4.

Slipperiness measurements, although significant, may not in themselves afford an adequate basis for selecting the most satisfactory commercial floor treatment. Other factors, such as durability, appearance, ease, and cost of maintenance, and the requirements of existing specifications, would also need to be considered in determining the suitability of any floor finish.

WASHINGTON, August 17, 1947.

U. S. Department of Commerce
National Bureau of Standards

Research Paper RP1880
Volume 40, May 1948

Part of the Journal of Research of the National Bureau of Standards

Perforated Cover Plates for Steel Columns: Summary of Compressive Properties

By Ambrose H. Stang and Martin Greenspan

Eighty-eight steel perforated cover plate columns have been tested in the elastic range. The experimental axial rigidity under compressive load of the uniformally perforated lengths has been compared with theoretical values. The agreement in general was very good.

The distribution of stress on the edge of the perforation of these columns was also measured. The maximum values of stress concentration found experimentally have been compared with theoretical values obtained for a single hole in a large plate. These experimental values also in general agreed with the theoretical values.

The values of the average stress on the net area for the compressive tests to destruction of 28 perforated plate columns were in nearly all cases greater than the maximum stress at failure for columns of the same size having solid plates.

I. Introduction

This paper summarizes the results of compressive tests of steel colums having perforated cover plates. Tests have been made of perforated plate columns with perforations of the following shapes: Circular, ovaloid with the load parallel to the long axis, ovaloid with the load parallel to the short axis, elliptical with the load parallel to the major axis, "square" with the load parallel to two sides, and "square" with the load parallel to a diagonal.

In this paper, the ovaloid perforations were those having the shape of a square with a semicircle erected on two opposite sides; the "square" perforations were squares with rounded corners, the radius of the fillets being about 0.086 times the length of the side of the square. The expression "perforated plate" is used here for a plate having a series of similar perforations uniformly distributed along its length.

Tests in the elastic range have been made on 88 columns with perforated plates and on 17 columns with solid plates. Maximum compressive-load tests have been made on 28 columns with perforated plates and on 4 with solid plates.

The Research Paper [1] [1] containing the original program outlined the need for the tests and described the columns and the testing procedure. The results of these tests are given in four Research Papers [2]. The results of additional tests are given in two other Research Papers [3, 4]. The details of the columns have been given in those Research Papers. The essential data describing them are given in table 1.

Two papers dealing with the theoretical axial rigidity of perforated cover plate columns have been written by Martin Greenspan [5, 6]. He has also written a paper [7] on the theoretical stress distribution in a plate with a small hole. In the present paper the results of the tests in the elastic range will be compared with the theoretical values, and the results of the maximum-load tests will be discussed.

[1] Figures in brackets indicate the literature references at the end of this paper.

TABLE 1. *Description of columns*

[Nominal dimensions: Plate thickness, ¾ in. Perforations equally spaced about midheight of column]

Column designations	Number of angles	Perforation				Load parallel to—	Plate width, w
		Number	Shape	Breadth, b	Spacing, s		
				in.	*in.*		
COLUMNS 14 FT. 9 IN. LONG; ANGLES 8 BY 4 BY ½ IN.							
C1A	4 and 2	4	Circle	9.00	21.0	Diameter	20.0
C1B	4 and 2	4	do	9.00	33.0	do	20.0
C1C	4 and 2	4	do	9.00	45.0	do	20.0
C2A	4 and 2	3	Ovaloid	6.75	25.5	Long axis	15.0
C2B	4 and 2	3	do	6.75	37.5	do	15.0
C2C	4 and 2	3	do	6.75	49.5	do	15.0
C3A	4 and 2	3	do	9.00	30.0	do	20.0
C3B	4 and 2	3	do	9.00	42.0	do	20.0
C3C	4 and 2	3	do	9.00	54.0	do	20.0
C4A	4 and 2	3	do	11.50	35.0	do	25.5
C4B	4 and 2	3	do	11.50	47.0	do	25.5
C4C	4 and 2	3	do	11.50	59.0	do	25.5
C4E	2	3	do	6.50	37.0	do	25.5
C4F	2	3	do	16.50	57.0	do	25.5
C4G	2	3	Ellipse	11.50	47.0	Major axis	25.5
C4H	2	3	Ovaloid	11.50	29.75	Short axis	25.5
C4I	2	3	Square	11.50	35.5	Side	25.5
C4J	2	3	do	11.67	36.0	Diagonal	25.5
COLUMNS 10 FT. 0 IN. LONG; ANGLES 6 BY 4 BY ½ IN.							
C6	4	3	Circle	10.00	30.0	Diameter	30.0
C7	4	2	Ovaloid	10.00	44.0	Long axis	30.0

II. Axial Rigidity

The axial rigidity is described by a factor, K, defined as the ratio of the axial rigidity of a column having a perforated plate to the axial rigidity of an unperforated, but otherwise similar, column. The axial rigidity factor K is then defined so that KEA_g is the rigidity that should be used in place of EA_g in the ordinary formula for computation of the extension (or shortening) of the member. Here E is the modulus and A_g the gross area of the member.

For a column having angles and a perforated plate, the experimental axial rigidity factor is

$$K=\frac{E'_p}{E'_s} \tag{1}$$

where E'_p is the effective modulus (based on gross area) for a perforated cover plate column, and E'_s is the modulus for a solid plate column of the same gross cross-sectional area and of the same material.

The experimental axial rigidity factor K for the perforated plate by itself may be calculated from the results of the column test, as shown on p. 680 of reference [1], by the formula

$$K=\frac{E'_p}{E'_s}\left(1+\frac{A_A}{A_P}\right)-\frac{A_A}{A_P} \tag{2}$$

where A_A is the cross-sectional area of the angles and A_P the gross cross-sectional area of the perforated plate.

The theoretical axial rigidity factor K for a plate or column is given by the equation [5, 6]

$$\frac{1}{K}-1=\frac{f}{C(n)}\frac{V_o}{V_g} \tag{3}$$

where

f=a constant depending on the shape of the perforation and the direction of the applied load.

$$C(n)=1-\frac{1}{2n^2} \tag{4}$$

$n=A_g/(A_g-A_n)$, A_g being the gross and

A_n the net cross-sectional area of the member (column or plate)

V_o=the volume of the perforation

V_g=the gross volume of one bay of the member.

Values of the constant f of eq 3 for various cases are given in table 2.

TABLE 2. *Values of f in equations 3 and 5*

Perforation	Load parallel to—	f	
		eq 3	eq 5
Circle	Diameter	3.000	4.713
Ellipse, semiaxes, a and b	Major axis, a	$1+(2b/a)$	1.571 $\frac{1+2b/a}{b/a}$
Do	Minor axis, b	$1+(2a/b)$	1.571 $\frac{1+2a/b}{a/b}$
Ovaloid	Long axis	2.048	7.313
Do	Short axis	4.968	4.435
Square	Side	2.989	5.940
Do	Diagonal	3.596	3.962

The theoretical axial rigidity factor K for a perforated plate of uniform thickness (by itself and

without angles) may be derived from eq 3 and put in the form

$$\frac{1}{K}-1=f\frac{w}{s}\frac{(b/w)^2}{2-(b/w)^2}, \qquad (5)$$

where

b = perforation width
w = plate width
s = perforation spacing.

Values of the constant f of eq 5 for various cases are given in table 2.

Nomographic charts for the solution of eq 5 are shown in figure 1 for plates having ovaloid perforations, in figure 2 for plates having elliptical perforations and in figure 3 for plates having square perforations, for limited ranges of the ratios b/w and w/s.

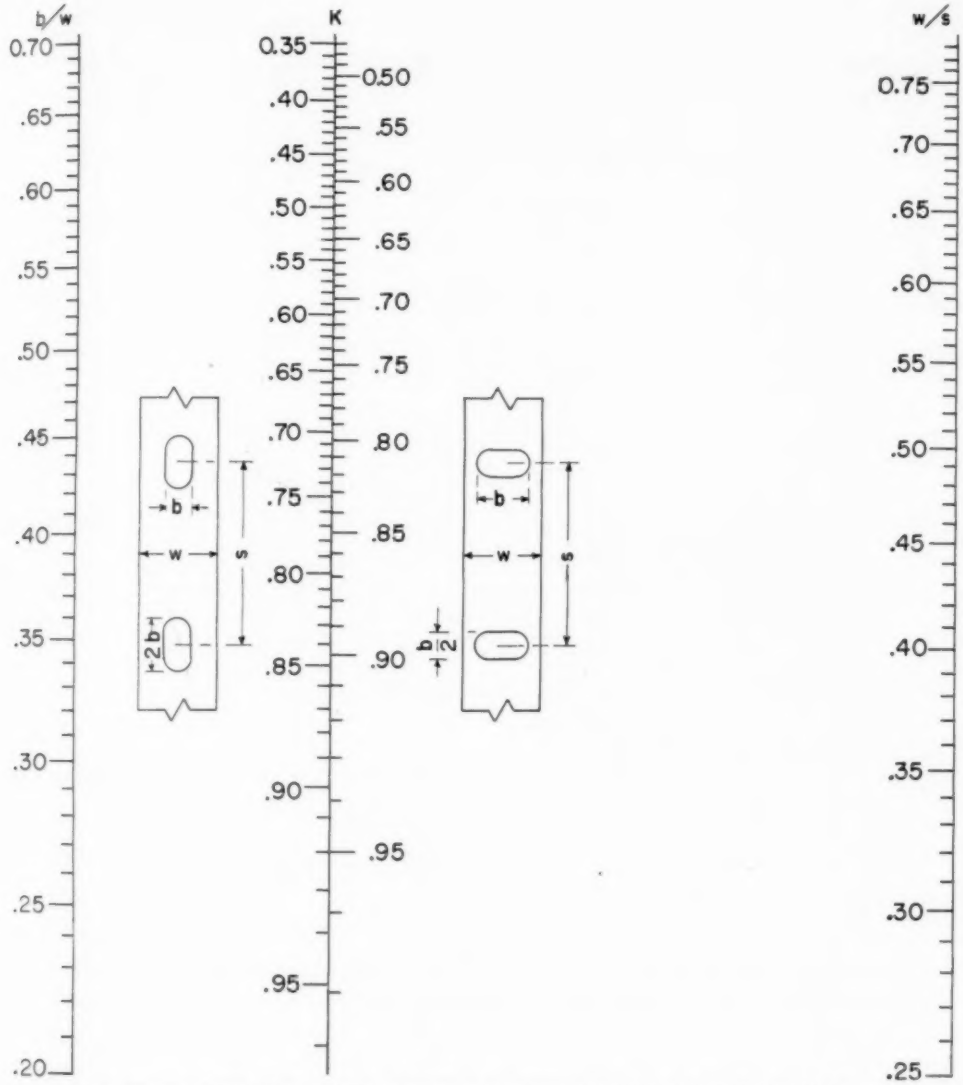

FIGURE 1. *Axial rigidity factor K of a plate of uniform thickness, having equally spaced ovaloid perforations* (eq 5). The *K*-scale at the left is for plates in which the long axis of the perforation is parallel to the direction of the load; the *K*-scale at the right for plates in which the short axis is parallel to the load. Gross area basis.

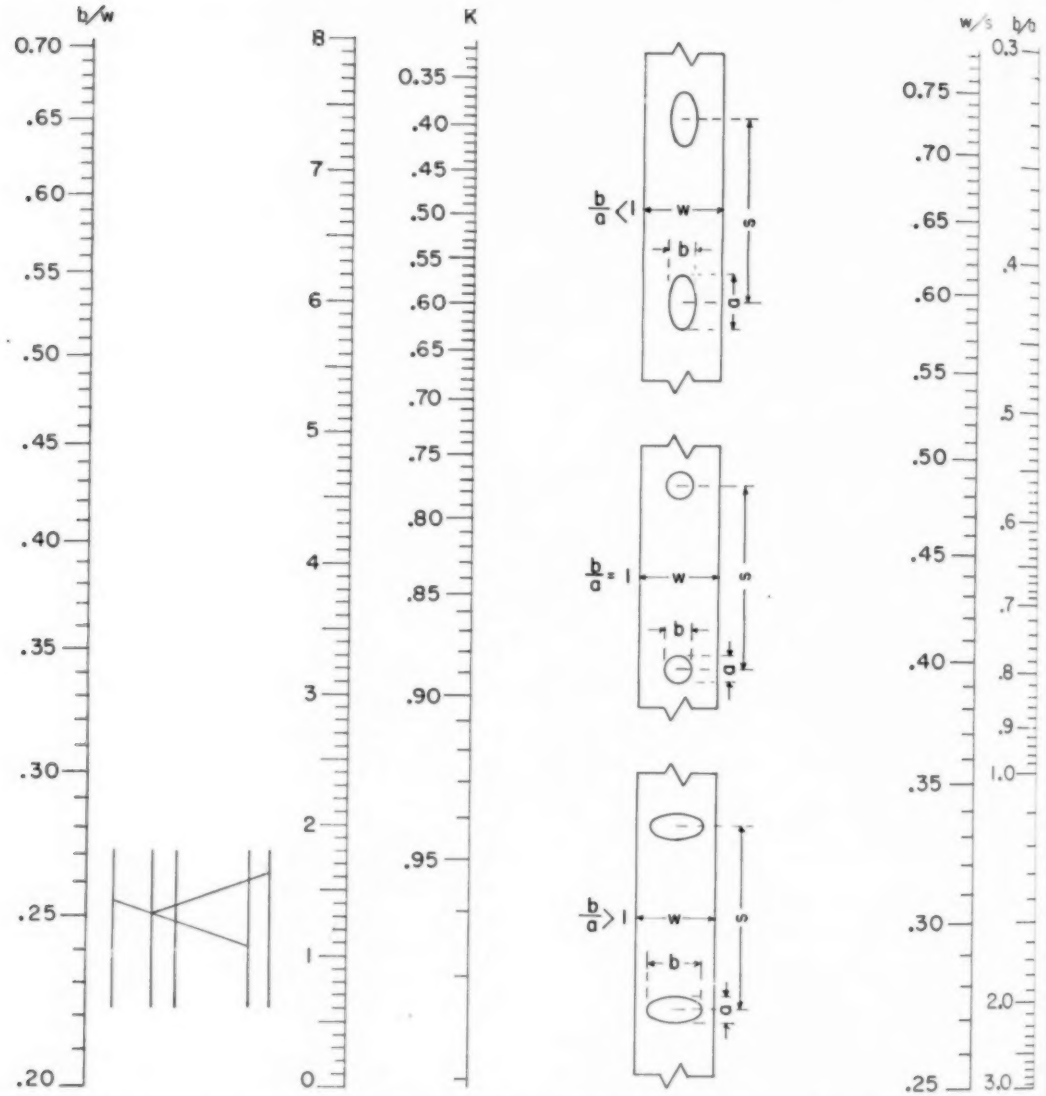

FIGURE 2. *Axial rigidity factor K of a plate of uniform thickness, having equally spaced elliptical perforations* [illegible]
Note the key near the lower left corner. Gross area basis.

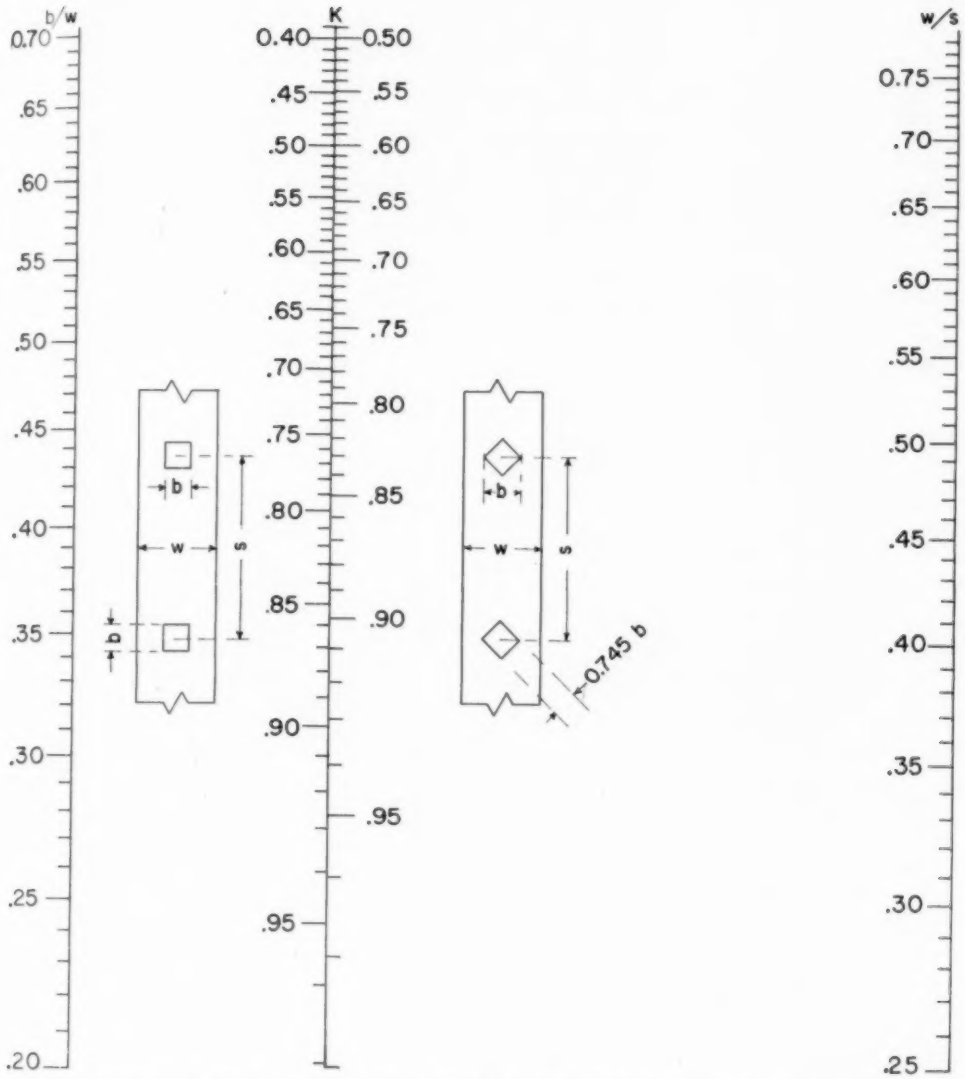

FIGURE 3. *Axial rigidity factor K of a plate of uniform thickness, having equally spaced square perforations* (eq 5).
The *K*-scale at the left is for plates in which two sides of the square are parallel to the direction of the load; the *K*-scale at the right, for plates in which diagonal of the square is parallel to the load.

TABLE 3. *Comparison of experimental and theoretical axial rigidity factors, K, for the columns and plates*

Column designation	Number of angles	See NBS Research Paper	Axial rigidity factor, K, for column				Axial rigidity factor, K, for plate			
			Experimental (eq 1)			Theoretical (eq 3)	Experimental (eq 2)			Theoretical (eq 3, 5)
PERFORATIONS, CIRCULAR										
C1A	2	RP1527	0.853	0.857	0.857	0.846	0.63	0.64	0.64	0.66
	4	do	.908	.915	.911	.899	.62	.65	.65	.66
C1B	2	do	.887	.887	.887	.896	.71	.71	.71	.76
	4	do	.928	.928	.925	.933	.71	.72	.70	.76
C1C	2	do	.912	.912	.912	.922	.78	.77	.77	.81
	4	do	.942	.939	942	.950	.78	.76	.76	.81
C6	4	RP1540	.922	.900		.919	.80	.76		.78
PERFORATIONS, OVALOID, LOAD PARALLEL TO LONG AXIS										
C2A	2	RP1474	0.866	0.874	0.877	0.874	0.60	0.62	0.62	0.67
	4	do	.921	.928	.928	.921	.62	.65	.64	.67
C2B	2	do	.918	.918	.928	.910	.73	.75	.78	.75
	4	do	.946	.942	.946	.945	.72	.71	.73	.75
C2C	2	do	.931	.935	.938	.931	.79	.80	.81	.80
	4	do	.962	.952	.962	.958	.81	.77	.81	.81
C3A	2	RP1514	.847	.840	.843	.834	.61	.60	.60	.65
	4	do	.908	.905	.908	.891	.64	.62	.64	.65
C3B	2	do	.867	.867	.874	.876	.67	.67	.68	.72
	4	do	.918	.918	.918	.920	.68	.67	.68	.72
C3C	2	do	.880	.877	.880	.901	.70	.69	.69	.77
	4	do	.918	.925	.925	.936	.67	.70	.69	.77
C4A	2	RP1501	.826	.826	.826	.799	.62	.62	.62	.62
	4	do	.888	.892	.888	.862	.61	.63	.61	.62
C4B	2	do	.840	.837	.837	.842	.65	.64	.64	.69
	4	do	.895	.888	.892	.893	.64	.62	.63	.69
C4C	2	do	.864	.860	.857	.870	.70	.69	.69	.74
	4	do	.905	.902	.902	.913	.67	.66	.66	.74
C4E	2	RP1861	.923	.917	.924	.931	.83	.82	.83	.86
C4F	2	do	.722	.726	.727	.755	.39	.40	.40	.54
C7	4	RP1540	.906	.889		.907	.73	.71		.77
PERFORATIONS, ELLIPTICAL, LOAD PARALLEL TO MAJOR AXIS										
C4G	2	RP1861	0.838	0.836	0.836	0.861	0.64	0.64	0.64	0.72
PERFORATIONS, OVALOID, LOAD PARALLEL TO SHORT AXIS										
C4H	2	RP1861	0.839			0.848	0.65			0.70
PERFORATIONS, SQUARE, LOAD PARALLEL TO SIDE										
C4I	2	RP1861	0.828			0.833	0.63			0.68
PERFORATIONS, SQUARE, LOAD PARALLEL TO DIAGONAL										
C4J	2	RP1861	0.855			0.880	0.69			0.75

The values of the experimental and the theoretical axial rigidity factors for the columns and for the plates are given in table 3. The experimental values have been plotted against the theoretical values in figure 4 for the columns and in figure 5 for the plates. In figures 4 and 5 the shape of the perforation is indicated by the shape of the plotted symbol, and the direction of the load was parallel to the ordinates.

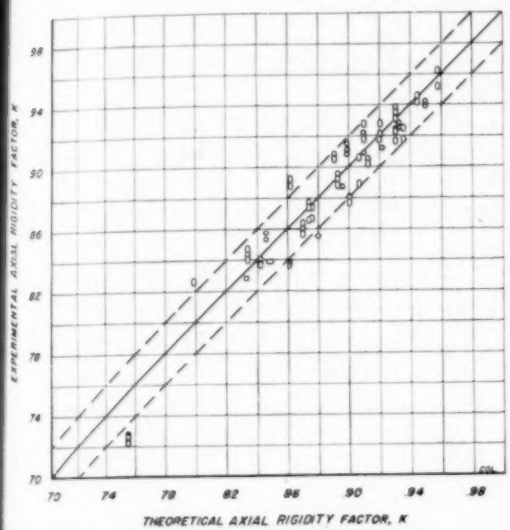

FIGURE 4. *Relation between experimental and theoretical axial rigidity factors for the columns.*

Based on gross area.

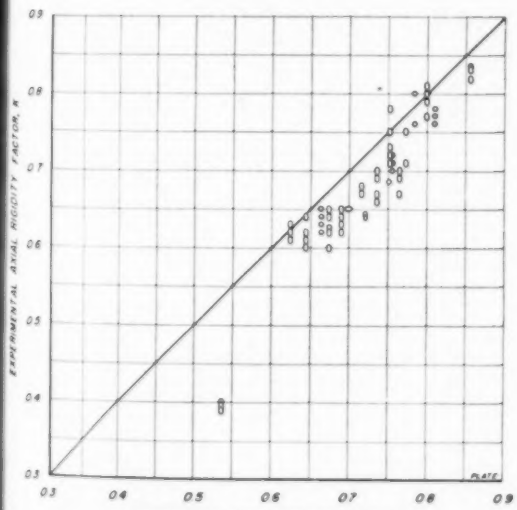

FIGURE 5. *Relation between experimental and theoretical axial rigidity factors for the perforated plates.*

Based on gross area

The experimental and theoretical values of K for the columns, figure 4 and table 3, differed by not more than ± 0.02, except for a few scattered values. Only one set of data is available for K less than 0.76.

When the perforated plates are considered, as shown in figure 5 and table 3, the agreement between experimental and theoretical values is also good, although not as good as for the complete columns. The general tendency is for the experimental values to be less than the theoretical. The difference is considerable for theoretical values of K for the plate less than about 0.55. It is probable that perforations relatively as large as these (columns C4F, reference [4]) will seldom be used in practice. The limitations of eq 3 have been discussed by Greenspan in reference [5, p. 319]. The results of these tests then show that the axial rigidity factor of columns and of perforated plates can be closely approximated by calculations according to eq 3 or 5.

III. Stresses on the Edge of the Perforation

Many theoretical studies of the influence of a perforation on the stresses in a plate loaded, say in the direction of its length, are based on the assumption that the plate width is large in comparison to the perforation width. Stresses σ at a point near the perforation are then compared with the uniform stress, S, at a large distance from the hole, generally by evaluating the ratio σ/S. In other similar studies but for a plate having a finite width and gross area A_g subjected to a load P, it has been found [6, 8] that instead of using the average stress based on gross area, P/A_g, for comparison with values derived from consideration of an infinite plate, the correction factor $C(n)$ of eq 4 should be used for the stress ratios, as $\sigma C(n)/(P/A_g)$. The value of (Cn) is unity for an infinite plate and is always less than one for a plate or column of finite cross-sectional area.

If experimental stress ratios determined for a column having a finite cross-sectional area are to be compared with theoretical values derived for an infinite plate, the observed stress ratio $\sigma_{ns}/(P/A_g)$ should be reduced in value by multiplying it by the $C(n)$ correction factor for the column, where σ_n is the maximum principal stress and σ_r the minimum principal stress.

Conversely, if the theoretical stress ratios, derived for an infinite plate, are to be compared to experimental values for a column of finite cross-sectional area, the former values should be increased by dividing them by the $C(n)$ correction factor to obtain theoretical value for a column of finite cross-sectional area, defined by $C(n)$.

The distributions of stresses on the edge of the middle perforation, averaged for all columns having perforations of the same shape and loaded in the same direction, are shown by the solid lines in figures 6, 7, 8, 9, 10, and 11. These values are based on gross area. The rectified lengths of one quadrant of the perforation boundaries were reduced to a standard length AC. Before averaging, the experimental stress ratio values were multiplied by the $C(n)$ value for the column, as given in table 4.

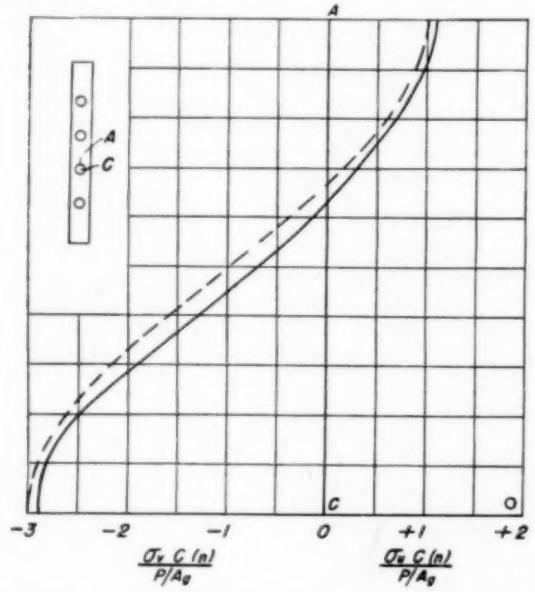

FIGURE 6. *Circular perforations; distribution of stress on the edge of the perforation.*

The solid line is the average of the experimental values multiplied by $C(n)$ for 19 columns. The dashed line represents the theoretical distribution. Based on gross area.

The dashed lines of figures 6 to 11 represent the theoretical stress distribution at the boundary of a single perforation in an infinite plate, according to the formulas of reference [7].

As the experimental stress ratios have been multiplied by the $C(n)$ correction factor, they are in effect representative of stress ratios in an

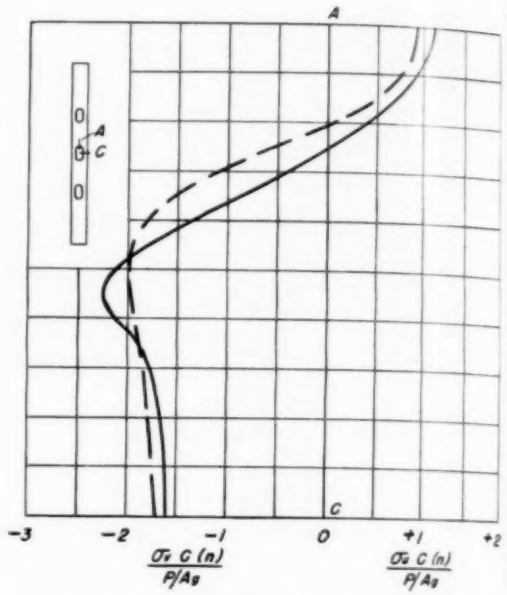

FIGURE 7. *Ovaloid perforations; load parallel to long axis; distribution of stress on the edge of the perforation.*

The solid line is the average of the experimental values multiplied by $C(n)$ for 61 columns. The dashed line represents the theoretical distribution. Based on gross area.

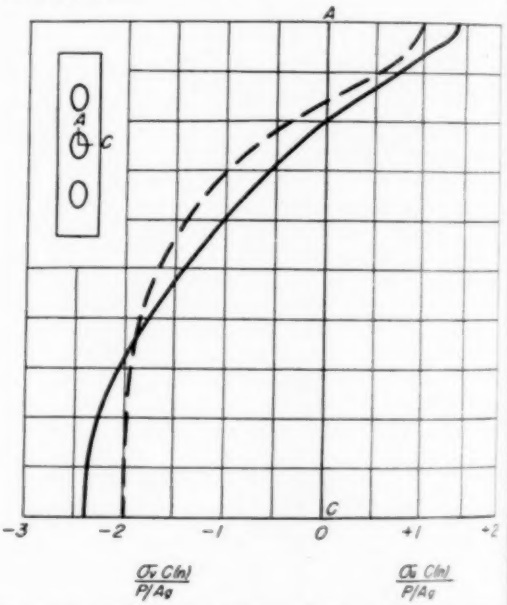

FIGURE 8. *Elliptical perforations; load parallel to major axis; distribution of stress on the edge of the perforation.*

The solid line shows the experimental values multiplied by $C(n)$ for column C4G-2. The dashed line represents the theoretical distribution. Based on gross area.

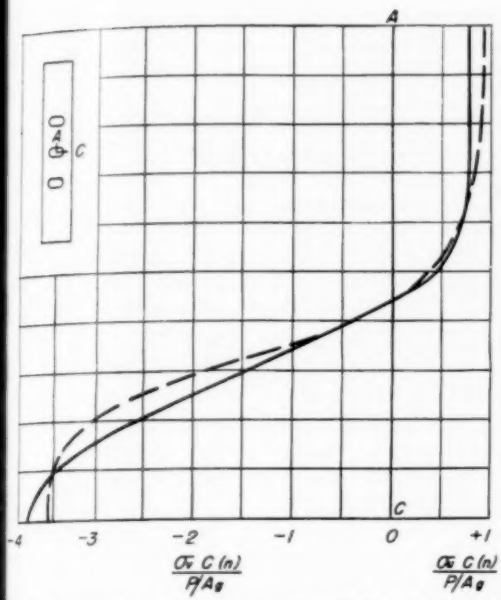

FIGURE 9. *Ovaloid perforations; load parallel to short axis; distribution of stress on the edge of the perforation.*

The solid line shows the experimental values multiplied by $C(n)$ for column C-II. The dashed line represents the theoretical distribution. Based on gross area.

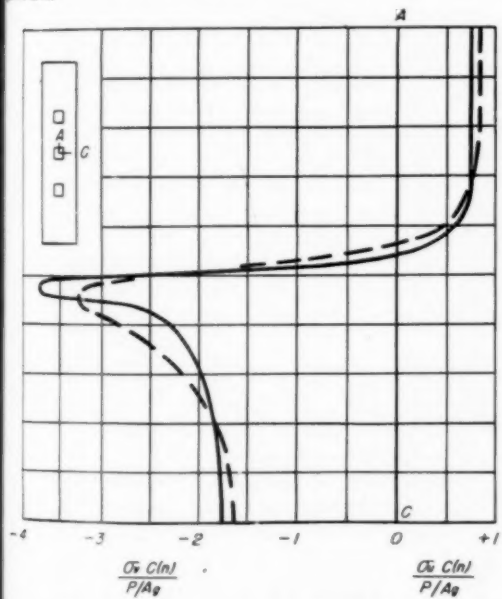

FIGURE 10. *Square perforations; load parallel to two sides; distribution of stress on the edge of the perforation.*

The solid line shows the experimental values multiplied by $C(n)$ for column C-II. The dashed line represents the theoretical distribution. Based on gross area.

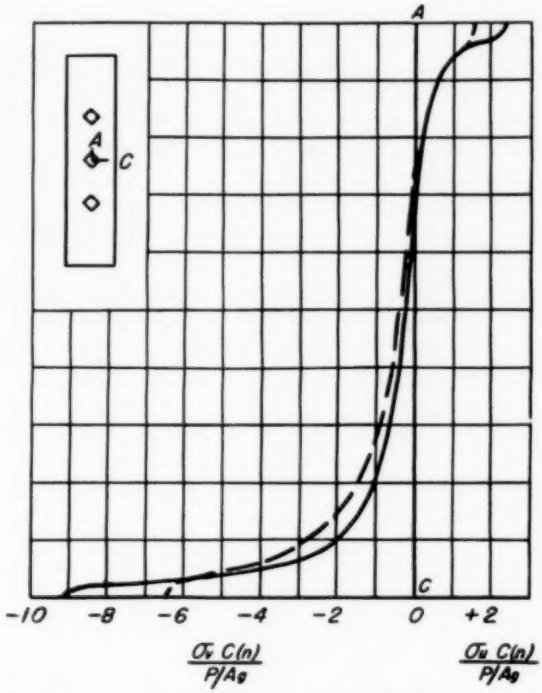

FIGURE 11. *Square perforations, load parallel to diagonal; distribution of stress on the edge of the perforation.*

The solid line shows the experimental values multiplied by $C(n)$ for column C-II. The dashed line represents the theoretical distribution. Based on gross area.

infinite plate and may be compared with the theoretical values, the derivation of which was based on the conditions in an infinite plate.

The agreement between the theoretical and experimental stress distributions on the edge of the perforation is good in all cases.

It should be noted that the theoretical stress distribution was derived by considering a plate having a single hole, and the observed stress ratios were obtained for plates having a series of equally spaced similar perforations.

It was decided to tabulate the values of the maximum stress for the perforated cover plates since they are of basic importance for structural design. The maximum stress is expressed by a "maximum stress ratio", maximum stress/(P/A_g). Values of maximum stress ratio are given in references [2, 3, 4] and in table 4 of this paper. The values based on gross area may be compared with the theoretical maximum stress ratios to be evaluated from the equations given in reference

TABLE 4. *Maximum stress concentration in the boundary of the perforation*

Column designation	Number of angles	$C(n)$	Ratio: $\frac{\text{Maximum stress}}{P/Ag}$, based on gross area					Ratio: $\frac{\text{Maximum stress}}{P/Ag}$ based on net area of experimentally tested column		
			Theoretical		Experimentally tested column					
			Infinite plate	Tested column						
PERFORATIONS—CIRCLES										
C1A, C1B, C1C	4	0.994	3.00	3.02	2.50	2.91	3.06	2.22	2.59	2.72
Do	2	.984	3.00	3.05	2.77	3.24	3.43	2.28	2.67	2.82
C6	4	.992	3.00	3.02	2.58			2.26		
PERFORATIONS—OVALOIDS, LOAD PARALLEL TO LONG AXIS										
C2A, C2B, C2C	4	0.986	1.96	1.97	2.03	2.20	2.20	1.85	2.01	2.01
Do	2	.989	1.96	1.98	2.15	2.43	2.52	1.83	2.07	2.15
C3A, C3B, C3C	4	.994	1.96	1.97	1.97	2.28	2.39	1.75	2.03	2.13
Do	2	.984	1.96	1.99	2.16	2.37	2.55	1.78	1.95	2.10
C4A, C4B, C4C	4	.991	1.96	1.98	1.98	2.27	2.43	1.72	1.97	2.11
Do	2	.979	1.96	2.00	2.24	2.63	2.48	1.78	2.09	1.97
C4E	2	.993	1.96	1.97	2.28			2.01		
C4F	2	.957	1.96	2.05	2.39			1.69		
C7	4	.992	1.96	1.98	2.18			1.91		
PERFORATIONS—OVALOIDS, LOAD PARALLEL TO SHORT AXIS										
C4H	2	0.979	3.57	3.65	3.94			3.12		
PERFORATIONS—ELLIPSES, LOAD PARALLEL TO MAJOR AXIS										
C4G	2	0.979	2.00	2.04	2.43			1.93		
PERFORATIONS—SQUARES, LOAD PARALLEL TO SIDE										
C4I	2	0.979	3.28	3.35	3.82			3.02		
PERFORATIONS—SQUARES, LOAD PARALLEL TO DIAGONAL										
C4J	2	0.978	6.45	6.60	9.10			7.41		

[7]. The theoretical maximum stress ratios are given for the columns in table 4, for both an infinite plate and for the actual column.

The three experimental maximum stress ratios given in the same line of table 4 are for columns having perforations of the same size but for increasing perforation spacings, as given in table 1. There seems to be a tendency in many cases for the experimental maximum stress ratio to increase as the perforation spacing increases.

The experimental values based on gross area are in many cases greater than the theoretical maximum stress ratios for the tested columns.

It is also interesting to compare the theoretical maximum stress ratios with the experimental values that are based on net area, even though such a comparison runs counter to some of the assumptions involved in the theoretical derivations. The values are also given in table 4. Very few of the experimental maximum stress ratios based on net area are greater than the theoretical values for the tested columns. The spread between the gross and net areas in nearly all commercial structural columns would be less than for these columns that have been tested. It would seem then that the theoretical maximum

stress ratios, determined as described above, can be safely used for designing perforated plate columns.

IV. Tests to Failure to Determine Maximum Compressive Loads

The steel columns subjected to compressive test to destruction consisted of a plate and two angles except for columns C6 and C7 [3], which had four angles. Unfortunately the C6 and C7 column series did not contain any columns with solid plates for comparison with the strengths of those perforated plate columns.

The other columns had cross-sectional shapes as shown in figure 12. The distance y_p from the the back of the plate to the center of area of the section, in the perforated portion of a column is always greater than the similar distance, y_s, for the solid portion of a perforated plate column. There is therefore a local eccentricity, $y_p - y_s$, tending to induce increased compression in the plate and to make the column fail by bending away from the plate side during a compressive load test. Tests of columns of this shape would thus be expected to give lower compressive strength values than would tests of columns of the same quality in which the perforated plates were not eccentrically loaded, as would be the case for four angle columns.

Of the four columns having two angles and a solid plate, two failed by primary buckling, bending toward the plate side as would be expected from the double modulus column theory. The other two columns began to deflect toward the plate side but finally failed by secondary buckling of the plate and deflected away from the plate side.

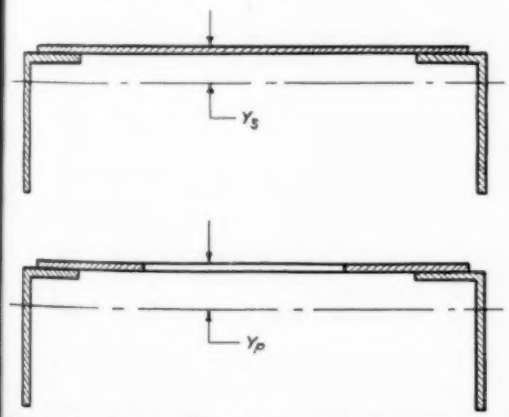

FIGURE 12. *Cross sections of columns having two angles.*

Top, the section representing a column having a solid plate or a section through the solid portion of a perforated plate column. Bottom, a section through the perforation. Eccentricity $= y_p - y_s$.

Of the 24 columns having two angles and a perforated plate, 22 failed by bending away from the plate side as would be expected from the consideration that, in the neighborhood of a perforation, the gravity axis of the columns is displaced away from the plate side. The other two columns showed practically no deflection until the maximum load was very nearly reached and then failed by bending toward the plate side.

The four columns, each having four angles and a perforated plate, all failed by buckling of the plates near one of the perforations.

The final failure of all of the columns was accompanied by local buckling of the outstanding legs of the angles, and by buckling of the plate near a perforation for the perforated plate columns as well as the general bending of the columns as a whole.

Figure 13 shows the perforated plate column C4J in the testing machine for the maximum load test.

The slenderness ratio for the solid plate columns was 70 for column C2, 71 for columns C1 and C3, and 72.5 for columns C4.

The effective area factor C of a perforated plate is a measure of the effectiveness of the plate with regard to compressive strength. It can be calculated, as shown on p. 685 of reference [1] by the formula

$$C = \frac{P_{max}}{A_p \sigma_{max}} - \frac{A_a}{A_p} \tag{6}$$

where P_{max} is the total compressive load at failure for the perforated plate column, σ_{max} is the average stress obtained by dividing the maximum compressive load on a similar solid plate column by the gross cross-sectional area, A_a the cross-sectional area of the angles and A_p the cross-sectional area of the plate. C may be taken on a gross- or on a net-area basis, depending on which value of A_p is used.

When based on net area, the value of C would be unity if the average compressive stress at failure for the perforated plate column was equal to that of a similar column having a solid plate.

Values of the effective area factor, C, for the two-angle columns are given in table 5.

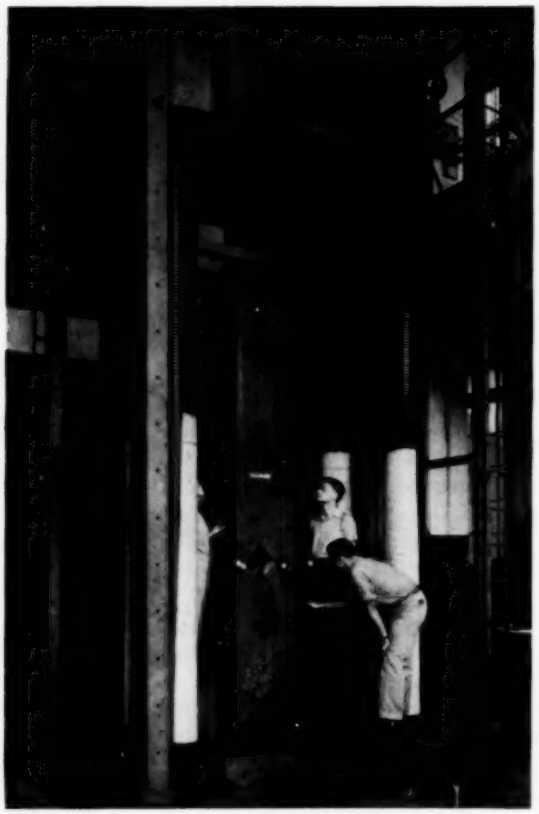

FIGURE 13. *Column C4J in the testing machine during the maximum compressive load test.*

The effective area factor C based on net area was for all but three columns greater than unity. For these C2 columns, the compressive stress at failure, based on net area, was 32.7 kips/in.^{2} for C2A; 32.3 kips/in.^{2} for C2B; and 33.3 kips/in.^{2} for C2C. The compressive stress at failure for the similar column C2D having a solid plate was 33.8 kips/in^2. The effective area factor C for columns of the size tested is evidently very sensitive to relatively small differences of compressive stress at failure.

From a consideration of these effects and of the local eccentricities present in perforated plate columns having but two angles, it seems that the net area of perforated steel plates may safely be used for design purposes. The values of table 5 show this is true for perforations of all of the shapes tested, even those having relatively great values of the maximum stress ratios.

TABLE 5. *Effective area factor, C, with respect to compressive strength for the columns*

[Each column had a perforated plate and two angles]

Column designation	Effective area factor, C	
	Based on gross area	Based on net area
PERFORATIONS—CIRCLES		
C1A	0.68	1.22
C1B	.68	1.22
C1C	.74	1.35
PERFORATIONS—OVALOIDS, LOAD PARALLEL TO LONG AXIS		
C2A	0.47	0.85
C2B	.44	.79
C2C	.52	.93
C3A	.59	1.06
C3B	.57	1.03
C3C	.64	1.16
C4A	.62	1.12
C4B	.65	1.18
C4C	.71	1.28
C4E–1	.93	1.25
C4E–2	.83	1.11
C4E–3	.91	1.21
C4F–1	.48	1.35
C4F–2	.52	1.47
C4F–3	.46	1.31
PERFORATIONS—ELLIPTICAL, LOAD PARALLEL TO MAJOR AXIS		
C4G–1	0.76	1.38
C4G–2	.72	1.31
C4G–3	.75	1.36
PERFORATIONS—OVALOID, LOAD PARALLEL TO SHORT AXIS		
C4H	0.64	1.18
PERFORATIONS—SQUARE, LOAD PARALLEL TO SIDE		
C4I	0.73	1.33
PERFORATIONS—SQUARE, LOAD PARALLEL TO DIAGONAL		
C4J	0.75	1.39

V. Summary and Conclusions

Tests in the elastic range have been made on 88 steel columns with perforated plates and on 17 steel columns with solid plates. Maximum compressive load tests have been made on 28 columns with perforated plates and on 4 with solid plates.

Theories have been derived dealing with the

axial rigidity of perforated plate columns and with the stress distribution in the neighborhood of a perforation.

Comparisons between the test results and the theoretical values lead to the conclusions that the axial rigidity is correctly defined by the theoretical eq 3 of this paper; and that the distribution of stress on the boundary of a perforation is adequately expressed by the equations of reference [7].

The results of the maximum compressive-load tests show that the net area of perforated plate columns may safely be used for estimating the strength of columns with perforated cover plates.

The tests of perforated cover plates for steel columns have been made in cooperation with the American Institute of Steel Construction, which furnished the specimens. The program was prepared by the National Bureau of Standards and by the Institute's Committee on Technical Research, which at the start of the program consisted of Comfort A. Adams, the late Otis E. Hovey, H. D. Hussey, Jonathan Jones, the late J. R. Lambert, the late L. S. Moisseiff, Walter Weiskopf, and F. H. Frankland, chairman. The committee was assisted by Shortridge Hardesty, Frank M. Masters, and Henry C. Tammen. The work was done in the Engineering Mechanics Section of the National Bureau of Standards.

The Institute has expressed no disapproval because the final tests were delayed for 4 years because of the Second World War. This forbearance has been much appreciated by the members of the staff to whom this work was assigned.

VI. References

[1] Ambrose H. Stang and Martin Greenspan, J. Research NBS **28,** 669 (1942) RP1473.

[2] Ambrose H. Stang and Martin Greenspan, J. Research NBS **28,** 687 (1942) RP1474; **29,** 279 (1942) RP1501; **30,** 15 (1943) RP1514; **30,** 177 (1943) RP1527.

[3] Ambrose H. Stang and Martin Greenspan, J. Research NBS **30,** 411 (1943) RP1540.

[4] Ambrose H. Stang and Bernard S. Jaffe, J. Research NBS **40,** 121 (1948) RP1861.

[5] Martin Greenspan, J. Research NBS **31,** 305 (1943) RP1568.

[6] Martin Greenspan, J. Research NBS **37,** 157 (1946) RP1737.

[7] Martin Greenspan, Quart. Applied Math. **2** 60 (1944).

[8] E. G. Coker and L. N. G. Filon, A treatise on photoelasticity, p. 545 (Cambridge Univ. Press, Cambridge, Eng., 1931).

WASHINGTON, November 28, 1947.

U. S. Department of Commerce
National Bureau of Standards

Research Paper RP1881
Volume 40, May 1948

Part of the Journal of Research of the National Bureau of Standards

Changes in the Indices of Refraction and Liquidus of a Barium Crown Glass Produced by the Partial Substitution of Some Oxides [1]

By Edgar H. Hamilton, Oscar H. Grauer, Zeno Zabawsky,* and C. H. Hahner

Optical glasses with high indices of refraction and Abbe values are very desirable for wide-angle lenses. In order to determine the range of compositions in which glasses of this type could be produced, oxides of Li, Be, Ca, B, La, or Th, were substituted for BaO or SiO_2 in a three- or four-component base glass. Substitutions were made on a mole-for-mole basis. The indices of refraction for the *C*, *D*, *F*, and *G'* lines and the liquidus were determined for each glass. Experimental glasses with indices of refraction (n_D) and Abbe values from 1.600 to 1.714 and 62.2 to 52.7, respectively, were made in small platinum crucibles.

I. Introduction

Previous to 1880, optical glasses could be divided into a few types such as crown, crown flint, and flint glasses with indices of refraction (n) and Abbe value (ν) ranging from 1.50 to 1.92 and 70 to 20, respectively. The ν value of the glasses decreased as the index of refraction increased so that, when ν is plotted against n, the points fall on a curved line. Abbe and Schott introduced a number of new types of glasses containing boron and barium oxides with ν values higher than for the old types of glasses with the same n_D. Recently G. W. Morey [2] [1] developed a number of new glasses in which the ratio of Abbe value to index of refraction is much higher than for the glasses of Abbe and Schott. This paper gives the composition, optical and other properties of some other glasses, which also have a high ratio of ν value to index of refraction. These glasses may find a use in optical instruments where a large flat field with a minimum of aberration is desired.

The oxides that gave promise of being useful in making such glasses were B_2O_3, BeO, CaO, La_2O_3, ThO_2, and Li_2O. Although glasses containing such oxides have been described in the literature [1], few systematic data are available on the effect of these oxides on the range of compositions in which glass can be produced. In this investigation one of the above oxides was substituted on a mole-for-mole basis for part of the barium oxide or silica in a base glass containing the following:

	Percent	
	Moles	Weight
SiO_2	54.0	35.5
B_2O_3	14.0	10.7
BaO	32.0	53.8

The substitutions were made in steps in order to determine the shapes of the index-of-refraction-composition and liquidus-composition curves. When glasses with desirable properties resulted, these glasses were used as base glasses for further substitutions.

II. Experimental Procedure

All melts were made in platinum crucibles 90 mm deep by 36 mm in diameter and stirred with platinum-10-percent-rhodium stirrers. Although the melts were stirred, striae-free glass could consistently be obtained only by crushing, mixing,

*Now with the Armstrong Cork Co., Lancaster, Pa.

[1] Presented at the Forty-Eighth Annual Meeting, the American Ceramic Society, Buffalo, N. Y., May 1, 1946 (Glass Division No. 13).

[2] Figures in brackets indicate the literature references at the end of the paper.

and remelting each glass.[3] A few compositions required remelting a second time to obtain glasses sufficiently free from striae to permit reliable index of refraction measurements to be made.

The presence of striae in optical glass is a very serious obstacle to the production of useful glasses. As the striae consist of local inhomogeneities in composition, any measurement on the glass that includes striae will be different in general from measurements on the rest of the glass. Even the portion of the glass that does not contain striae will have a different composition, because the striae will have removed disproportionate amounts of its constituents.

Furthermore, on annealing the glass, differences in the coefficients of expansion between the glass and striae will cause local strains and thus give rise to differences in index of refraction for different parts of the glass.

Striae have always "haunted" the optical-glass maker and have been chiefly responsible for the slow development of new optical glasses. Even at present, unless the utmost care is exercised in procedures and techniques, striae will be found in most glasses.

After the final remelting, the glass was poured into a 3-in. diameter steel mold. As soon as it solidified, it was transferred to a heated, covered clay box and placed in an electric annealing furnace. The glasses were cooled through their annealing ranges at approximately 5 deg C per hour.

The indices of refraction of the glasses were determined for the *C*, *D*, *F*, and *G'* lines by the Pulfrich method.[4] The maximum error of a single determination should not exceed ± 0.0001.

For the glasses that were analyzed, it was found that except for a few glasses the difference between the analyzed and batch compositions did not exceed 0.3 mole percent. The calculated compositions are given in the tables, as many of the glasses have not been analyzed. In general it is believed that the calculated compositions were more accurate than those determined by chemical analysis, particularly as duplicate glasses listed in the table indicated far less difference in composition by their measured indices of refraction than by chemical analysis. For all but one set of duplicate glasses the measured indices of refraction (n_D) agreed within 0.0001.

The liquidus temperature of each glass was determined by a temperature gradient method [2]. The crystals formed in many of the glasses were very small, making it extremely difficult to determine the exact location in the specimen at which devitrification ceases. Complete identification of the crystal phases was not attempted. The appearance of a new crystalline phase at the liquidus was determined by petrographic examination. The crystallographic evidence indicates that the discontinuities found in the liquidus curves are accompanied by changes in the primary phase at the liquidus.

III. Results and Discussions

1. Substitution of Beryllium Oxide for Barium Oxide

The substitution of beryllium oxide for barium oxide produced glasses with lower indices of refraction and higher Abbe values than the base glass (table 1). No indices of refraction are given for melt 469, containing 12 mole percent of beryllium oxide, as this glass could not be cooled without devitrification.

A minimum point is indicated on the liquidus-composition curve, figure 1, near the 6-mole percent beryllium-oxide composition, and there is a definite change in slope of the index-of-refraction-composition curves near this composition. Glasses containing 6-mole percent or less of beryllium oxide produced anisotropic crystals at the liquidus; the 8-mole percent glass, isotropic crystals; the 10-mole-percent glass, a mixture of isotropic and anisotropic crystals; and the 12-mole-percent glass, anisotropic crystals.

Abbe values (ν) have been plotted on this and succeeding figures. Discontinuities are usually found on the Abbe-value-composition curves at approximately the same compositions as on the other curves for the same series of glasses. Because of the large probable error in calculating Abbe values, discontinuities on the Abbe-value-composition curves were not considered significant.

2. Substitution of Beryllium Oxide for Silica

The substitution of beryllium oxide for silica produced glasses with higher indices of refraction

[3] After most of the glasses had been made, it was found that striae-free glass could be made without remelting provided it was melted and stirred in a platinum crucible of the proper proportions. In a platinum crucible 3 in. in diameter by 3½ in. deep, 2-pound melts of striae-free glass have been made consistently.

[4] Determinations by I. Malitsky of this Bureau.

TABLE 1. *Series 1. Substitution of beryllium oxide for barium oxide*

Composition	Glass number											
	680		694		695		696		700		469	
	Mole %	*wt %*	*Mole %*	*wt %*	*Mole %*	*wt %*	*Mole %*	*wt %*	*Mole %*	*wt %*	*Mole %*	*wt %*
[illegible]O	54	35.5	54	37.6	54	38.8	54	40.0	54	41.4	54	42.8
[illegible]O	14	10.7	14	11.3	14	11.7	14	12.0	14	12.4	14	12.8
[illegible]O	32	53.8	28	49.9	26	47.7	24	45.5	22	43.0	20	40.4
BeO	0	0.0	4	1.2	6	1.8	8	2.5	10	3.2	12	4.0
INDEX OF REFRACTION												
[illegible]	1.6236		1.6145		1.6100		1.6043		1.5969		(1)	
[illegible]	1.6268		1.6176		1.6130		1.6072		1.5999		(1)	
[illegible]	1.6343		1.6249		1.6202		1.6142		1.6067		(1)	
[illegible]	1.6404		1.6307		1.6259		1.6198		1.6122		(1)	
[illegible]	58.5		59.7		60.3		61.1		61.3		(1)	
LIQUIDUS, ° C												
	1,160		1,088		1,046		1,061		1,078		1,133	

(1) This glass devitrified when cooled.

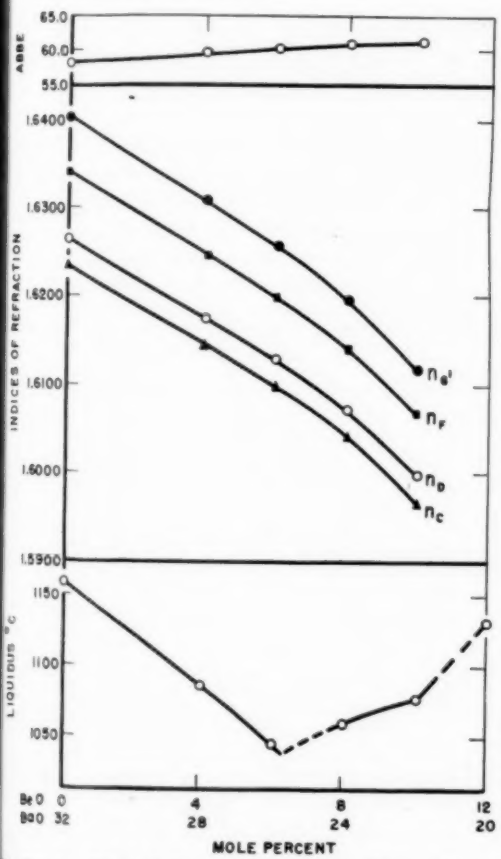

FIGURE 1. *Effect of the substitution of beryllium oxide for barium oxide on the Abbe value, indices of refraction, and liquidus.*

and approximately the same Abbe values as the base glass (table 2). A change in slope of the index-of-refraction-composition curves was found near the glass composition containing 8-mole percent of beryllium oxide (fig. 2). This compo-

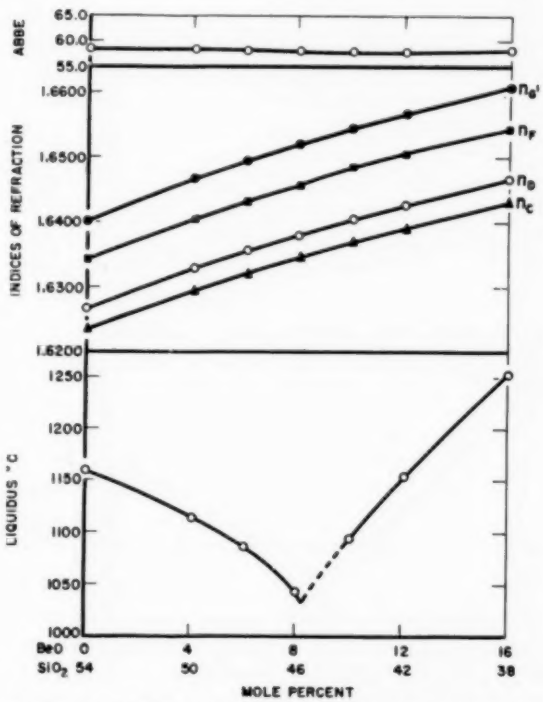

FIGURE 2. *Effect of the substitution of beryllium oxide for silica on the Abbe value, indices of refraction, and liquidus.*

TABLE 2. *Series 2. Substitution of beryllium oxide for silica*

Composition	GLASS NUMBER													
	680		684		683		645 and 760 [1]		682		681 and 704 [1]		705	
	Mole %	*wt %*	*Mole %*	*wt %*	*Mole %*	*wt %*	*Mole %*	*wt %*	*Mole %*	*wt %*	*Mole %*	*wt %*	*Mole %*	*wt %*
SiO_2	54	35.5	50	33.4	48	32.3	46	31.2	44	30.1	42	29.0	38	26.
B_2O_3	14	10.7	14	10.9	14	10.9	14	11.0	14	11.1	14	11.2	14	11.
BaO	32	53.8	32	54.6	32	55.1	32	55.5	32	55.9	32	56.4	32	57.
BeO	0	0.0	4	1.1	6	1.7	8	2.3	10	2.9	12	3.4	16	4.

INDEX OF REFRACTION									
	680	684	683	645	760	682	681	704	705
n_C	1.6236	1.6297	1.6325	1.6349	1.6349	1.6375	1.6395	1.6395	1.65
n_D	1.6268	1.6329	1.6357	1.6381	1.6382	1.6408	1.6427	1.6427	1.64
n_F	1.6343	1.6405	1.6434	1.6458	1.6459	1.6486	1.6506	1.6506	1.65
$n_{G'}$	1.6404	1.6467	1.6496	1.6518	1.6521	1.6548	1.6569	1.6569	1.66
ν	58.5	58.6	58.4	58.3	58.3	58.1	58.0	57.9	58.

LIQUIDUS, °C									
	1,160	1,115	1,088	1,049	1,040	1,096	1,156	1,163	1,25

[1] Duplicate batch compositions.

sition is approximately at the minimum of the liquidus-composition curve. All glasses in this series produced anisotropic crystals at the liquidus temperature. Crystals from glasses containing 8-mole percent or less of beryllium oxide has a maximum index of refraction of 1.605; for crystals from the other glasses this value was 1.655.

For optical glasses of this type, 6 to 8 mole per cent of beryllium oxide appears to be the optimum concentration, as this amount produces glasses with the lowest liquidus temperature. If the concentration of beryllium is further increased, the liquidus temperature increases rapidly, the glasses are more difficult to fine, and the tendency

TABLE 3. *Series 3. Substitution of calcium oxide for barium oxide*

Composition	GLASS NUMBER																			
	681 and 704 [1]		560		561		562		862		564 and 691 [1]		585		586		692		590	
	Mole %	*wt %*	*Mole %*	*wt %*	*Mole %*	*wt %*	*Mole %*	*wt %*	*Mole %*	*wt %*	*Mole %*	*wt %*	*Mole %*	*wt %*	*Mole %*	*wt %*	*Mole %*	*wt %*	*Mole %*	*wt %*
SiO_2	42	29.0	42	30.3	42	31.8	42	33.5	42	34.3	42	35.3	42	37.3	42	39.6	42	40.8	42	42.2
B_2O_3	14	11.2	14	11.7	14	12.3	14	12.9	14	13.3	14	13.6	14	14.4	14	15.3	14	15.8	14	16.3
BaO	32	56.4	28	51.7	24	46.4	20	40.7	18	37.6	16	34.3	12	27.2	8	19.3	6	14.9	4	10.3
BeO	12	3.4	12	3.6	12	3.8	12	4.0	12	4.1	12	4.2	12	4.5	12	4.7	12	4.9	12	5.0
CaO	0	0.0	4	2.7	8	5.7	12	8.9	14	10.7	16	12.6	20	16.6	24	21.1	26	23.6	28	26.2

INDEX OF REFRACTION													
	681	704	560	561	562	862	564	691	585	586	692	590	591
n_C	1.6395	1.6395	1.6355	1.6316	1.6256	1.6230	1.6207	1.6207	1.6158	1.6101	1.6076	1.6053	[2]
n_D	1.6427	1.6427	1.6388	1.6348	1.6289	1.6261	1.6237	1.6238	1.6189	1.6132	1.6106	1.6083	[2]
n_F	1.6506	1.6506	1.6464	1.6424	1.6362	1.6335	1.6311	1.6311	1.6261	1.6202	1.6177	1.6154	[2]
$n_{G'}$	1.6569	1.6569	1.6526	1.6485	1.6422	1.6395	1.6371	1.6371	1.6320	1.6261	1.6234	1.6210	[2]
ν	58.0	57.9	58.6	59.0	59.3	59.5	59.6	59.6	59.8	60.6	60.4	60.3	[2]

LIQUIDUS, ° C													
	1,156	1,163	1,153	1,150	1,138	1,131	1,114	1,111	1,080	1,050	1,013	1,052	1,130

[1] Duplicate batch compositions. [2] Devitrified during cooling.

of the glasses to devitrify increases. Therefore, the glass containing 8 mole percent of beryllium oxide in this series was used as the base composition for other series of melts.

3. Substitution of Calcium Oxide for Barium Oxide

The substitution of calcium oxide for barium oxide produced glasses with lower indices of refraction and higher Abbe values than the base glass (table 3). A minimum liquidus temperature was found at approximately 26 mole percent of calcium oxide.

With the exception of melts 681, 704, 691, and 692, the glasses in this series were not remelted. As the amount of calcium oxide in the glass was increased, the quality of the glasses improved with respect to their striae content. Glasses containing 16 mole percent or more of calcium oxide were obtained free from striae. The measured indices of refraction of glasses 560, 561, and 562 may not be reliable because of the presence of striae. For this reason, they were not considered in drawing the index-of-refraction-composition curves of figure 3.

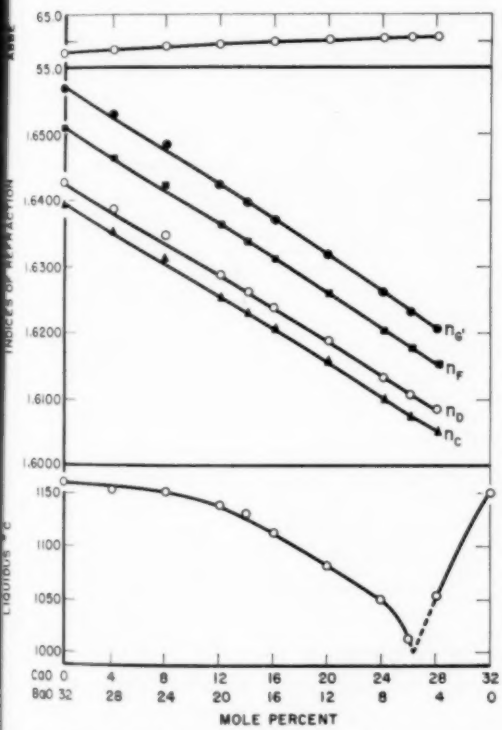

FIGURE 3. *Effect of the substitution of calcium oxide for barium oxide on the Abbe value, indices of refraction, and liquidus.*

No indices of refraction are given for melt 591 as this composition could not be cooled without devitrification. Consequently, the calcium oxide content of glasses of this type should not greatly exceed that of the glass having the minimum liquidus.

4. Substitution of Lanthanum Oxide for Barium Oxide

The substitution of lanthanum oxide for barium oxide produced glasses with the highest indices of refraction of any of the series of melts discussed in this paper (table 4). The increase in index of refraction averages 0.0056 per mole percent substituted. Discontinuities were found in the liquidus-composition and in the index-of-refraction-composition curves near the compositions containing 1 and 6 mole percent of lanthanum oxide (fig. 4). A straight line could fit the index of refraction data almost as well as the three lines drawn in figure 4. However, examination reveals systematic deviations from the straight line was compared with the random deviations, because of experimental error, which results when the index line is drawn in segments corresponding to the breaks in the liquidus curve. The liquidus temperature of the glasses increased very rapidly as the concentration of lanthanum oxide was increased above 6 mole percent with a corresponding increase in the difficulty of melting and fining the glasses. Melt 650 containing 12 mole percent of lanthanum oxide was very difficult to melt and contained striae, making a determination of the index of refraction for the G' line impossible. Because of these difficulties, the preparation of glasses containing larger amounts of lanthanum oxide was not attempted.

5. Substitution of Thoria for Barium Oxide

The substitution of thoria for barium-oxide produced glasses with higher indices of refraction and lower Abbe values than the base glass (table 5). The average increase in index of refraction was 0.0028 per mole percent of thoria substituted for barium oxide. As the thoria content of the glasses was increased up to 4 mole percent, the

TABLE 4. *Series 4. Substitution of lanthanum oxide for barium oxide*

Composition	Glass number																	
	645 and 760 [1]		675		646		651		673		676		647		649		674	650
	Mole %	*wt %*	*Mole %*	*wt %*	*Mole %*	*wt %*	*Mole %*	*wt %*	*Mole %*	*wt %*	*Mole %*	*wt %*	*Mole %*	*wt %*	*Mole %*	*wt %*	*Mole %*	*wt %*	*Mole %*	*wt %*
SiO_2	46	31.2	46	30.7	46	30.1	46	29.5	46	29.0	46	28.5	46	28.0	46	27.0	46	26.2	46	25.[illegible]
B_2O_3	14	11.0	14	10.8	14	10.6	14	10.4	14	10.2	14	10.0	14	9.9	14	9.5	14	9.2	14	[illegible]
BaO	32	55.5	31	52.7	30	50.0	29	47.5	28	45.0	27	42.6	26	40.3	24	36.0	22	31.9	20	28.[illegible]
BeO	8	2.3	8	2.2	8	2.2	8	2.1	8	2.1	8	2.1	8	2.0	8	2.0	8	1.9	8	[illegible]
La_2O_3	0	0.0	1	3.6	2	7.1	3	10.5	4	13.7	5	16.8	6	19.8	8	25.5	10	30.8	12	[illegible]

INDEX OF REFRACTION

	645	760	675	646	651	673	676	647	649	674	650
n_C	1.6349	1.6349	1.6403	1.6456	1.6518	1.6580	1.6634	1.6677	1.6794	1.6910	1.70[illegible]
n_D	1.6381	1.6382	1.6435	1.6490	1.6553	1.6614	1.6668	1.6713	1.6830	1.6948	1.70[illegible]
n_F	1.6458	1.6459	1.6513	1.6570	1.6634	1.6697	1.6752	1.6799	1.6919	1.7038	1.71[illegible]
$n_{d'}$	1.6518	1.6521	1.6575	1.6632	1.6698	1.6763	1.6820	1.6867	1.6989	1.7109	[illegible]
ν	58.3	58.3	58.2	57.2	56.7	56.4	56.2	55.2	54.6	54.0	53.[illegible]

LIQUIDUS, ° C

1,049	1,040	1,023	1,046	1,058	1,063	1,062	1,069	1,151	1,231	1,[illegible]

[1] Duplicate batch compositions.
[2] Glass-contained striae, making determination impossible.

TABLE 5. *Series 5. Substitution of thorium oxide for barium oxide*

Composition	GLASS NUMBER																	
	645 and 760 [1]		707		665		710 and 728 [1]		671 and 879 [1]		742		664		611			
	Mole %	*wt %*	*Mole %*	*wt %*	*Mole %*	*wt %*	*Mole %*	*wt %*	*Mole %*	*wt %*	*Mole %*	*wt %*	*Mole %*	*wt %*	*Mole %*	*wt %*	*Mole %*	*wt %*
SiO_2	46	31.2	46	30.9	46	30.5	46	30.1	46	29.7	46	29.4	46	29.1	46	28.[illegible]		
B_2O_3	14	11.0	14	10.9	14	10.8	14	10.6	14	10.5	14	10.4	14	10.2	14	[illegible]		
BaO	32	55.5	31	53.1	30	50.7	29	48.5	28	46.2	27	44.1	26	41.9	24	[illegible]		
BeO	8	2.3	8	2.2	8	2.2	8	2.2	8	2.2	8	2.1	8	2.1	8	[illegible]		
ThO_2	0	0.0	1	2.9	2	5.8	3	8.6	4	11.4	5	14.0	6	16.7	8	[illegible]		

INDEX OF REFRACTION

	645	760	707	665	710	728	671	679	742	664	611
n_C	1.6349	1.6349	1.6378	1.6408	1.6434	1.6433	1.6464	1.6464	1.6486	1.6513	[illegible]
n_D	1.6381	1.6382	1.6410	1.6441	1.6466	1.6465	1.6497	1.6497	1.6520	1.6546	[illegible]
n_F	1.6458	1.6459	1.6488	1.6518	1.6546	1.6544	1.6577	1.6576	1.6601	1.6627	[illegible]
$n_{d'}$	1.6518	1.6521	1.6551	1.6581	1.6612	1.6608	1.6641	1.6639	1.6665	1.6689	[illegible]
ν	58.3	58.3	58.2	58.3	57.6	57.9	57.5	58.0	57.0	57.4	[illegible]

LIQUIDUS, ° C

1,049	1,040	1,046	1,040	1,040	1,042	1,062	1,054	1,156	1,220	>1,[illegible]

[1] Duplicate batch compositions.
[2] Devitrified during cooling.

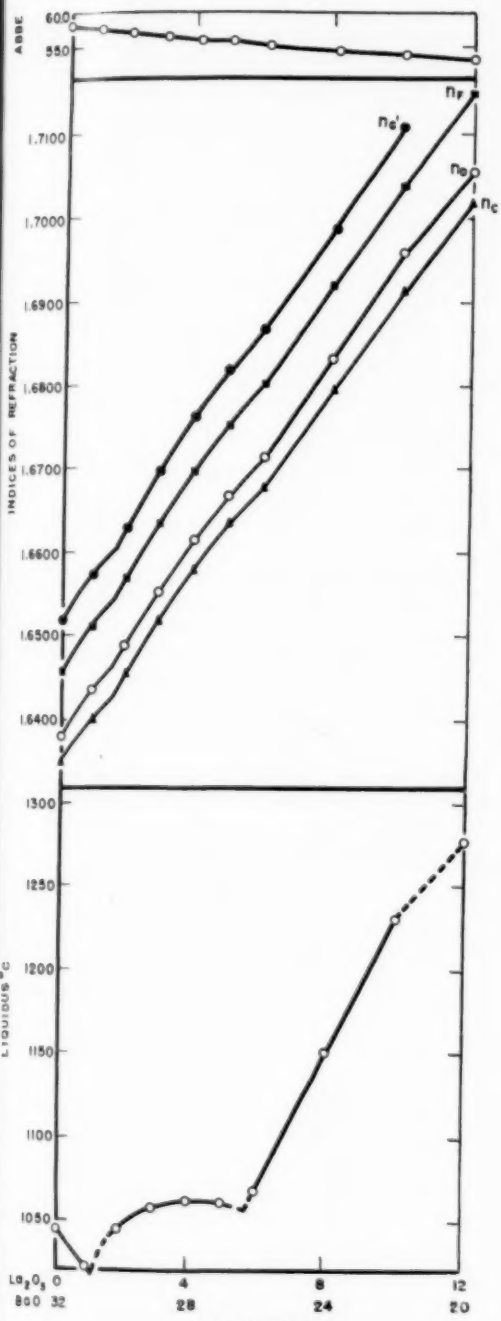

FIGURE 4. *Effect of the substitution of lanthanum oxide for barium oxide on the Abbe value, indices of refraction, and liquidus.*

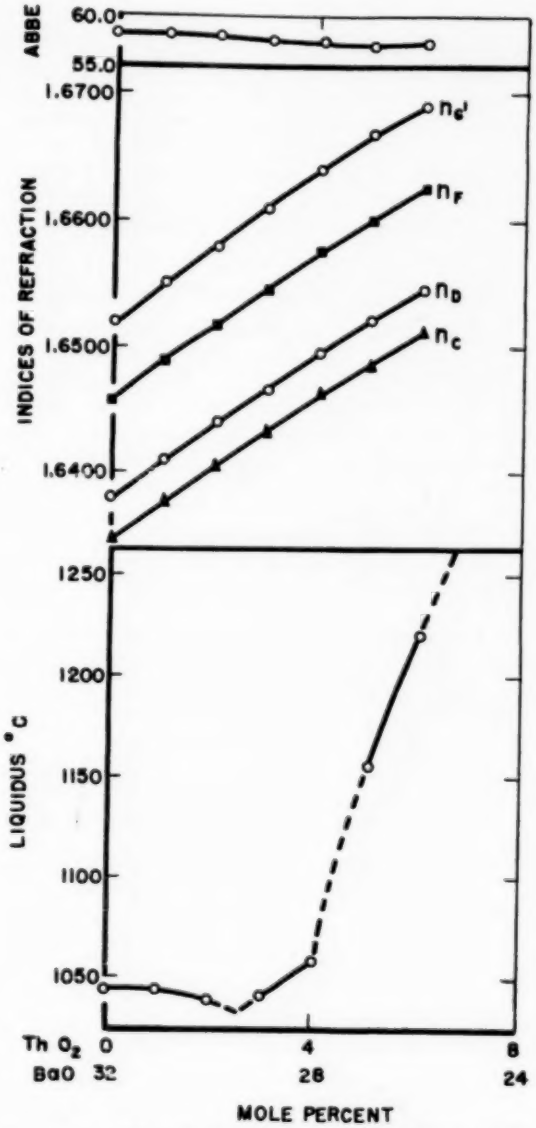

FIGURE 5. *Effect of the substitution of thorium oxide for barium oxide on the Abbe value, indices of refraction, and liquidus.*

liquidus changed very little, but further increases produced a large increase in liquidus temperature. Two discontinuities were found in the liquidus-composition curve (fig. 5) in the region containing 3 and 4 mole percent of thoria. When the indices of refraction are plotted against compositions, very slight changes in slope appear at the same composi-

tions where discontinuities are found on the liquidus curve. Although the changes on the index of refraction curve are sufficiently slight to permit a smooth curve to represent the data equally well, it is felt that by analogy with the previous series of glasses the representation of discontinuities in slope is justified. The series was discontinued with the melt containing 8 mole percent of thoria, as this melt could not be cooled without devitrification.

6. Substitution of Lithia for Barium Oxide

Lithia up to 16 mole percent was substituted for barium oxide in composition number 645. The indices of refraction and liquidus temperature of the glasses decreased, and the Abbe values increased as the lithia content of the glasses was increased (table 6 and fig. 6). The fluidity of the melts increased with increase in their lithia content. All the glasses produced the same type of crystals at the liquidus temperature, and no discontinuities were found in the liquidus-or index-of-refraction-composition curves of figure 6.

7. Substitution of Boron Oxide for Silica

The liquidus temperature of most of the melts previously discussed was 1,040° C or higher. It

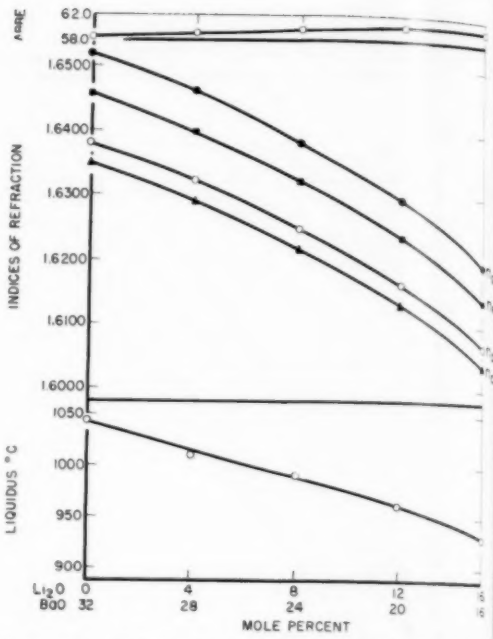

FIGURE 6. *Effect of the substitution of lithium oxide for barium oxide on the Abbe value, indices of refraction, and liquidus.*

TABLE 6. *Series 6. Substitution of lithium oxide for barium oxide*

Composition	GLASS NUMBER									
	645 and 760 [1]		699		689		680		693	
	Mole %	*wt %*	*Mole %*	*wt %*	*Mole %*	*wt %*	*Mole %*	*wt %*	*Mole %*	*wt %*
SiO_2	46	31.2	46	33.1	46	35.2	46	37.5	46	40.2
B_2O_3	14	11.0	14	11.7	14	12.4	14	13.2	14	14.2
BaO	32	55.5	28	51.4	24	46.8	20	41.7	16	35.7
BeO	8	2.3	8	2.4	8	2.6	8	2.7	8	2.9
Li_2O	0	0.0	4	1.4	8	3.0	12	4.9	16	7.0
INDEX OF REFRACTION										
	645	760	699		689		680		693	
n_C	1.6349	1.6349	1.6292		1.6216		1.6133		1.6039	
n_D	1.6381	1.6382	1.6324		1.6247		1.6163		1.6069	
n_F	1.6458	1.6459	1.6399		1.6321		1.6235		1.6140	
$n_{G'}$	1.6518	1.6521	1.6460		1.6380		1.6293		1.6196	
ν	58.3	58.3	59.0		59.7		60.1		60.1	
LIQUIDUS, ° C										
	1,049	1,040	1,009		990		959		932	

[1] Duplicate batch compositions.

TABLE 7. *Series 7. Substitution of boron oxide for silica*

Composition	GLASS NUMBER															
	696		726		701		698		702		727		697		703		714	
	Mole %	wt %	Mole %	wt %	Mole %	wt %	Mole %	wt %	Mole %	wt %	Mole %	wt %	Mole %	wt %	Mole %	wt %	Mole %	wt %
[illegible]	54	40.0	52	38.5	50	36.9	46	33.8	42	30.7	40	29.2	38	27.7	34	24.6	30	21.6
[illegible]	14	12.0	16	13.7	18	15.4	22	18.7	26	22.1	28	23.7	30	25.3	34	28.6	38	31.8
[illegible]	24	45.5	24	45.3	24	45.2	24	45.0	24	44.8	24	44.7	24	44.6	24	44.4	24	44.2
[illegible]	8	2.5	8	2.5	8	2.5	8	2.5	8	2.4	8	2.4	8	2.4	8	2.4	8	2.4
INDEX OF REFRACTION																		
[illegible]	1.6043		1.6053		1.6059		1.6070		1.6065		1.6067		1.6064		1.6052		1.6039	
[illegible]	1.6072		1.6083		1.6089		1.6100		1.6095		1.6096		1.6093		1.6082		1.6068	
[illegible]	1.6142		1.6153		1.6159		1.6170		1.6164		1.6165		1.6163		1.6150		1.6137	
[illegible]	1.6198		1.6209		1.6215		1.6225		1.6219		1.6220		1.6217		1.6204		1.6191	
[illegible]	61.1		61.4		61.3		61.4		62.0		62.0		62.0		62.4		62.2	
LIQUIDUS, °C																		
	1,061		1,030		1,002		962		927		943		940		936		903	

was believed that glasses with lower liquidus and higher indices of refraction and Abbe values could be produced by substituting boron oxide for silica, and five series of glasses were prepared in which this substitution was made.

Boron oxide was substituted for silica in glass no. 696 (table 1). The compositions and data for the glasses are given in table 7 and plotted in figure 7. This substitution produced glasses with lower liquidus temperatures and higher Abbe values than the base glass. It had an anomalous effect on the indices of refraction. The index of refraction (n_D) increased from 1.6072 to 1.6100, and then decreased to 1.6068 as the boron oxide content of the melts was increased from 14 to 38 mole percent. The maximum index of refraction was found near 22 mole percent of boron oxide.

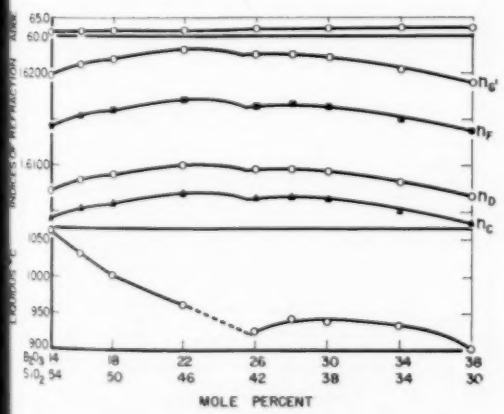

FIGURE 7. *Effect of the substitution of boron oxide for silica in glass 696 on the Abbe value, indices of refraction, and liquidus.*

Two discontinuities were found in the liquidus-composition and index-of-refraction–composition curves at the 18 and near the 26 mole percent of boron-oxide composition. Glasses containing 26 mole percent or less of boron oxide produced isotropic crystals at the liquidus, whereas the glasses containing 28 mole percent or more produced anisotropic crystals. As the boron oxide content of the glasses was increased the liquidus temperature decreased from 1,061° to 903° C.

Boron oxide was substituted for silica in glass no. 645 (table 2). The substitution of boron oxide for silica produced the same anomalous effect on the index of refraction as in the preceding series. Maxima were found in the index-of-refraction–composition curves at 22 and 26 mole percent of boron oxide (table 8 and fig. 8). Discontinuities were found in the index-of-refraction–composition and liquidus-composition curves near 18 and 24 mole percent of boron oxide. The liquidus decreased from 1,054° to 960° C and then increased slightly to 970° C as the boron oxide content of the glasses was increased. The Abbe values of the glasses increased as their boron oxide content was increased.

781956—48——3

TABLE 8. *Series 8. Substitution of boron oxide for silica*

Composition	GLASS NUMBER															
	645 and 760 [1]		730		688		687		731		686		685 and 706 [1]		715	
	Mole %	*wt %*	*Mole %*	*wt %*	*Mole %*	*wt %*	*Mole %*	*wt %*	*Mole %*	*wt %*	*Mole %*	*wt %*	*Mole %*	*wt %*	*Mole %*	*wt %*
SiO_2	46	31.2	44	29.8	42	28.4	38	25.6	36	24.2	34	22.8	30	20.0	26	17
B_2O_3	14	11.0	16	12.6	18	14.1	22	17.2	24	18.7	26	20.2	30	23.2	34	26
BaO	32	55.5	32	55.3	32	55.2	32	55.0	32	54.9	32	54.8	32	54.6	32	54
BeO	8	2.3	8	2.3	8	2.3	8	2.2	8	2.2	8	2.2	8	2.2	8	2
INDEX OF REFRACTION																
	645	760	730		688		687		731		686		685	706	715	
n_C	1.6349	1.6349	1.6353		1.6354		1.6365		1.6357		1.6363		1.6355	1.6353	1.63	
n_D	1.6381	1.6382	1.6385		1.6386		1.6397		1.6388		1.6395		1.6386	1.6385	1.63	
n_F	1.6458	1.6459	1.6461		1.6463		1.6473		1.6464		1.6470		1.6461	1.6460	1.64	
$n_{G'}$	1.6518	1.6521	1.6524		1.6525		1.6535		1.6525		1.6531		1.6522	1.6521	1.65	
ν	58.3	58.3	58.6		58.7		59.2		59.6		59.7		59.9	59.8	60	
LIQUIDUS, °C																
	1,049	1,040	1,028		1,005		985		972		962		968	968	970	

[1] Duplicate batch compositions.

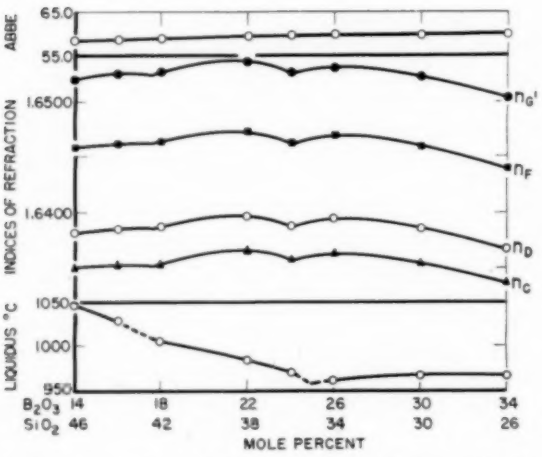

FIGURE 8. *Effect of the substitution of boron oxide for silica in glass 645 on the Abbe value, indices of refraction, and liquidus.*

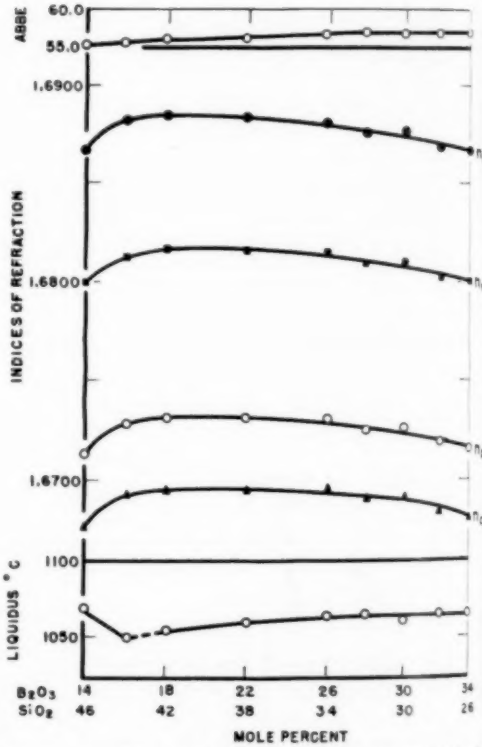

FIGURE 9. *Effect of the substitution of boron oxide for silica in glass 647 on the Abbe value, indices of refraction and liquidus.*

Boron oxide was substituted for silica in glass No. 647 (table 4) containing 6 mole percent of lanthanum oxide. The indices of refraction of the glasses increased and then decreased (table 9 and fig. 9) as the boron oxide content of the glasses increased from 14 to 34 mole percent. The glass containing 22 mole percent of boron oxide had the highest index of refraction of any glass in this series. The liquidus of the glasses decreased to a

TABLE 9. *Series 9. Substitution of boron oxide for silica*

Composition	GLASS NUMBER																	
	647		736		652		653, 711, and 723 [1]		654		737		911		773		713	
	Mole %	*wt %*	*Mole %*	*wt %*	*Mole %*	*wt %*	*Mole %*	*wt %*	*Mole %*	*wt %*	*Mole %*	*wt %*	*Mole %*	*wt %*	*Mole %*	*wt %*	*Mole %*	*wt %*
SiO_2	46	28.0	44	26.7	42	25.4	38	22.9	34	20.4	32	19.2	30	18.0	28	16.7	26	15.5
B_2O_3	14	9.9	16	11.2	18	12.6	22	15.4	26	18.1	28	19.5	30	20.8	32	22.2	34	23.5
BaO	26	40.3	26	40.3	26	40.2	26	40.0	26	39.9	26	39.8	26	39.7	26	39.6	26	39.6
BeO	8	2.0	8	2.0	8	2.0	8	2.0	8	2.0	8	2.0	8	2.0	8	2.0	8	2.0
La_2O_3	6	19.8	6	19.8	6	19.8	6	19.7	6	19.6	6	19.5	6	19.5	6	19.5	6	19.4
INDEX OF REFRACTION																		
	647		736		652		653	711	723	654		737		911		773		713
n_C	1.6677		1.6693		1.6695		1.6697	1.6695	1.6694	1.6695		1.6690		1.6691		1.6684		1.6681
n_D	1.6713		1.6729		1.6731		1.6733	1.6731	1.6729	1.6731		1.6725		1.6726		1.6719		1.6716
n_F	1.6799		1.6814		1.6816		1.6818	1.6816	1.6814	1.6815		1.6809		1.6810		1.6802		1.6759
$n_{G'}$	1.6867		1.6884		1.6884		1.6886	1.6884	1.6882	1.6881		1.6876		1.6878		1.6869		1.6866
ν	55.2		55.5		55.9		55.9	55.9	55.9	56.5		56.5		56.6		56.8		56.8
LIQUIDUS, ° C																		
	1,069		1,051		1,055		1,058	1,059	1,066	1,064		1,064		1,060		1,066		1,063

[1] Duplicate batch compositions.

minimum of 1,051° C for the glass containing 16 mole percent of boron oxide; then it increased to 1,165° C at approximately 26 mole percent and remained fairly constant as the boron oxide content was increased. In this respect, this series of glasses differs from all the other series in which boron oxide was substituted for silica. All of the glasses in this series produced anisotropic crystals at the liquidus; those from the glasses containing 14 to 16 mole percent of boron oxide were needle-like. The crystals from the other glasses were very small and had rounded edges.

TABLE 10. *Twelve mole percent lanthanum oxide glasses*

Composition	GLASS NUMBER									
	650		732		769		745		744	
	Mole %	*wt %*	*Mole %*	*wt %*	*Mole %*	*wt %*	*Mole %*	*wt %*	*Mole %*	*wt %*
SiO_2	46	25.3	30	16.3	30	15.9	28	14.7	28	14.4
B_2O_3	14	8.9	30	18.9	30	18.5	28	17.1	28	16.7
BaO	20	28.1	20	27.7	22	29.8	24	32.2	26	34.1
BeO	8	1.9	8	1.8	6	1.3	8	1.8	6	1.3
La_2O_3	12	35.8	12	35.3	12	34.5	12	34.2	12	33.5
INDEX OF REFRACTION										
n_C	1.7017		1.7005		1.7031		1.7095		1.7108	
n_D	1.7056		1.7043		1.7069		1.7134		1.7148	
n_F	1.7149		7.7135		1.7161		1.7230		1.7244	
$n_{G'}$	(1)		1.7208		1.7235		1.7306		1.7322	
ν	53.5		54.0		54.3		52.9		52.7	
LIQUIDUS, °C										
	1,276		1,164		1,176		1,176		1,160	

[1] Contained striae, making determination impossible.

Glass no. 650 containing 12 mole percent of lanthanum oxide had a high index of refraction (n_D=1.7056), an Abbe value of 53.5 and a liquidus of 1,276° C. Boron oxide was substituted for 16 mole percent of silica to determine whether this substitution would produce a glass with similar optical properties and a substantially lower liquidus temperature. The resulting glass, melt 732 of table 10, had an index of refraction, n_D, of 1.7043, Abbe value of 54.0 and a liquidus of 1,164° C, which is more than 100° C below the liquidus temperature of melt 650. The substitution of barium oxide for beryllium oxide or for silica and boron oxide in composition 732 produced glasses with approximately the same liquidus temperatures but with higher indices of refraction and, in the case of two of the glasses, lower Abbe values (see melts 769, 745, and 744 of table 10). Attempts to cool 1,000-g melts of compositions 732 and 745 in the form of a block approximately 1 inch thick resulted in considerable devitrification. Work is in progress to alter these glasses so that they can be cooled without devitrification.

Boron oxide was substituted for silica in glass number 671 containing 4 mole percent of thoria. The index of refraction increased and then decreased (table 11 and fig. 10). The maximum index of refraction appeared to be at a composition

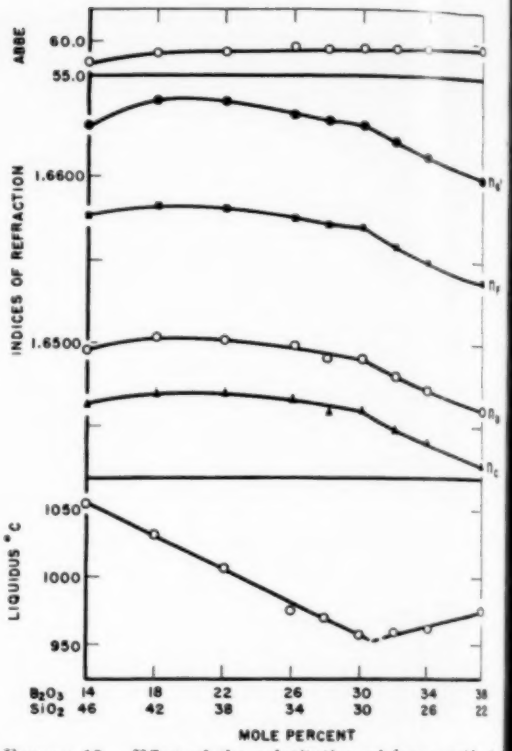

FIGURE 10. *Effect of the substitution of boron oxide for silica in glass 671 on the Abbe value, indices of refraction, and liquidus.*

TABLE 11. *Series 10. Substitution of boron oxide for silica*

Composition	GLASS NUMBER																	
	671 and 679 [1]		659 and 672 [1]		658		677		734 and 747 [1]		656		740		729		771	
	Mole %	*wt %*	*Mole %*	*wt %*	*Mole %*	*wt %*	*Mole %*	*wt %*	*Mole %*	*wt %*	*Mole %*	*wt %*	*Mole %*	*wt %*	*Mole %*	*wt %*	*Mole %*	*wt %*
SiO_2	46	29.7	42	27.0	38	24.4	34	21.7	32	20.4	30	19.1	28	17.8	26	16.5	22	13.9
B_2O_3	14	10.5	18	13.4	22	16.4	26	19.3	28	20.7	30	22.1	32	23.5	34	25.0	38	27.8
BaO	28	46.2	28	46.1	28	45.8	28	45.7	28	45.6	28	45.5	28	45.4	28	45.3	28	45.1
BeO	8	2.2	8	2.2	8	2.1	8	2.1	8	2.1	8	2.1	8	2.1	8	2.1	8	2.1
ThO_2	4	11.4	4	11.3	4	11.3	4	11.2	4	11.2	4	11.2	4	11.2	4	11.1	4	11.1
	INDEX OF REFRACTION																	
	671	679	659	672	658		677		734	747	656		740		729		771	
n_c	1.6464	1.6464	1.6470	1.6471	1.6470		1.6465		1.6457	1.6460	1.6459		1.6448		1.6440		1.6429	
n_D	1.6497	1.6497	1.6503	1.6504	1.6503		1.6497		1.6489	1.6493	1.6491		1.6480		1.6472		1.6460	
n_F	1.6577	1.6576	1.6582	1.6582	1.6582		1.6575		1.6568	1.6570	1.6569		1.6557		1.6549		1.6537	
$n_{g'}$	1.6641	1.6639	1.6645	1.6645	1.6645		1.6636		1.6631	1.6633	1.6631		1.6620		1.6612		1.6596	
$\nu_{g'}$	57.5	58.0	58.2	58.4	58.3		59.1		58.5	58.7	58.7		59.1		59.0		59.4	
	LIQUIDUS, °C																	
	1,062	1,054	1,039	1,030	1,005		977		969	970	958		960		962		971	

[1] Duplicate batch compositions.

containing approximately 20 mole percent of boron oxide. A minimum liquidus was found at approximately 30 mole percent of boron oxide. Anisotropic crystals were formed at the liquidus from glasses containing 30 mole percent or less of boron oxide. Glasses containing more than 30 mole percent of boron oxide produced isotropic crystals at the liquidus.

In all the series of melts in which boron oxide was substituted for silica similar anomalous effects on the indices of refraction of the glasses were observed. The maximum index of refraction in each series was found at 18 to 22 mole percent of boron oxide. A similar anomalous effect was observed by English and Turner [3] in a series of Na_2O.-B_2O_3.SiO_2 glasses containing approximately 20 percent of Na_2O. They found a maximum in the index of refraction curve at approximately 27 mole percent of boron oxide. This series of glasses was repeated under more controlled conditions by Wang and Turner [4]. The melts were made in platinum crucibles, and the glasses were analyzed. They found a maximum in the index-of-refraction-composition curve at approximately 20 mole percent of boron oxide. In a series of glasses containing alumina, calcium oxide, sodium oxide, potassium oxide, boron oxide, and silica, Turner and Winks [5] observed a maximum at approximately 24 mole percent of boron oxide.

8. Serviceability and Chemical Durability of Some Glasses Containing Lanthanum Oxide

When working with new compositions that might be useful as optical glasses, the question of the serviceability or ability of the glasses to maintain a clear polished surface is always of importance. The hygroscopic nature of an optical glass has been proposed as an indicator of its serviceability [6].

Hygroscopicity determinations were made on the glasses from series 4 in which lanthanum oxide was substituted for barium oxide and on three additional glasses containing 12 mole percent of lanthanum oxide.[5] A number of glasses were exposed at one time. The results in table 12 are grouped to show simultaneous determinations. For purposes of comparison a sample of a borosilicate crown optical glass (BSC 517/645) known to have good serviceability and a sample of a glass of unsatisfactory serviceability ("dish") were included. The results indicate that the glasses containing lanthanum oxide are as good as or better than BSC 517/645.

[5] Determinations made by Donald Hubbard of this Bureau.

TABLE 12. *Hygroscopicity of some glasses containing lanthanum oxide as indicated by exposure to the high humidity obtained from a saturated* $CaSO_4 \cdot 2H_2O$ *solution in a closed system* [1]

Glass No.	Mole percent of—					Water sorbed after exposure for—	
	SiO_2	B_2O_3	BaO	BeO	La_2O_3	1 hr	2 hr
GROUP A [2]							
						mg/cm²	*mg/cm²*
645	46	14	32	8	0	18.6	33.3
675	46	14	31	8	1	12.3	17.9
646	46	14	30	8	2	9.2	14.3
651	46	14	29	8	3	6.8	12.5
673	46	14	28	8	4	13.8	26.3
676	46	14	27	8	5	10.8	20.6
BSC 517/645	....	....	....	....	....	17.0	23.6
GROUP B							
676	46	14	27	8	5	17.0	20.6
647	46	14	26	8	6	7.1	11.5
649	46	14	24	8	8	3.8	11.2
674	46	14	22	8	10	2.0	6.5
650	46	14	20	8	12	3.6	9.6
GROUP C							
650	46	14	20	8	12	5.7	8.0
732	30	30	20	8	12	6.4	9.3
744	28	28	26	6	12	5.3	8.4
745	28	28	24	8	12	5.5	8.7
BSC 517/645	....	....	....	....	....	18.4	....
"Dish"	....	....	....	....	....	60.6	117.0

[1] Determinations made by Donald Hubbard of this Bureau.
[2] Groups indicate samples exposed at the same time.

To obtain an indication of the chemical durability of glasses containing lanthanum oxide, polished samples of four glasses containing 12 mole percent of lanthanum oxide were partially immersed in Britton universal buffer at pH values from 2 to 12 and in 5-percent sodium hydroxide solution for 6 hours at 80° C, and the amount of attack was measured by an interferometer method [7]. The results are given in table 13, which also includes for comparison the data on a BSC 517/645 and a light barium crown optical glass (LBC 540/574). The glasses containing lanthanum oxide appeared to be slightly less acid-resistant and considerably more alkali-resistant than the typical crown optical glasses.

TABLE 13. *Attack values on four glasses containing 12 mole percent lanthanum oxide exposed for 6 hr at 80°C to Britton universal buffer covering* pH *range 2.0 to 12.0 and to 5-percent sodium hydroxide solution as determined by an interferometer method* [1]

pH	Glass number					
	650	732	744	745	BSC 517/645 [2]	LBC 5725/574 [2]
	Fringes [3]	*Fringes*	*Fringes*	*Fringes*	*Fringes*	*Fringes*
2.2	½ pitted	½	¼+	½ pitted	⅒	⅒.
4.2		⅛	⅒	¾ ?		
6.0	(4)	(4)	(4)	(4)	⅒+	¾.
8.0	(4)	(4)	(4)	(4)	¼+	1+.
10.3	(4)	(4)		(4)		
11.9		(4)		(4)	1¾	1¼+.
5-percent NaOH solution.	⅒	(4)	⅒	(4)	[5] 3+	[5] 3¼.

[1] Determinations made by Donald Hubbard of this Bureau.

[2] BSC 517/645 and LBC 5725/574 are borosilicate crown and light barium crown optical glasses, respectively.

[3] One fringe equals approximately 0.29 micron. [4] Not detectable.

[5] Exposed for 3 hr; the attack for 6-hr exposure should be approximately twice the reported values.

IV. Conclusions

1. The substitution of beryllium oxide for barium oxide on a mole-for-mole basis lowered the index of refraction and increased the Abbe value. When beryllium oxide was substituted for silica, the index of refraction was increased, and the Abbe value was only slightly changed. When less than 6 to 8 mole percent of beryllium oxide was substituted for barium oxide or silica, the liquidus temperature was lowered. Greater amounts of beryllium oxide raised the liquidus temperature and increased the tendency of the glass to crystallize.

2. Substituting up to 26 mole percent of calcium oxide for barium oxide on a mole-for-mole basis markedly aided the fining of the glass, but the index of refraction was lowered and the Abbe value was increased.

3. The substitution of lanthanum oxide for barium oxide on a mole-for-mole basis produced a large increase in the index of refraction and a decrease in Abbe value. The increase in index of refraction averaged 0.0056 per mole percent substituted. The substitution of more than 6 mole percent produced a large increase in liquidus temperature.

4. The substitution of thorium oxide for barium oxide on a mole-for-mole basis produced an increase in the index of refraction and a decrease in Abbe value. The increase in index of refraction averaged 0.0028 per mole percent substituted The substitution of more than 4 mole percent produced a very large increase in liquidus temperature.

5. The substitution of boron oxide for silica produced an increase in Abbe value and an anomalous effect on the index of refraction. As the boron oxide was increased, the index of refraction increased to a maximum near 22 mole percent of boron oxide. Increasing the boron oxide content of the glasses usually lowered the liquidus temperature; the glasses containing lanthanum oxide were exceptions to this statement.

6. Discontinuities in the liquidus-composition curve and the index of refraction curves for each series were found at approximately the same composition. These discontinuities, which were accompanied by a change in the primary phase at the liquidus temperature, indicated a change in the arrangement of the atoms in the glass phase.

7. The possibility of producing optical glasses with indices of refraction of 1.71 or higher with Abbe values above 50.0 was indicated.

8. Glasses containing lanthanum oxide exhibited very low hygroscopicity, which indicates that they will maintain good polished surfaces under normal conditions of service. These glasses appeared to offer unusually high resistance to the attack of alkaline solutions.

9. Experimental glasses have been made that markedly depart from the linear relationship between index of refraction and Abbe value that prevails in ordinary optical glasses. The field of known optical glasses has been extended in a very desirable direction from the point of view of optical instrument design.

V. References

[1] U. S. Patents 1,943,051; 2,150,694; 2,206,081; 2,241-249; 2,297,453; 2,406,580; Gorden F. Brewster, Norbert J. Kreidl, and Tyler G. Pett, J. Soc. Glass Tech. **31,** 153 (1947).

[2] W. B. Silverman, J. Am. Ceram. Soc. **??,** 378 (1939).

[3] S. English and W. E. S. Turner, J. Soc. Glass Tech. **7,** 155 (1923).

[4] T. H. Wang and W. E. S. Turner, J. Soc. Glass Tech. **29,** 390 (1945).

[5] W. E. S. Turner and Francis Winks, J. Soc. Glass Tech. **9,** 389 (1925).

[6] Donald Hubbard, J. Research NBS **36,** 365 (1946) RP1706.

[7] Donald Hubbard and Edgar H. Hamilton, J. Research NBS 27, 143 (1941) RP1409.

WASHINGTON, November 12, 1947.

U. S. Department of Commerce
National Bureau of Standards

Research Paper RP1882
Volume 40, May 1948

Part of the Journal of Research of the National Bureau of Standards

Influence of Low Temperatures on the Mechanical Properties of 18:8 Chromium-Nickel Steel

By D. J. McAdam, Jr., G. W. Geil, and Frances Jane Cromwell

By means of tension tests of notched and unnotched specimens, an investigation has been made of the mechanical properties of various 18:8 chromium-nickel steels between room temperature and —188° C. One of the steels was ferritic; the others were of the metastable austenitic type. Plastic deformation of the metastable austenitic alloys causes a phase change and thus hardens the alloy. The rapidity of this change increases with decrease in temperature. At low temperatures the hardening due to the phase change is so rapid that the load-extension curve sometimes has two maxima. For this reason six important strength indices sometimes are required to evaluate the mechanical properties.

I. Introduction

In a series of papers, the authors and their associates have presented results of a general investigation of the influence of low temperatures on the mechanical properties of ferrous and nonferrous metals [6 to 11].[1] However, the only steels studied were ferritic, and the only stainless steel was a 13:2 chromium-nickel steel [6, 7]. Of the chromium-nickel alloys generally classed as austenitic there are two groups; in one group, the austenite is stable at room temperature; in the other group, the austenite is metastable. When alloys of the metastable, or "marginal", group are cooled rapidly from about 1,900° F, they are austenitic, but the austenite tends to change partially to ferrite when the alloy is plastically deformed at room temperature or is reheated above 1,000 °F and subsequently cooled slowly. Although metastability of these alloys is disadvantageous for some types of service, their strength and toughness make them suitable for many types of service, especially when good corrosion and oxidation resistance is required.

One of the most important of the marginal alloys contains about 18 percent of chromium and 8 percent of nickel and is generally known as 18:8 chromium-nickel steel. Generally the chromium content ranges between 17 and 19, and the nickel content between 7 and 9 percent. As the space lattice of chromium is body-centered and that of nickel is face-centered, an increase in the chromium content tends to make the alloy ferritic, and an increase in the nickel content tends to make it austenitic. For steels containing 18 percent of chromium, about 13 to 15 percent of nickel generally is necessary to make them stable at room temperature. The boundary between the stable and marginal group, however, depends on the percentage of carbon, manganese, and other alloying elements that may be added for special uses. It depends also on the temperature.

As shown by Aborn and Bain [1], Pilling [13] and others, the 18:8 alloy at room temperature would be completely stable only as a mixture of ferrite and carbides.[2] Although rapid cooling of the commercial 18:8 alloy from about 1,900° F prevents the transformation of the austenite to ferrite, some ferrite will be formed subsequently if the alloy is deformed plastically at room temperature. Because the ferrite thus formed contains carbon in supersaturated solution, it is sometimes called martensite [13]. In future reference to this phase, however, it will be designated as ferrite. During long exposure of the 18:8 alloy to elevated temperatures, the metastability of the alloy manifests itself by precipitation of carbides.

Krivobok and Lincoln [5] investigated a series of alloys of the 18:8 type. The chromium content ranged from about 17 to 19 percent and the nickel

[1] Figures in brackets indicate the literature references at the end of this paper.

[2] Complete stability could be obtained only by cooling the steel at a very slow rate, requiring a cooling period much longer than is practical.

from 7 to 9 percent. Moreover, there were two series with different carbon contents; the alloys of one series contained about 0.05 percent, and those of the other series contained about 0.15 percent of carbon. They studied the effect of composition on the mechanical properties of annealed strip and of strip that had been cold-rolled various amounts. The ultimate stress and the ductility were found to vary greatly with the composition. They also discuss the influence of composition on the stability of the austenite.

Pilling [13] compared the rate of work-hardening of an 18:8 alloy with that of an 18:14 alloy and found that the 18:8 alloy hardened much more rapidly because of a greater precipitation of ferrite. Pfeil and Jones [14] compared the rates of work-hardening of 18:8, 18:15, and 18:29 alloys, and also studied the variation of the work-hardening with carbon content. They found that the 18:8 alloy hardened more rapidly than the others. They also found that the rate of work-hardening of the 18:8 alloy increased greatly with increase in the carbon content, whereas the rate of work-hardening of the other alloys was affected very little. However, other investigators [15, 18] have reported results obtained with an 18:8 alloy in which the rate of work-hardening varied little or decreased with increase in the carbon content.

Austin and Miller [2] studied the magnetic permeability of chromium-nickel stainless steels. In the austenitic state an alloy of the 18:8 type, an 18:12 alloy, and a 25:12 alloy were found to have practically the same magnetic permeability, about 1.003. With cold-work the increase in permeability was rapid for the 18:8 alloy, was much less rapid for the 18:12 alloy, and was negligible for the 25:12 alloy. The permeability of the 25:12 alloy was practically unchanged after 90-percent reduction in area of the cross section.

Post and Eberly [15] studied the change in magnetic permeability with cold work as affected by variations in the percentages of chemical elements in the alloy. The chromium ranged from 13.9 to 24.3 percent, nickel from 7.75 to 20.65, carbon from 0.03 to 0.20, manganese from 0.4 to 3.92, molybdenum up to 2.4, titanium up to 0.5, and columbium up to 1.0 percent. An empirical formula was developed to show the percentage of nickel necessary to make an alloy stable when cold-worked to 80-percent reduction in cross section. As carbon, manganese, and molybdenum have a marked effect on the stability of austenite, constants for these elements are included in the formula. Titanium and columbium decrease the stability of austenite. Manganese is about half as effective as nickel in austenite-forming tendency, and molybdenum is one and one-half times as effective as chromium in ferrite-forming tendency. The formula developed, however, is based entirely on results of experiments at room temperature. The results of the present investigation will show that the formula does not apply to these alloys at low temperatures. The percentage of nickel necessary to cause stability varies with the temperature.

Uhlig [19] showed that nitrogen, which is present in the commercial 18:8 alloys, inhibits the change from austenite to ferrite at room temperature. If a heat is prepared free from nitrogen, it will be partly ferritic even when quenched from 2,100° F. If the carbon is also reduced to a negligible amount, the quenched alloy is almost entirely ferritic. With free access of air during melting, alloys with high chromium content absorb enough nitrogen to have a great effect on their properties.

When high strength is needed for a stable or marginal austenitic alloy, it can be obtained only by cold-work. On the other hand, Smith, Wycke, and Gorr [17] have developed a ferritic alloy of approximate 18:8 composition, which can be strengthened by precipitation-hardening. The austenite-forming and ferrite-forming elements are balanced so that the austenite transforms spontaneously to ferrite during about 4 hours after the alloy has been air-cooled from 1,900° F. The ferrite thus formed contains carbon and other elements in supersaturated solution. When the alloy is heated at 900° to 1,000° F, it is hardened by particle-precipitation. The precipitate has not yet been identified, but the most important element associated with the precipitation-hardening is titanium. If the titanium content is less than 0.4 percent, the alloy may remain partly austenitic at room temperature; if the content is more than 1.0 percent, precipitation-hardening will be excessive, and the ductility will be too low. Aluminum is added primarily as a deoxidizer, but the excess remaining in the alloy augments the precipitation-hardening effect of the titanium.

The influence of low temperatures on the prop-

erties of ferrous and nonferrous metals has been investigated by Colbeck, MacGillivray, and Manning [3]. An 18:8 chromium-nickel steel was included in their investigation. They report values for the yield stress, ultimate stress, and reduction of area at various temperatures between room temperature and the temperature of liquid air, but they give no values for the breaking stress. DeHaas and Hadfield [4] reported values for the same properties at room temperature and at the temperature of liquid hydrogen (−252.8° C). Their values for ultimate stress are shown in figure 15, which will be discussed later.

Rosenberg [16] studied the tensile and impact properties of aircraft metals, including various alloys of the 18:8 type, at temperatures down to −78° C. In addition to plain 18:8 alloys, there were alloys containing small percentages of elements that are customarily added to prevent local depletion of chromium by carbide precipitation at elevated temperatures. Specimens from some of these heats of steel have been included in the investigation to be described in this paper, and a few of the results obtained by Rosenberg have been plotted in some of the figures.

The literature on the properties of the chromium-nickel stainless steels is confined mainly to the study of the properties of the alloys at room temperatures and at elevated temperatures. Very little work has been reported on the mechanical properties of these alloys at low temperatures, and in these reported investigations insufficient information is supplied on the flow stresses, breaking stresses, and fracture of the alloys. In recent years there has been increasing need for additional information about the influence of temperature down to that of liquid air on the properties of these alloys. The present paper gives the results of an investigation of the effect of temperature, ranging from room temperature to that of liquid air, on the mechanical properties of 18:8 chromium-nickel alloys. The results obtained in this study also reveal the influence of plastic deformation and temperature on the transformation from austenite to ferrite and give information applicable qualitatively to the entire group of metastable alloys, including those that are much nearer than the 18:8 alloy to the boundary between the metastable and the stable austenitic group. An alloy of the ferritic 18:8 steel of the precipitation hardening type also was included in this study.

II. Materials, Method of Investigation, and Specimens

The alloys used in this investigation were all of the 18:8 type; the chemical compositions are given in table 1. The compositions of all but one of the alloys were such that the alloys were austenitic after quenching from 1,900° F; the alloy designated *EH* in table 1 becomes ferritic after quenching from 1,900° F, and can then be hardened by reheating to cause precipitation. The heat treatments given to these alloys are described in table 2.

TABLE 1. *Description of steels*

Material designation	Chemical composition								
	Carbon	Manganese	Silicon	Chromium	Nickel	Molybdenum	Titanium	Columbium	Aluminum
	Per-cent	*Per-cent*	*Per-cent*	*Per-cent*	*Per-cent*	*Per-cent*	*Per-cent*	*Per-cent*	*Per-cent*
EA	0.07	0.44	0.50	18.22	8.63	.....	.....	.....	.....
EB	.10	.47	.35	18.82	9.38	.....	.....	.....	.....
EC	.05	.39	.62	19.04	9.15	.....	0.29	.....	.....
EE	.075	.64	.61	18.61	10.16	.....	.....	0.93	.....
EF	.07	.93	.42	18.58	8.93	3.36	.....	.....	.....
EG	.07	.73	.48	18.41	7.88	2.80	.....	.....	.....
EH	.07	.50	.50	17.00	7.00	.....	.70	.....	0.20

TABLE 2. *Heat treatment of steels*

Material designation	Rod diameter	Temperature	Time held	Cooled in—
	in	*°F*	*hr*	
EA to *EE*	0.625	1,900	1	Water.
EF	.625	(a)	.....	.....
EH	1.000	1,900	½	Air.
		1,000	¾	Water.

a Annealed by manufacturer.

The alloys were received in the form of round rods of the sizes indicated in table 2. The rods of one of the alloys, designated by *EF* in table 1, had been annealed by the manufacturer. The annealing treatment doubtless was about the same as the austenitizing treatment given to alloys *EA* to *EE* (table 2). The rods of the other alloys were in cold-drawn condition; the rods of two of the

781956—48——4

alloys (*EB* and *EE*) had been drawn two different amounts.

For a description of the apparatus and the methods of testing at low temperatures, reference may be made to a previous paper [6]. Most of the specimens used in this investigation were unnotched and of standard form. Deeply notched cylindrical specimens, however, were also used in obtaining the diagrams in figure 16. The notches were all about the same depth (k=about 0.16),[3] but the notch angle varied between 150° and 50°. The notched specimens were about 5½ ins. long. The ends of the specimens were threaded to ⅝-in. diameter. Between the threaded ends, the specimen was machined to a uniform diameter of ⅝ in., and a circumferential V-notch was machined at the midsection. The notch was carefully machined to the selected angle, with the conical sides tangent to the arc at the root of the notch. Care was also taken to minimize heating, bending, or appreciable cold work during the machining.

The results are presented in diagrams of three types. Diagrams of the first type (figs. 1 to 3) show the influence of extension on the nominal stress, the load divided by the initial area of cross section. Diagrams of the second type (figs. 4 to 8) show the variation of the stress with the true strain. Diagrams of the third type (figs. 9 to 16) show how the strength indices of these alloys vary with temperature.

III. Variation of the Nominal Stress with Tensile Extension

Automatic load-extension diagrams obtained in the tension tests of the 18:8 chromium-nickel steels gave clear evidence of phase changes during the plastic deformation. Typical curves derived from automatic load-extension diagrams obtained with unnotched specimens are shown in figures 1, 2, and 3.[4] These curves show the influence of plastic extension on the nominal stress, that is, the stress value obtained by dividing the tensile load by the initial area of cross section.

[3] Notch depth is expressed in terms of the relative area ($k=b^2/B^2$) of the minimum cross section, where b and B represent the radii of the minimum and maximum cross section, respectively. Thus, the greater the notch depth, the smaller is the value of k.

[4] No actual points, except those for the final breaking stresses, are shown in the derived diagrams of figures 1, 2, and 3. The use of symbols or plotted points along the curves would tend to obscure the abrupt changes that occur, especially for the −78°C and −188°C curves.

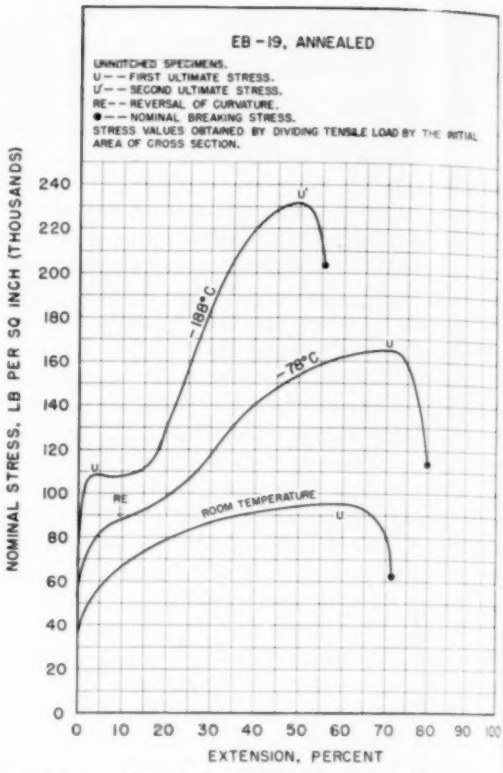

FIGURE 1. *Variation of nominal stress with extension, annealed 18:8 chromium-nickel steel, plain.*

Figure 1 shows results of tension tests of annealed austenitic plain 18:8 alloy at three different temperatures. The curve obtained at room temperature is qualitatively similar to a curve obtained without phase change. The slope decreases continuously between the points representing yield and maximum load. Transformation from austenite to ferrite during plastic deformation at room temperature evidently was not sufficient to cause a qualitative change in the form of the curve. The curve obtained at −78°C, however, gives clear evidence of a rapid phase change during the tension test. The reversal of curvature and the rapid increase in slope beyond the point of reversal (*RE*) indicates that the strengthening during plastic extension was due not only to ordinary work-hardening, but also to hardening caused by transformation of austenite to ferrite supersaturated with carbon. The hardening caused by this phase change possibly is not due merely to the difference in hardness between the ferrite and

austenite; it may be due partly to precipitation of fine particles of the ferrite within the austenite grains, or to precipitation of carbides.

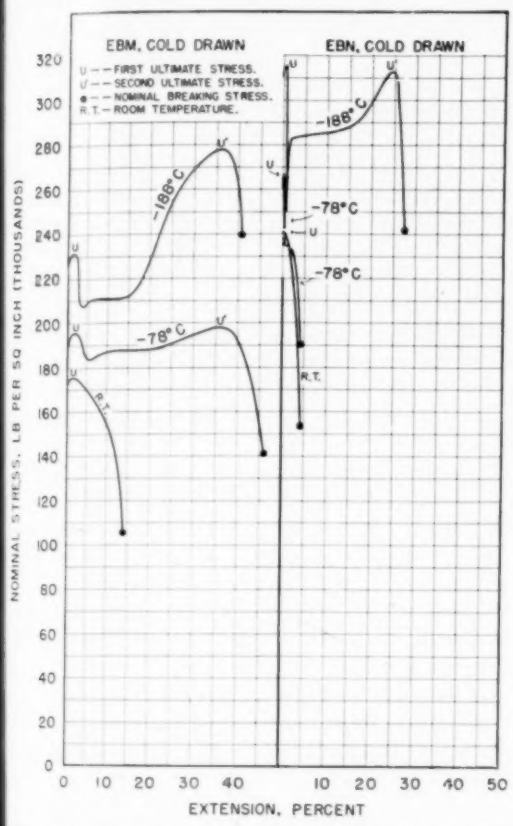

FIGURE 2. *Variation of nominal stress with extension, cold-drawn 18:8 chromium-nickel steels, plain.*

The curve obtained at −188° C reveals still more clearly the combined influences of work hardening and the hardening caused by phase change. This curve, like the curves obtained at room temperature and at −78° C, shows no abrupt yield point; from the region representing the beginning of plastic strain, the curve rises with continuously decreasing slope to the maximum designated by *U*. The descent beyond *U* represents the effect of incipient local contraction. In the absence of a phase change, the local contraction would have continued, and the curve would have descended with increasing slope to a point representing fracture. However, the local contraction and consequent descent of the curve evidently was stopped by a rapid phase change.

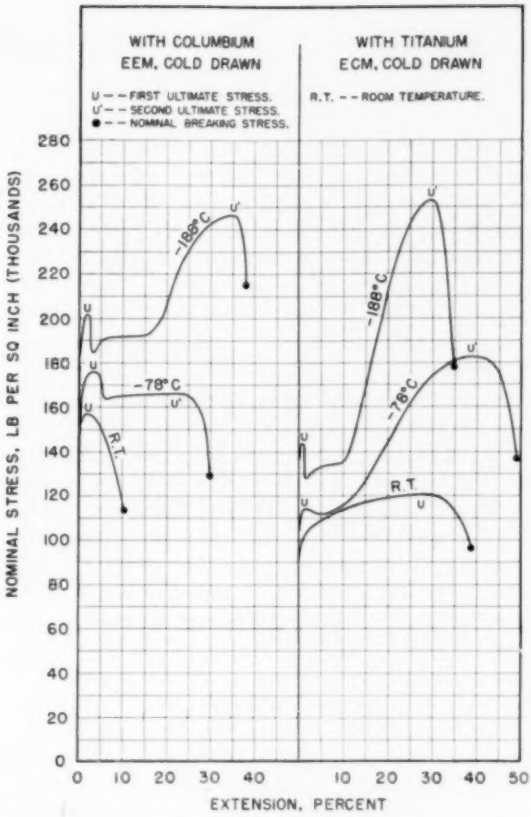

FIGURE 3. *Variation of nominal stress with extension, cold-drawn 18:8 chromium-nickel steels.*

The influence of the hardening due to the phase change then became dominant and caused the rise of the curve from the minimum to a second maximum designated by *U'*. This point indicates the beginning of final local contraction.

The ordinates of points *U* and *U'*, therefore, represent first and second ultimate stresses. The final local contraction beginning at the second maximum of the tensile load is not necessarily in the same place as the incipient local contraction at the first maximum. Specimens examined after fracture at low temperatures often show evidence of slight local contraction at a distance from the region of final contraction.

Figure 2 shows results obtained with cold-drawn-rods of the same alloy that was used in obtaining figure 1. The metal designated *EBM* in figure 2 was moderately cold-drawn to approximately 49-percent reduction of area, and the metal

designated *EBN* was severely cold-drawn to approximately 71-percent reduction of area. The curves obtained at room temperature are similar in form to the curve obtained at room temperature with the annealed alloy; there are no reversals in curvature or second maxima. As would be expected, however, the extension at the maximum load was much less for the moderately cold-drawn metal *EBM* than for the annealed metal, and there was practically no extension at the maximum load for the severely cold-drawn metal *EBN*. The curves obtained at room temperature, therefore, are qualitatively similar to curves obtained without phase change.

Comparison of the curves obtained at −188° C with the annealed metal and with the cold-drawn metals (figs. 1 and 2) shows that the increase in the nominal stress between the first and second maximum is greatest for the annealed metal, *EB–19*, and least for the severely cold-drawn metal *EBN*. A part of these differences is due to corresponding differences in ordinary work hardening between the first and second maximum, but more is due to the differences in the hardening caused by phase changes. The greater the plastic deformation at room temperature, the less is the combined influence of ordinary work-hardening and the hardening due to phase change during plastic deformation at −188° C.

As previously stated, columbium or titanium sometimes is added to 18:8 alloys to prevent the precipitation of chromium-rich carbides at elevated temperatures, and the resultant local depletion of the chromium in solid solution. The strong affinity of columbium and titanium for carbon, however, tends indirectly to decrease the stability of the austenite at low temperatures. Figure 3 shows results of tension tests of two cold-drawn 18:8 alloys, one containing columbium and the other containing titanium. Comparison of the curves obtained at room temperature shows that alloy *ECM* had been less severely cold-drawn than alloy *EEM*. The ultimate stress was much lower, and the extension at the maximum load was much greater for alloy *ECM* than for alloy *EEM*. Moreover, both these alloys evidently had been less severely cold-drawn than the moderately cold-drawn plain 18:8 alloy, *EBM* (fig. 2).

The curves obtained at −78° C with alloys *ECM* and *EEM* (fig. 3) differ greatly. Although both curves reveal clearly the hardening effect of ferrite precipitation, the effect was more prominent with the alloy containing titanium. With the alloy containing columbium, the precipitation hardening was sufficient merely to stop the abrupt decrease of the nominal stress from the first maximum (U) and then to hold the stress nearly constant during the extension to the second maximum (U'). The second ultimate stress, therefore, was a little lower than the first. With the alloy containing titanium, however, the nominal stress increased more than 50 percent between the first and second maximum. Precipitation of ferrite during the plastic deformation evidently was much more rapid for the alloy containing titanium than for the alloy containing columbium. Comparison of the curves obtained at −188° C (fig. 3) shows again that the rise between the first and the second maximum is much greater for alloy *ECM* than for alloy *EEM*.

The more rapid hardening of the alloy containing titanium, however, cannot be attributed to a difference between the effects of titanium and columbium. As previously shown, the alloy containing titanium had been less severely cold-drawn than the other alloy, and hence the precipitation of ferrite during the cold-drawing at room temperature had been less. Consequently both work-hardening and precipitation hardening at the low temperatures were greater for the alloy containing titanium than for the alloy containing columbium.

IV. Variation of the Flow Stress with the True Strain

Curves of the type shown in figures 1, 2, and 3 are important because they show how the load varies during a tension test, but they do not show how the "true stress" varies with plastic strain, nor do they represent correctly the variation of the strain after the beginning of local contraction. Therefore, in diagrams of the type now to be considered, ordinates represent true stresses and abscissas represent true strains. Figures 4 to 8 show diagrams of this type. Each curve in these figures shows the influence of plastic strain on the "flow stress," which is the true tensile stress at any instant during flow of the metal. Strain is represented in terms of A_0/A,[5] in which A_0

[5] The ratio A_0/A is designated the effective length ratio and represents the ratio of current to original length, had the specimens contracted uniformly at the same rate as at its minimum cross section.

and A represent the initial and current areas of cross section. Values of A_0/A are represented on a logarithmic scale; therefore, true strain, which is defined as $\log_e A_0/A$, would be measured linearly on this scale.

The results of tension tests represented in figures 1, 2, and 3 are represented again in the diagrams of a different type in figures 4, 5, and 6, respectively. During the tension tests at room temperature the change in the diameter of the specimen was measured at frequent intervals, and measurement was continued almost to the beginning of fracture. The small open circles along the flow-stress curves represent the results of measurements during flow, and the end of each curve obtained at room temperature represents the true fracture stress, the stress at the beginning of

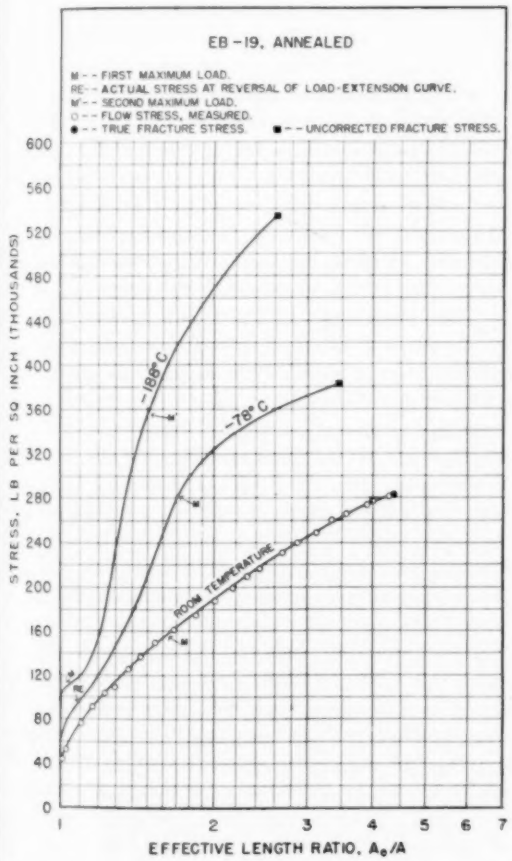
EB-19, ANNEALED
M - - FIRST MAXIMUM LOAD.
RE - - ACTUAL STRESS AT REVERSAL OF LOAD-EXTENSION CURVE.
M' - - SECOND MAXIMUM LOAD.
O - - FLOW STRESS, MEASURED.
● - - TRUE FRACTURE STRESS.
■ - - UNCORRECTED FRACTURE STRESS.
STRESS, LB PER SQ INCH (THOUSANDS)
EFFECTIVE LENGTH RATIO, A_0/A
-188° C
-78° C
ROOM TEMPERATURE

FIGURE 4. *Variation of true stress with strain, annealed 18:8 chromium-nickel steel, plain.*

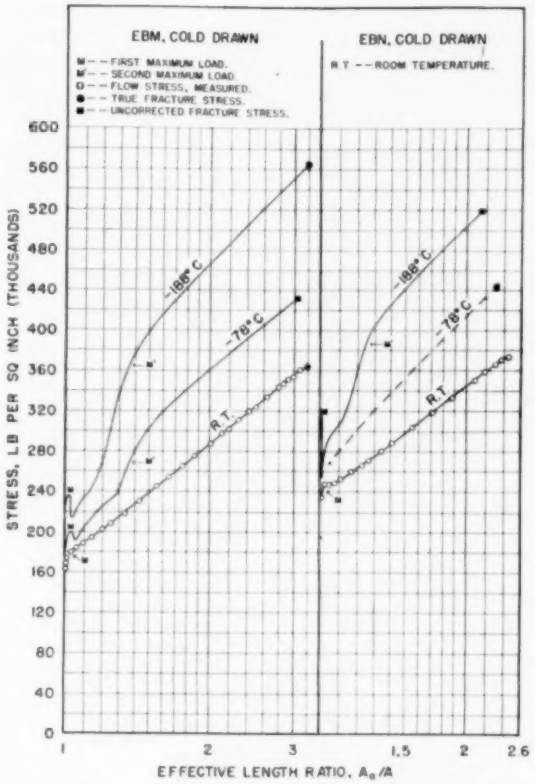
EBM, COLD DRAWN
EBN, COLD DRAWN
M - - FIRST MAXIMUM LOAD.
M' - - SECOND MAXIMUM LOAD.
O - - FLOW STRESS, MEASURED.
● - - TRUE FRACTURE STRESS.
■ - - UNCORRECTED FRACTURE STRESS.
R.T. - - ROOM TEMPERATURE.
STRESS, LB PER SQ INCH (THOUSANDS)
EFFECTIVE LENGTH RATIO, A_0/A
-188° C
-78° C
R.T.

FIGURE 5. *Variation of true stress with strain, cold-drawn 18:8 chromium-nickel steels, plain.*

fracture. The fracture stresses were also determined in the usual way, by dividing the load at the beginning of fracture by the area of cross section measured after fracture. The area so determined is generally less than the area measured at the beginning of fracture, because the metal at the rim of the cross section continues to extend after fracture begins at the axis [7, 10, 11]. With these 18:8 chromium-nickel steels, however, the difference between the uncorrected fracture stress and the true fracture stress was slight, even at room temperature. The uncorrected fracture stresses of the alloys tested at room temperature, therefore, are not indicated in the figures.

During the tension tests at —78° C and at —188° C, no transverse measurements of the specimen were made, and the fracture stresses were determined in the usual way, by dividing the tensile load at the beginning of fracture by the area of cross section measured after fracture.

As the difference between the uncorrected fracture stress and the true fracture stress was slight even at room temperature, it probably was negligible at low temperatures. The uncorrected fracture stresses indicated in figures 4, 5, and 6, therefore, probably are not far from the true fracture stresses.

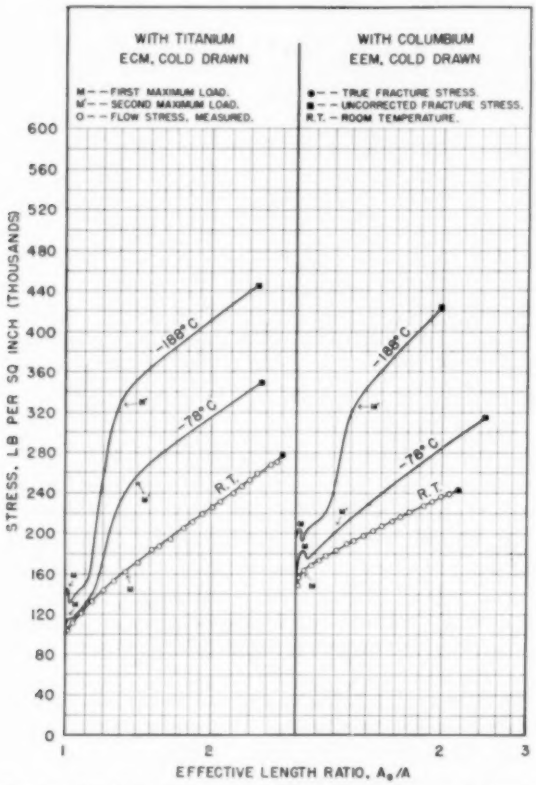

FIGURE 6. *Variation of true stress with strain, cold-drawn 18:8 chromium-nickel steels.*

As no transverse measurements of the specimens were made during the tests at −78° C and −188° C, the flow-stress curves for these temperatures (figs. 4, 5, and 6) are derived from the corresponding curves representing the variation of the nominal stress with extension (figs. 1, 2, and 3). The derivation is based on the simplifying assumption that each specimen remains cylindrical during the extension to the beginning of final local contraction. This assumption implies that, during this extension, the percent difference between the flow stress and the nominal stress at any instant is equal to the percent extension. In this way, the flow-stress curves for −78° C and −188° C in figures 4, 5, and 6 have been constructed between the point representing yield and the point representing the final maximum of the load. Because of the local contraction, the curve between the point representing the final maximum and the point representing fracture cannot be determined from a load-extension diagram. Between these points, however, the curves have been drawn to represent the probable approximate variation of the flow stress at −78° C and 188° C.

The flow-stress curve obtained with annealed plain 18:8 alloy at room temperature (fig. 4) is similar in form to curves obtained with metal that is free from phase change during plastic deformation. As shown in previous papers [10, 11], the flow-stress line obtained with some metals is nearly straight between the points representing maximum load and fracture, as in figure 6, but the line obtained with many metals rises with continuously decreasing slope, as in figure 4. The flow-stress lines obtained at room temperature with the cold-drawn plain alloys (figure 5), rise with increasing slope, thus showing the effect of the precipitation-hardening during the plastic deformation. The flow-stress curves obtained at low temperatures, like the corresponding curves in figures 1, 2, and 3, give clear evidence of the influence of phase change. The reversal of curvature and the steep ascent to the point representing the beginning of local contraction can be attributed only to the hardening caused by rapid precipitation of ferrite throughout the austenite.

Although the nominal-stress curve obtained with the annealed alloy at −188° C (fig. 1) descends beyond the first maximum (U), the corresponding curve in figure 4 indicates that the flow stress rises continuously with plastic strain. The continuous rise of the flow stress is in accord with the previously expressed view that the descent of the nominal-stress curve beyond the first maximum in figure 1 does not represent a yield point, but represents incipient local contraction. Moreover, the curves obtained at −78° C with the annealed alloy show no indication of a yield point. However, all the curves obtained with the previously cold-worked alloys at the low temperatures apparently indicate an abrupt drop in the stress beyond the first maximum. Although this drop of the curves resembles somewhat the drop between the upper and lower yield points of ferritic steels, there are two reasons why the drop in the

curves does not represent a yield point. One reason is that considerable plastic strain occurs during the test before the load reaches the first maximum, for all the alloys except the severely cold-drawn plain alloy *EBN* (fig. 5). The other reason is that no suggestion of a yield was obtained with the annealed alloy (fig. 4). It seems probable, therefore, that there is no drop in the true flow stress for either an annealed or a cold-drawn 18:8 alloy. The strains plotted in figures 4, 5, and 6 are *average* true strains, calculated on the assumption that the specimens remained cylindrical during the extension to the beginning of final local contraction. Actually, however, the true strain in the region of incipient local contraction may be considerably greater than is indicated by the average extension of the specimen. Moreover, inertia effects probably accentuate the abrupt drop of the load from the first maximum. The true flow stress, therefore, probably rises continuously with the plastic deformation of either annealed or cold-drawn 18:8 alloys.

In figure 7, a comparison is made between a cold-drawn metastable austenitic alloy containing molybdenum and a precipitation-hardened alloy. The previously discussed composition of the precipitation-hardenable alloy (*EH*), and the details of the heat treatment are given in tables 1 and 2. As shown in figure 7, the flow-stress curves obtained with the alloy (*EGM*) containing molybdenum are generally similar to the curves shown in figures 4, 5, and 6. The ductility of the metastable austenitic alloys evidently is not seriously affected by the rapid hardening caused by the phase change during plastic deformation at low temperatures (figs. 4, 5, and 6). However, the effect of low temperatures on the ductility of the annealed plain 18:8 alloy (fig. 4) was greater than the effect on the cold-drawn alloys (fig. 5). The adverse effect of a low temperature on the ductility evidently is greater when all the plastic deformation is at the low temperature than when part of it is at room temperature. Precipitation of ferrite from the austenite, therefore, evidently has considerable effect on the ductility. The good ductility exhibited by these alloys at low temperatures may be due partly to retention of some of the austenite.

At room temperature, the flow stress curve for the ferritic alloy *EH–A–10* (fig. 7) was higher than that for the moderately cold-drawn plain alloy

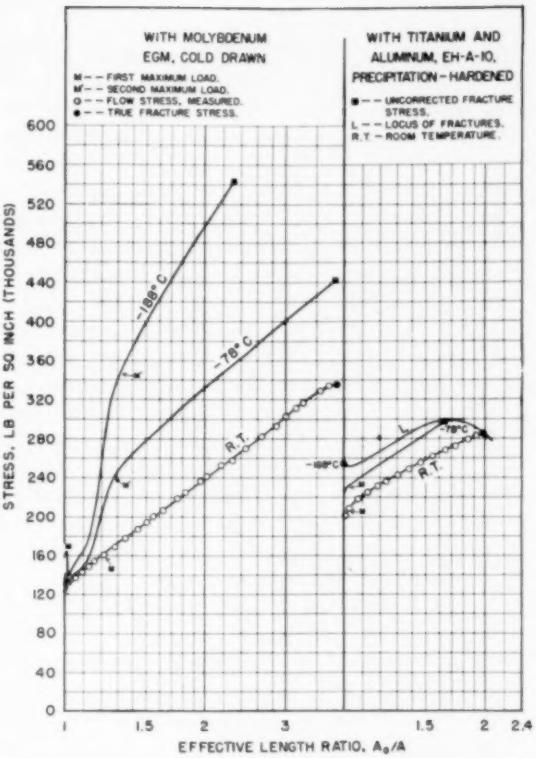

FIGURE 7. *Variation of true stress with strain, 18:8 chromium-nickel steels.*

EBM (fig. 5) or the moderately cold-drawn alloys containing titanium, columbium, and molybdenum (figs. 6 and 7), but was lower than that for the severely cold-drawn plain alloy *EBN* (fig. 5). The ductility of the ferritic alloy at room temperature (fig. 7) was a little less than that of any of the cold-drawn metastable austenitic alloys (figs. 5, 6, and 7). With decrease in temperature, the ductility of the ferritic alloy decreased rapidly, and a specimen tested at —188° C showed no ductility. To make sure that the brittleness at that temperature was not due to some defect in the specimen, another specimen was tested; the result was the same. The effect of low temperatures on the ductility of this alloy, therefore, evidently is similar to the effect on the ductility of annealed low-carbon steels. For use at low temperatures, the ductility would possibly be improved if some austenite were retained along with the ferrite and the precipitated constituent.

It has been shown that the influence of the total plastic deformation on the flow stress at a low temperature depends on the relative amounts of the plastic deformation at room temperature and at the low temperature. For a study of the influence of both the prior plastic deformation at room temperature and the total plastic deformation, results obtained with the same metal after various amounts of prior plastic deformation may be assembled in a single diagram, in which abscissas represent values of the total plastic deformation [12]. A diagram of this type is shown in figure 8, which is derived by assembling flow-stress curves reproduced from figures 4 and 5. Figure 8 thus represents the influence of total plastic deformation on the flow stress and fracture stress of a plain 18:8 chromium-nickel steel. As the true strains represented by the prior plastic deformation and the subsequent deformation during a tension test are directly additive, and inasmuch as the abscissa and ordinate scales in figure 8 are the same as in figures 4 and 5, the flow-stress curves have been transferred directly from the basic diagrams to figure 8. In such a transfer, however, it is necessary to place the origin of each curve at an abscissa representing the corresponding amount of prior plastic deformation. The two vertical dot-and-dash curves in figure 8 represent the amounts of prior plastic deformation given to alloys *EBM* and *EBN*. Curve F_0 represents approximately the tensile flow-stress curve that would be obtained if the stress could be kept unidirectional. The local contraction of a tension test specimen induces transverse radial tensile stress, and the ratio of the transverse to the longitudinal stress (radial stress ratio) increases with the local contraction. Because of the increasing radial stress ratio, curve F for the annealed alloy rises above the derived curve F_0. A method of deriving curve F_0 is described in a previous paper [12] in which the relation between curves F_0 and F is shown in diagrams. In figure 8, curve F_0 has been drawn so as to be in approximately correct relation to curve F for the annealed alloy. It also has been drawn to pass through the first maximum points M on the flow-stress curves obtained with the cold-drawn alloys *EBM* and *EBN* at room temperature. The diagram thus represents qualitatively the influence of prior and total plastic deformation and of low temperatures on the flow stress and fracture stress.

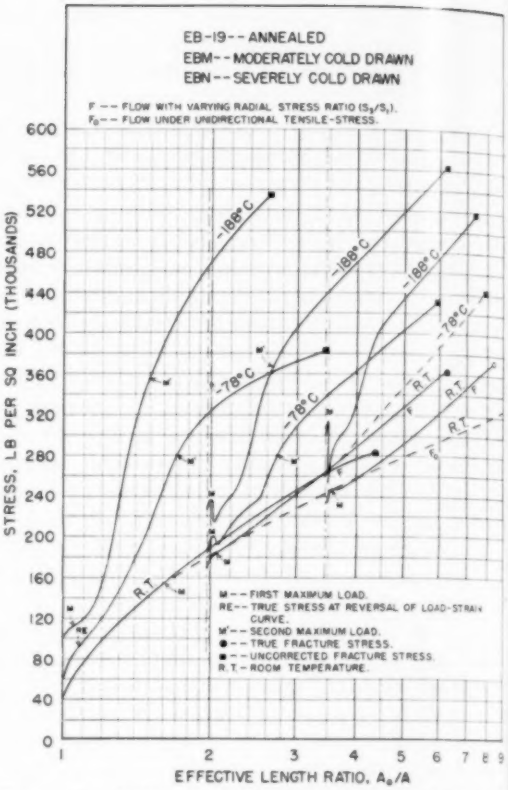

FIGURE 8. *Influence of prior and total plastic deformation on flow stress and fracture stress of plain 18:8 chromium-nickel-steel.*

The curves representing flow during local contraction at room temperature rise above curve F_0 because of increasing transverse radial tensile stress induced by the local contraction. A curve similar to curve F_0 could be drawn through points M on the flow-stress curves obtained at −188° C. As points M represent flow stresses after various amounts of plastic deformation at room temperature and only slight plastic deformation at −188° C, a curve drawn through points M would approximately represent flow under unidirectional tensile stress entirely at −188° C, but with the requirement that the precipitation-hardening was the same as at room temperature. A similar curve could be drawn to represent flow at −78° C. The more rapid rise of the flow-stress curves obtained at −78° C and −188° C (fig. 8) is due to the more rapid precipitation-hardening during flow at these temperatures.

The rapid rise of these curves cannot be attributed to an increase in the radial stress ratio; the stress remains nearly unidirectional until the beginning of the final local contraction, designated by M'.

The rapid precipitation-hardening during plastic deformation at low temperatures evidently increases the fracture stress nearly as rapidly as it increases the flow stress. If precipitation-hardening were no more rapid at −188° C. than at room temperature, the point representing fracture in a test entirely at −188° C would be on the previously discussed curve that could be drawn through the corresponding points M in fig. 8. With sufficient increase in the prior plastic deformation at room temperature, the fracture stress at a low temperature would begin to decrease because of the decrease in the relative amount of plastic deformation at the low temperature and the accompanying decrease in the amount of precipitation-hardening.

V. Magnetic Changes with Plastic Deformation

Reference has been made to several investigations of the change in magnetic properties of 18:8 alloys with plastic deformation [1, 2, 13, 15]. In some investigations, quantitative studies of the transformation from austenite to ferrite have been made by measurement of magnetic permeability [2, 15]. None of the specimens used in these previous investigations, however, had been plastically deformed at low temperature. As the evidence in figures 1 to 8 shows that the hardening due to the phase change is more rapid at low temperatures than at room temperature, a brief qualitative investigation has been made to determine if these differences in precipitation-hardening could be correlated with changes in magnetism. For this purpose typical specimens that had been used in tension tests represented in figures 4 to 7 were explored by means of a small strong horseshoe magnet. These specimens included annealed, moderately cold-drawn, and severely cold-drawn metals. Some had been tested to fracture at room temperature, and some had been tested at low temperatures.

The specimens that had been tested to fracture at room temperature were slightly magnetic at the surface of fracture and in the adjacent locally contracted region, but the magnetic attraction was hardly noticeable elsewhere along the specimen. Moreover, the magnetic attraction was not appreciably greater for moderately cold-drawn than for annealed metal. The attraction was a little greater for specimens of severely cold-drawn metal, especially at the surface of fracture. However, the attraction was not strong enough to lift the specimens. The increase in magnetism in the locally contracted region is a result of the relatively large amount of plastic deformation occurring during the local contraction.

The specimens that had been tested at −78° C and at −188° C were only slightly magnetic at the threaded ends, which had not been plastically deformed at the low temperatures. Between the end fillet and the locally contracted region, however, each specimen was strongly magnetic; the attraction was strong enough to lift some specimens attached to both poles of the magnet. At the surface of fracture, the attraction was so strong that each specimen could be vertically suspended from one pole of the magnet. The magnetic attraction along the plastically extended side of the specimen, however, evidently was not as strong for the severely cold-drawn specimens as for the moderately cold-drawn or annealed specimens. The weaker magnetic attraction for the severely cold-drawn alloy may be correlated with the relatively smaller amount of plastic deformation at low temperature. The method of investigation was not sensitive enough to detect differences in magnetism between specimens of annealed metal and specimens of moderately cold-drawn metal, or to detect differences between specimens that had been plastically deformed at −78° C and those that had been deformed at −188° C.

The results of these qualitative magnetic tests confirm the previously expressed view that the rapid rise of the flow-stress with plastic deformation at low temperatures (figs. 4 to 8) is due to a rapid transformation of austenite to ferrite.

VI. Variation of Strength Between Room Temperature and —188° C

Consideration will now be given to diagrams of a different type. In these diagrams, which are shown in figures 9 to 16, temperatures are plotted as abscissas, and indices of strength are plotted as ordinates. In these figures, the temperature scale is the same that has been used in previous papers by the authors and their associates [6 to 10]. Temperatures in degrees K are plotted on a

logarithmic scale. As abscissas are proportional to the logarithm of the degrees K, the scale is the same in principle as Kelvin's original thermodynamic scale. This scale has been used because, as has been shown [6 to 10], it gives a linear relationship between temperature and the strength indices for various metals in the absence of phase changes.

The strength of most metals can be evaluated by the use of only three indices, namely, the yield stress, ultimate stress, and fracture stress. For 18:8 chromium-nickel steels at low temperatures, however, six strength indices are important, although sometimes less than six are sufficient. As illustrated in figures 1 to 7, these indices are: yield stress, first ultimate stress, stress at a minimum in the load-extension curve, stress at a reversal of the load-extension curve, second ultimate stress, and true fracture stress. All these indices and the true stress at the second maximum load have been used in figures 9 to 14. Nominal-stress values, such as those represented in figures 1 to 3, have been used for the first ultimate stress, the minimum in a load-extension curve, the reversal of a load-extension curve, and the second ultimate stress.

Figure 9 shows results obtained with a plain 18:8 alloy. This is not the same as the alloy used in obtaining figures 1, 2, 4, 5, and 8. As most of the experiments represented in figure 9 were made several years ago, the importance of determining values for both the first and second ultimate stresses was not realized. Complete curves for the first ultimate stress, therefore, could not be obtained. As indicated by the symbols along the two ultimate-stress curves in figure 9, part of each curve shows the influence of a range of temperature on the first ultimate stress, and part shows the influence of a lower range of temperature on the second ultimate stress. However, the experiments have been made at enough different temperatures to establish definitely the form of the curves of variation of the ultimate stress and fracture stress.

Figures 9 to 14 show the effect of temperature on the important strength indices. The effect of temperature on a strength index comprises the direct effect on the strength of the metal, and the superimposed effects on the amount of plastic deformation and the rate of hardening in the test made to determine the strength index. For the

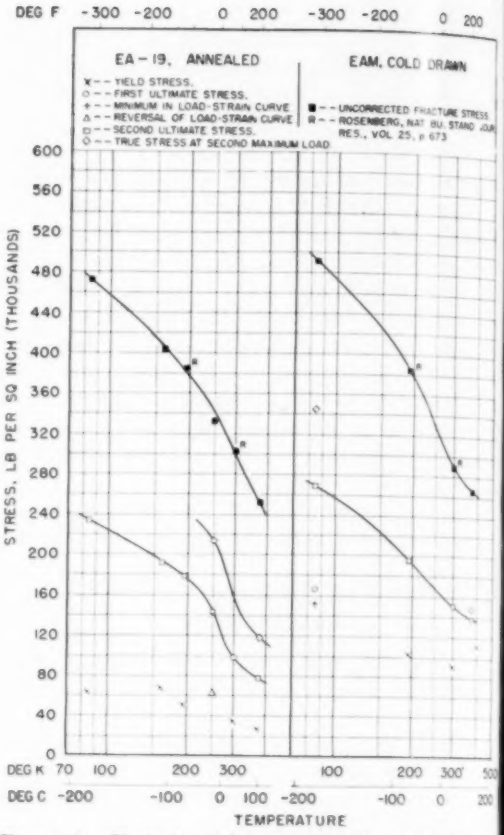

FIGURE 9. *Variation of the strength of plain 18:8 chromium-nickel steels with temperature.*

18:8 alloys, the superimposed indirect effects vary greatly with the temperature, and with the amount of plastic deformation required for determining the strength index. In studying the variation of the strength indices with temperature, consideration should be given to the relation between the direct and indirect effects of temperature on each index. The smaller the amount of plastic deformation required for determining the index, the less are the superimposed indirect effects, and the more nearly does the variation of the index with temperature represent the direct effect of temperature on the strength of the metal.

As the yield stress represents the strength of the metal at approximately the beginning of plastic strain, the influence of temperature in this index generally represents approximately the direct influence of temperature on the strength of the metal. The yield stresses of the 18:8 alloys a

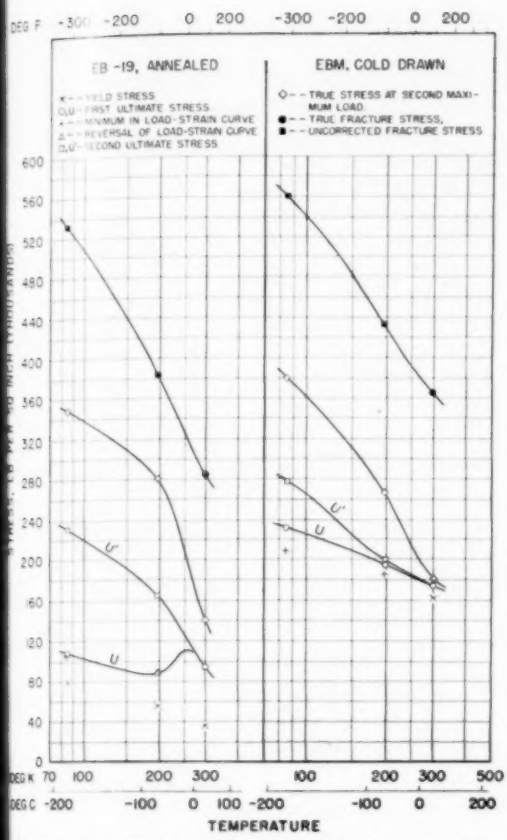
EB -19, ANNEALED
EBM, COLD DRAWN
X - - YIELD STRESS
O,U - - FIRST ULTIMATE STRESS
+ - - MINIMUM IN LOAD-STRAIN CURVE
Δ - - REVERSAL OF LOAD-STRAIN CURVE
□,U' - - SECOND ULTIMATE STRESS
○ - - TRUE STRESS AT SECOND MAXIMUM LOAD
● - - TRUE FRACTURE STRESS,
■ - - UNCORRECTED FRACTURE STRESS
DEG F -300 -200 0 200 -300 -200 0 200
DEG K 70 100 200 300 100 200 300 500
DEG C -200 -100 0 100 -200 -100 0 200
TEMPERATURE

FIGURE 10. *Variation of the strength of plain 18:8 chromium-nickel steels with temperature.*

room temperature were determined by means of transverse measurements during the tension tests. At low temperatures, the yield stresses were determined by means of the automatic load-extension diagrams. Because of the indefiniteness of the yield stress of the metastable austenitic alloys, the values obtained from the automatic diagrams are only approximately correct.

As shown in figures 9, 10, 12, 13, and 14, the increase in the yield stress with decrease in temperature is less rapid than the increase of any other index except the first ultimate stress. As would be expected, however, the greater the amount of prior plastic deformation, the less do the indices of resistance to plastic deformation diverge with decrease in temperature. After severe prior plastic deformation, the curves for the first and second ultimate stresses nearly coincide, as shown in the diagram for alloy *EBN* in figure 11.

The yield stress of the ferritic alloy (fig. 11) rises much more rapidly with decrease in temperature than the yield stress of the metastable austenitic alloys (figs. 9 to 14); the rise is about as rapid as for a carbon steel. As shown in a previous paper [8], a rapid increase of the yield stress with decrease in temperature is associated with a rapid decrease in ductility.

Next to the yield stress the first ultimate stress is the most suitable index for revealing the direct influence of temperature on the strength of an 18:8 alloy. However, when the nominal-stress versus extension curve merely reverses curvature without traversing a maximum, the nominal stress at the reversal may be used for the same purpose, and is nearly as satisfactory as the first ultimate stress. In some of the diagrams, it was possible to establish complete curves for both the first and second ultimate stresses. The relation between these

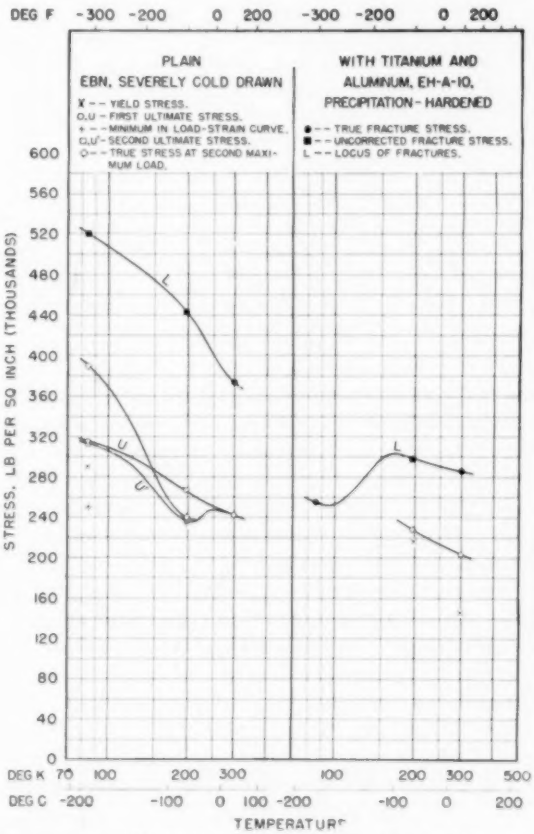
PLAIN
EBN, SEVERELY COLD DRAWN
WITH TITANIUM AND ALUMINUM, EH-A-10, PRECIPITATION-HARDENED
X - - YIELD STRESS.
O,U - FIRST ULTIMATE STRESS.
+ - - MINIMUM IN LOAD-STRAIN CURVE.
□,U' - SECOND ULTIMATE STRESS.
○ - - TRUE STRESS AT SECOND MAXIMUM LOAD.
● - - TRUE FRACTURE STRESS.
■ - - UNCORRECTED FRACTURE STRESS.
L - - LOCUS OF FRACTURES.
STRESS, LB PER SQ INCH (THOUSANDS)
DEG F -300 -200 0 200 -300 -200 0 200
DEG K 70 100 200 300 100 200 300 500
DEG C -200 -100 0 100 -200 -100 0 200
TEMPERATURE

FIGURE 11. *Variation of the strength of 18:8 chromium-nickel steels with temperature.*

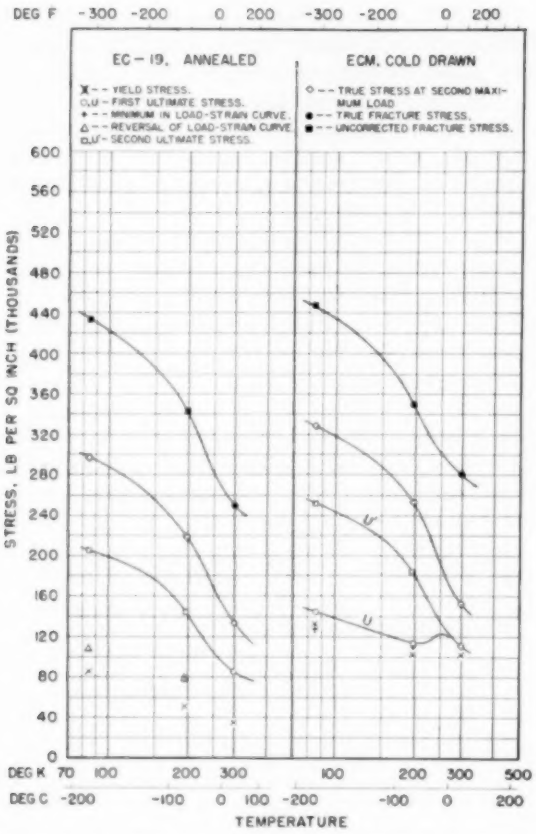

FIGURE 12. *Variation of the strength of 18:8 chromium-nickel steels containing titanium with temperature.*

curves is illustrated in the diagram for the moderately cold-drawn alloy *ECM* at the right of figure 12. This diagram should be compared with the nominal-stress curves obtained with the same alloy (fig. 3). Only one ultimate-stress value was obtained at room temperature, but two ultimate stresses were obtained at −78° C and at −188° C. Between room temperature and −78° C, therefore, the ultimate-stress curve branches as indicated in figure 12. Branching curves are shown also in the diagram at the right of figure 14 and in the diagram obtained with the moderately cold-drawn plain alloy *EBM* (fig. 10).

A similar branching of curves designated U and U' is shown in the diagram at the left of figure 10. Curve U in this diagram, however, is based partly on the small triangle representing the nominal stress at the point of reversal of the load-strain curve obtained at −78° C. As illustrated by the corresponding curve in figure 1, the nominal-stress approached a maximum, but rapid precipitation-hardening caused a reversal of curvature before a maximum was attained. The point of reversal of curvature (*RE*) evidently was very little higher than the maximum that would have been attained in the absence of the rapid phase change. Consequently, use has been made of the nominal stress represented by point *RE* in establishing curve U in figure 10 to represent as nearly as possible the direct influence of temperature on the strength of the annealed metal. A similar method has been used in deriving curve U in the diagram at the left of figure 13. A curve of similar form and significance could be based on the two small triangles

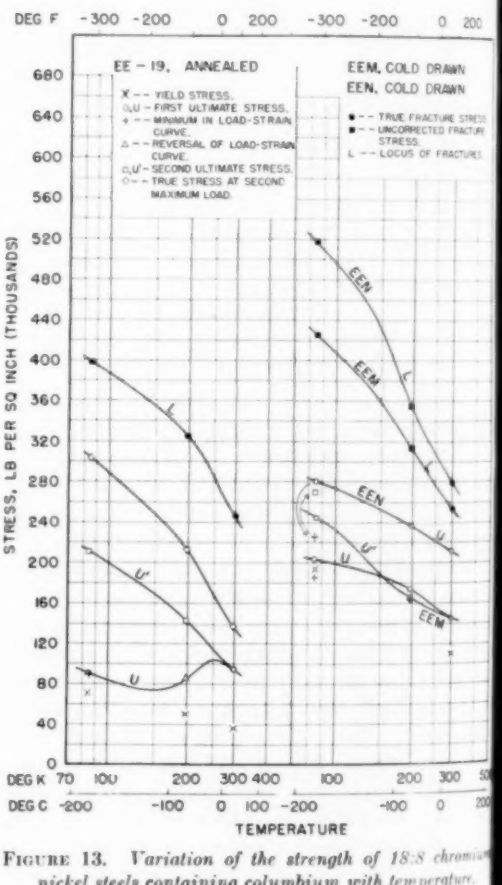

FIGURE 13. *Variation of the strength of 18:8 chromium-nickel steels containing columbium with temperature.*

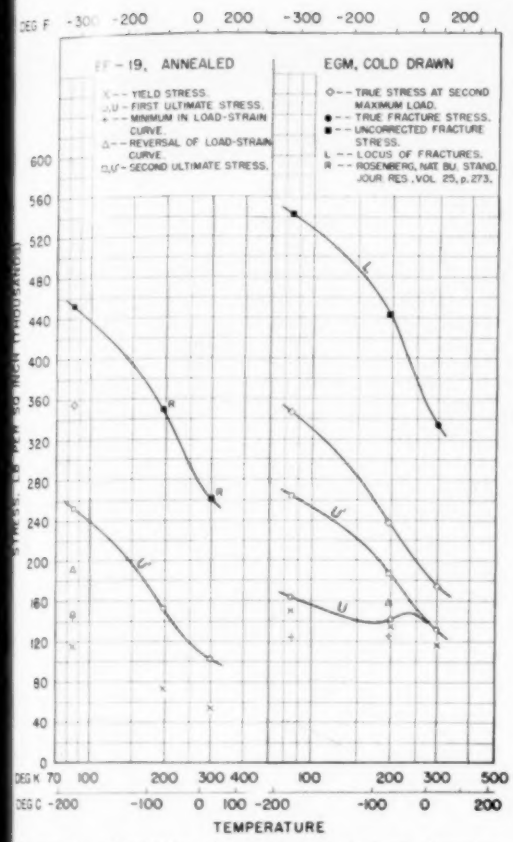

FIGURE 14. *Variation of the strength of 18:8 chromium-nickel steels containing molybdenum with temperature.*

in the diagram for the annealed alloy, at the left of figure 12.

Only the nearly straight part of curve U, however, represents approximately the direct effect of temperature on the strength of the metal. The upward bulge of the curve in a diagram for annealed metal or for moderately cold-drawn metal (figs. 10, 12, 13, and 14) is due to the superimposed effect of temperature on the strain necessary for the load to reach a maximum. As shown in the diagram for the annealed plain alloy *EB–19* (fig. 1), the strain necessary for the load to reach a maximum was much greater at room temperature than at low temperatures. This diagram should be compared with curve U in the diagram at the left of figure 10. A similar relationship is revealed by a comparison of the diagram at the right of figure 3 with curve U in the diagram at the right of figure 12, and by a comparison of the diagram at the left of figure 7 with curve U in the diagram at the right of figure 14. The upward bulge in curve U in diagrams for annealed alloys or for moderately cold-drawn alloys, therefore, is due to hardening of the metal during the relatively great plastic deformation necessary for the load to reach a maximum.

When the prior cold-work has been severe, the strain necessary for the load to reach a maximum is about as small at room temperature as at low temperatures. Illustrations of this relationship are shown in figure 2 and in the diagram at the left of figure 3.[6] As the plastic strain at the first maximum load was small at room temperature and at low temperatures, the corresponding curves U in figures 10, 11, and 13 are practically free from effects of variable plastic deformation. Unlike the curves obtained with the less severely cold-worked alloys or with the annealed alloys, these curves rise continuously with decrease in temperature. If yield-stress curves were drawn in these figures, their slopes would differ little from the slopes of curves U and from the slopes of the nearly straight parts of the curves U obtained with the softer alloys. These slopes represent approximately the direct effect of temperature on the strength of the 18:8 chromium-nickel steels.

All the curves of the variation of the second ultimate stress with temperature are affected by the phase changes induced by plastic deformation. In the absence of the rapid phase changes at low temperatures there would be no second ultimate stress. The divergence of curves U and U' is greatest for the annealed metals, and decreases with increase in the amount of prior cold-work. The influence of the rapid phase change at low temperatures is revealed most prominently by the steep rise of the curves representing the influence of temperature on the true stress at the second maximum and on the fracture stress. The course of each of these curves, however, indicates that with decrease in temperature below that of liquid air the influence of temperature on these strength indices gradually decreases.

[6] Comparison of ultimate stresses shows that the prior cold-work was more severe for these three alloys and for alloy *EEN* (fig. 13) than for any of the other alloys used in the investigation.

VII. Variation of Strength of 18:8 Chromium-Nickel Steel and of Some Other Metals Between Room Temperature and −252.8° C

The only extensive investigation of the mechanical properties of metals at the temperature of liquid hydrogen was by DeHaas and Hadfield [4]. Steels of many different compositions and a few nonferrous metals were included in their investigation. Only two chromium-nickel stainless steels were used. One was an 18:8 chromium-nickel steel; the other was a stable austenitic steel containing 14.4 percent of chromium and 59.3 percent of nickel. Yield stresses, ultimate stresses, and ductility values were determined at room temperature and at the temperature of liquid hydrogen, but fracture stresses were not determined.

In figure 15, results obtained by DeHaas and Hadfield at room temperature and at −252.8° C are compared with results obtained at the National Bureau of Standards within the range between room temperature and −188° C. The diagram shows results obtained by DeHaas and Hadfield with monel metal, electrolytic copper, the 18:8 alloy, and the stable austenitic chromium-nickel steel. For comparison, curves obtained with monel metal and oxygen-free copper have been reproduced from a paper by McAdam and Mebs [6], and two curves obtained with the annealed plain 18:8 alloy *EA-19* have been reproduced from figure 9. With the exception of the fracture-stresses derived from figure 9, only ultimate stresses are represented in figure 15.

With the 18:8 chromium-nickel steel and the stable austenitic steel, DeHaas and Hadfield, obtained almost identical results at room temperature. At −252.8° C, however, the ultimate stress of the 18:8 alloy was about 50 percent greater than that of the stable austenitic alloy. The strength index reported for the 18:8 alloy at this temperature undoubtedly is the second ultimate stress. The ultimate-stress curve obtained with the 18:8 alloy *EA-19* has been prolonged with little change of curvature, so as to pass through the point representing the result obtained by DeHaas and Hadfield with an alloy of the same type.

Moreover, the fracture-stress curve obtained with alloy *EA–19* has been prolonged with little change of curvature, so that an approximate estimate may be made of the probable breaking

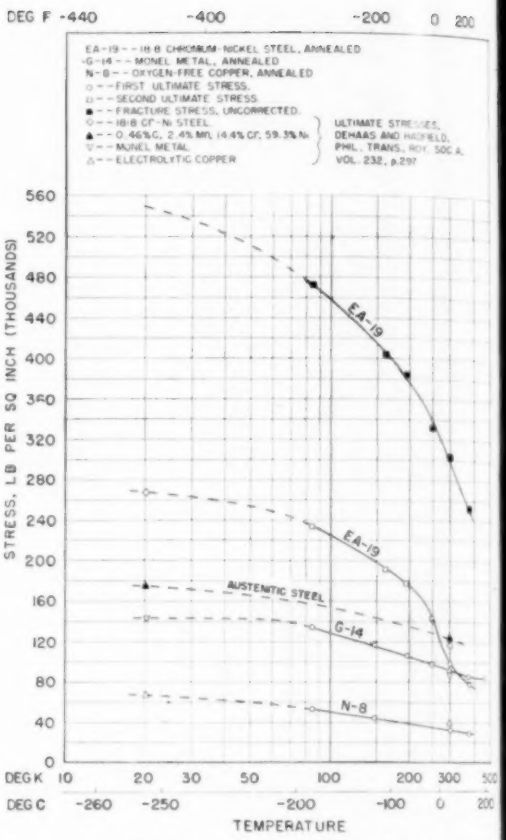

FIGURE 15. *Variation of the strength of various metals with temperature.*

stress of this alloy at the temperature of liquid hydrogen. The value thus obtained is of the same order as the breaking stresses of some of the 18:8 alloys in liquid air (figs. 10, 11, 13, and 14).

As shown in previous papers [6, 8, 9], and as illustrated in figure 15 by the curves for monel metal *G–14* and copper *N–8*, the variation of the strength indices for many nonferrous metals on this temperature scale is nearly linear between room temperature and −188° C. The results reported by DeHaas and Hadfield, however, indicate that the linear relationship does not continue between the temperatures of liquid air and liquid hydrogen. Although some of the reported ultimate stresses at the temperature of liquid hydrogen may be too low, the evidence indicates that the curves for the nonferrous metals and the stable austenitic alloy differ greatly in slope from the

curve obtained with the 18:8 alloy. The evidence also indicates that the great difference in strength of these chromium-nickel alloys at the temperature of liquid air is due to a difference in the stability of the austenite. The austenite in the alloy containing 14.4 percent of chromium and 59.3 percent of nickel evidently retains its stability during plastic deformation at the temperature of liquid hydrogen.

If curves to represent the variation of the first ultimate stress of the metastable austenitic alloys with temperature were included in figure 15, the slope between room temperature and −188° C would differ little from the slopes of the curves obtained with monel metal and copper, and from the probable slope of a curve obtained with the stable austenitic steel. The slopes of these curves represent approximately the direct effect of temperature on the strength of the metals. The difference between these slopes and the slope of the curves for the 18:8 alloy is due to the superimposed effect of the variation in the amount of phase-change with temperature. This variation becomes less with decrease in temperature as the proportion of untransformed austenite remaining after deformation of the specimen in the tensile test becomes less as the temperature is lowered. As the temperature approaches that of liquid air, possibly all or nearly all of the austenite is transformed to ferrite by the plastic deformation.

VIII. Influence of Notches on Mechanical Properties

Figure 16 shows the results of a brief investigation of the influence of notches on the strength indices of 18:8 alloys throughout a range between room temperature and −188° C. The alloys used in obtaining these two diagrams are the same that were used in obtaining the diagram at the left of figure 11 and the diagram at the right of figure 12. The curves representing results obtained with unnotched specimens are the same in figure 16 as in the corresponding diagrams of figures 11 and 12. A slight distinction between the first and second ultimate stresses could be observed in some specimens with 150° notch angle, but no distinction could be made when the angle was smaller.

Even when the angle was 50°, however, the plastic strain necessary for the load to reach a

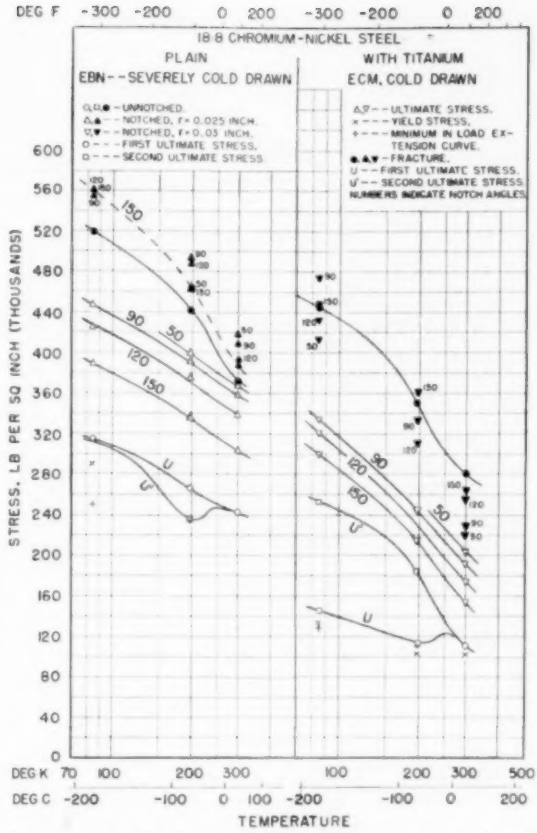

FIGURE 16. *Combined influences of notches and low temperatures on the tensile properties of 18:8 chromium-nickel steel.*

maximum at low temperatures was more than that for an unnotched specimen at the first maximum. Although the ductility decreased with decrease in the notch angle and with decrease in temperature, the combined influence of these two variables on the ductility was less for the 18:8 alloys than for pearlitic steels. At −188° C, the strain at fracture of a 50° specimen was about 26 percent ($A_0/A=1.26$). Moreover, the breaking stress of this specimen at −188° C was high, although the specimen fractured before the tensile load reached a maximum. These unusual properties suggest that the ultimate stresses of the notched specimens were appreciably increased by the phase change during plastic deformation. This phase change evidently contributes to the toughness of both notched and unnotched specimens.

Acknowledgment is made to D. H. Woodard, W. D. Jenkins, Fannie Wilkinson, and Lavaria Weinrich for general assistance in the experiments and the preparation of the illustrations.

IX. References

[1] R. H. Aborn and E. C. Bain, Trans. Am. Soc. Steel Treating **18,** 837 (1930).

[2] J. B. Austin and O. S. Miller, Trans. Am. Soc. Metals **28,** 743 (Sept. 1940).

[3] E. W. Colbeck, W. E. MacGillivray, and W. R. D. Manning, Trans. Inst. Chem. Engrs. **11,** 89 (1933).

[4] W. J. DeHaas and Sir Robert Hadfield, Phil. Trans. Roy. Soc. [A] **232,** 297 (1933 to 1934).

[5] V. N. Krivobok and R. A. Lincoln, Trans. Am. Soc. Metals **25,** 637 (1937).

[6] D. J. McAdam, Jr. and R. W. Mebs, Am. Soc. Testing Materials **43,** 661 (1944).

[7] D. J. McAdam, Jr., R. W. Mebs, and G. W. Geil, Proc. Am. Soc. Testing Materials **44,** 593 (1944).

[8] D. J. McAdam, Jr., G. W. Geil, and R. W. Mebs, Proc. Am. Soc. Testing Materials **45,** 448 (1945).

[9] D. J. McAdam, Jr., G. W. Geil, and R. W. Mebs, Trans. Am. Soc. Metals **37,** 497 (1946).

[10] D. J. McAdam, Jr., G. W. Geil, and R. W. Mebs, Am. Inst. Mining Met. Engrs., Tech. Pub. 2220, Metals Technology, (August 1947).

[11] D. J. McAdam, Jr., G. W. Geil, and W. D. Jenkins, Proc. Am. Soc. Testing Materials **47,** 554 (1947).

[12] D. J. McAdam, Jr., G. W. Geil, and Frances Jane Cromwell, Am. Inst. Mining Met. Engrs., Tech. Pub. 2296, Metals Technology (Jan. 1948).

[13] N. B. Pilling, Proc. Am. Soc. Testing Materials Part 2, **30,** 278 (1930).

[14] L. B. Pfeil and D. G. Jones, J. Iron Steel Inst. **127,** No. 1, 337 (1933).

[15] C. B. Post and W. S. Eberly, Trans. Am. Soc. Metals **39,** 868 (1947).

[16] S. J. Rosenberg, NBS J. Research **25,** 673 (1940) RP 1347.

[17] R. Smith, E. H. Wycke, and W. W. Gorr, Am. Inst. Mining Met. Engrs., Tech. Pub. 2006, Metals Technology (June 1946); Trans. Am. Inst. Mining Met. Engrs. **167,** 313 (1946).

[18] E. E. Thum, The book of stainless steels (Am. Soc. Metals, Cleveland, Ohio, 1935).

[19] H. H. Uhlig, Trans. Am. Soc. Metals **30,** 947 (1942).

WASHINGTON, January 2, 1948.

U. S. Department of Commerce
National Bureau of Standards

Research Paper RP1883
Volume 40, May 1948

Part of the Journal of Research of the National Bureau of Standards

Absorption of X-Rays in Air

By Frank H. Day and Lauriston S. Taylor

Studies have been undertaken to determine the absorption in air of X-rays produced by voltages from 10 to 200 kv (constant potential) for various initial filtrations. A free-air ionization chamber on tracks is used to obtain absorption data over a 150-cm distance. No appreciable change in quality of X-rays is observed in this distance because of the air absorption. Hence, for short distances, effective air absorption coefficients for heterogeneous X-rays of various qualities have been determined.

I. Introduction

The use, in recent years, of beryllium-window X-ray tubes with their high-intensity outputs of soft X-rays has developed a need for air-absorption corrections where distance is a factor in X-ray exposure measurements. Such, for example, is the case where the inverse-square law is used in computing the exposure at a point when the actual measurement is of necessity made at some other point. There is also need for corrections to be applied to the free-air type of ionization chamber due to air absorption between the limiting diaphragm of the chamber and the front edge of the collector plates. Since the exposure rate is specified in the plane of the limiting diaphragm, air-absorption along the path between the diaphragm and the collector plate results in the readings of the chamber being too low. This distance in the case of the guarded-field free-air standard for calibrations up to 200 kv at the Bureau of Standards is 21.1 cm, and for unfiltered radiations produced at, say, 50 kv, the necessary corrections may be considerable.

II. Apparatus and Experimental Procedure

A diagram of the experimental arrangement is shown in figure 1, where a mobile, free-air-guard-plate ionization chamber is indicated. The opening in its lead shield is 10 cm in diameter. This opening is adequate to accommodate, at any point along the track, the total area of X-rays determined by the fixed, limiting diaphragm, the diameter of which is 1.75 cm. The effective width of the collector plates is 10.2 cm, and the diameter of the beam with the chamber in its farthest position from the tube (position *B*, fig. 1) is 6.5 cm. The interelectrode separation is a fixed distance of 12.7 cm, and this is insufficient spacing to allow for the production and collection of all secondary electrons associated with a primary beam 6.5 cm in diameter. Hence, there is a slight loss of ionization, which earlier studies show does not exceed 1 or 2 percent.[1] No correction has been applied for this loss.

The charge collected in the ionization chamber at various points along the track is measured with a capacity compensator and string electrometer [2] with an accuracy of ± 1 percent. The exposure of the chamber is controlled by a timer operating a ½-in. lead shutter. The timer is actuated by an accurately controlled 60-cycle signal from the Radio Section of the Bureau of Standards.

Tungsten-target X-ray tubes with low inherent filtration are used in conjunction with various types and thicknesses of initial filtration. The term "initial filtration," as here used, refers to filters of aluminum, copper, or lead introduced between the X-ray tube and the column of air over which air-absorption measurements are made. The window thickness of the cerium glass in one X-ray tube used is 1.29 mm and of the beryllium in another tube, 1.5 mm.

Power supplied to the X-ray tube is furnished by a kenotron rectifier with a resistance-capacitance filter incorporated to reduce the ripple to

[1] Lauriston S. Taylor, George Singer, and A. L. Charlton, Am. J. Roent. **41**, 256 (1939).
[2] Lauriston S. Taylor, BS J. Research **6**, 807 (1931) RP306.

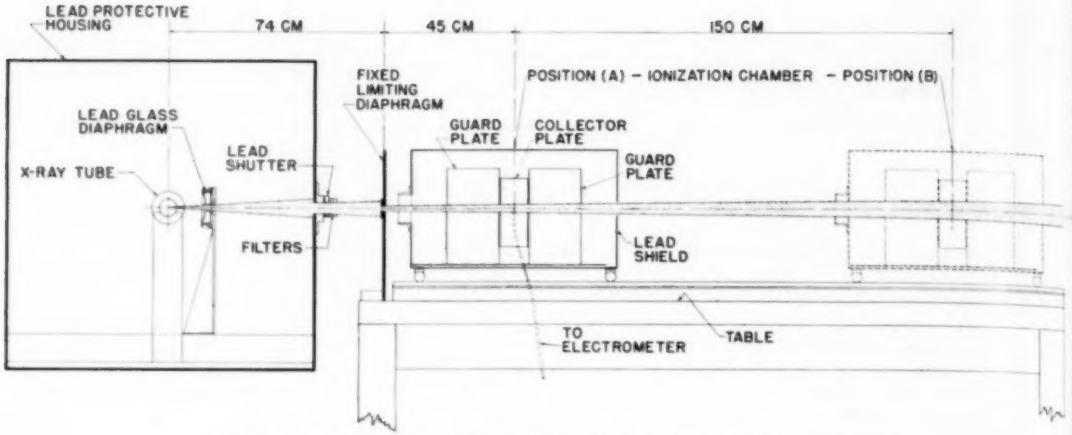

FIGURE 1. *Experimental arrangement for air absorption measurements.*

0.05 percent per milliampere current drain. The tube currents used are not in excess of 10 ma.

The voltage input to the rectifier units is constant to 0.25 percent or better, the 208-volt commercial supply being fed through a voltage stabilizer. The voltage to the rectifier units is then varied by induction regulator control. It is estimated that the absolute direct-current voltage applied to the X-ray tubes is known to an accuracy of 1 or 2 percent.

The filament voltage of the X-ray tubes is stabilized by an electronic voltage stabilizer in the ground circuit feeding through an insulating transformer. The output of the stabilizer is also manually controlled by an adjustable-ratio autotransformer to reduce long-period fluctuations.

In view of the above-described stabilization, the variation in quantity of X-ray output over a period of exposure of 10 seconds or more is not greater than 0.5 percent. This is also verified from previous experience on fluctuations in X-ray output of this equipment, as determined by the Bureau's standard chamber for measurements up to 200 kv.

III. Observations and Calculations

Under steady operating conditions of the X-ray tube, the ionization chamber is exposed for a given number of milliampere-seconds at successive points along the track. The ratio of the ionization currents measured at two points along the track is a measure of the air absorption between these points, inasmuch as the total flux passing through the limiting diaphragm is measured by the chamber, except for the part lost by air absorption.

Measurements are first made, using the beam in its minimum-filter condition. Filters of aluminum, copper, or lead are then interposed in the beam up to the point where the beam is rendered sufficiently homogeneous, so that further additions of filters will not lower the air-absorption coefficient by an appreciable amount. This is illustrated (fig. 2) by the semilogarithmic plots of X-ray

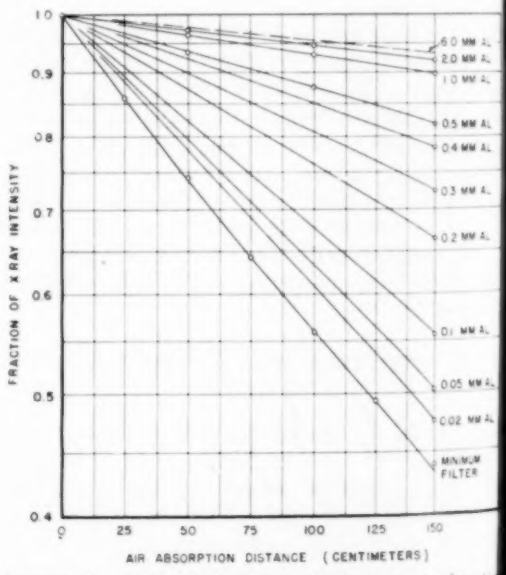

FIGURE 2. *Effect of aluminum filtration on air absorption of 50-kv X-rays produced by beryllium-window X-ray tube with inherent filtration 1.5 mm* Be.

intensity as a function of the length of the absorbing air path for the 50 kv X rays from the beryllium-window tube. Here it is observed that filtrations in excess of 2 mm of aluminum will not greatly affect the air absorption.[3] Similarly, it is found that for any voltage up to 200 kv, filtrations of 6 mm of Al, 0.2 mm of Cu, or 0.1 mm of Pb are sufficient for the attainment of a practical lower limit to the air absorption.

These studies are made with X rays of 200 kv and less, to voltages as low as transmission through filters will allow. Minimum-filter conditions allow observations on X rays as low as 7.5 kv from a beryllium-window tube. Even these 7.5-kv X rays show no great change in quality due to absorption in the air itself over the distance of observation, as indicated by a near straight-line semilogarithmic plot in figure 3. Since the beam is effectively monochromatic, it is permissible to prepare tables of linear absorption coefficients involving a single term [4] for air under normal atmospheric conditions, (760 mm of mercury pressure and 22° C), these to be applied over short distances.

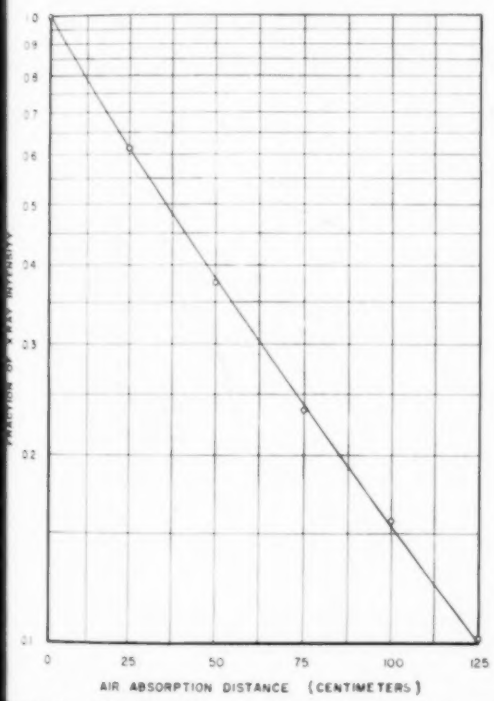

FIGURE 3. *Air absorption of 7.5-kv X-rays produced by beryllium-window tube with inherent filtration 1.5 mm* Be.

[3] The curve for 6-mm filtration was not observed at this voltage because of the extremely long exposure which would be necessary. At 100 kv, however, the difference between the 2-mm and the 6-mm curves is approximately 1 percent. The difference would not be greater than this in the case of 50-kv rays, for the same amount of filter would render the beam more homogeneous in the latter case.

Tables 1, 2, and 3 give effective linear absorption coefficients, μ (cm^{-1}) for air, where μ is used in the formula, $I_X = I_0 e^{-\mu X}$, I_X being the intensity at a distance X cm beyond the point where the original intensity, I_0, is measured. The X-ray beam is here considered to be parallel.

TABLE 1. *Linear absorption coefficients for X-rays of air under atmospheric conditions obtained with beryllium-window X-ray tube*

Voltage	Absorption coefficient (μ)				
	Minimum filtration [1]	Added filtration			
		0.05 mm Cu	0.1 mm Cu	0.2 mm Cu	0.1 mm Pb
kv	cm^{-1}	cm^{-1}	cm^{-1}	cm^{-1}	cm^{-1}
50	5.8×10^{-1}	3.5×10^{-2}	1.5×10^{-3}	0.5×10^{-3}	0.3×10^{-4}
60	5.6	3.1	1.2	.4	.3
70	5.5	2.8	1.1	.4	.3
80	5.3	2.5	1.0	.4	.3
90	5.2	2.2	0.9	.3	.3
100	5.1	2.0	.8	.3	.3
120	4.8	1.6	.7	.3	.3
140	4.6	1.3	.6	.3	.3
160	4.3	1.1	.5	.3	.3
180	4.1	1.0	.5	.3	.3
200	3.9	0.8	.4	.3	.3

[1] Minimum filtration is 1.5 mm of beryllium plus 119 cm of air.

Data in these tables are derived by calculating μ for air between 119 cm and 269 cm from the tube target. Errors due to change in quality of the X-rays will be involved in applying these data to determine intensities at great distances [5] from the target, and, also, at distances a few centimeters from the target. However, within the range of approximately 1 to 3 m from the target, these coefficients may be applied with little error.

For ready reference, some air absorption correction factors have been prepared and are shown

[4] To accurately specify the absorption of a heterogeneous beam, it is necessary to employ an expression that is the sum of exponential terms involving different absorption coefficients.

[5] "Great distances", as here used, refers to the absorption by a sufficient quantity of air to reduce the intensity of the original beam by several half-value layers. However, reductions of the order of only one half-value layer, such as observed in this experiment (fig. 2), show very little quality dependence.

TABLE 2. *Linear absorption coefficients for X rays of air under atmospheric conditions obtained with beryllium-window X-ray tube*

Voltage	Absorption coefficient (μ)							
	Minimum filtration [1]	Added filtration						
		0.05 mm Al	0.2 mm Al	0.5 mm Al	1.0 mm Al	2.0 mm Al	4.0 mm Al	6.0 mm Al
kv	cm^{-1}	cm^{-1}	cm^{-1}	cm^{-1}	cm^{-1}	cm^{-1}	cm^{-1}	cm^{-1}
7.5	20.5×10^{-3}							
10	12.9	9.7×10^{-3}	8.3×10^{-3}					
15	7.8							
20	6.9	5.3	3.9	2.5×10^{-3}				
30	6.1	4.9	3.3	1.8	0.9×10^{-3}	0.8×10^{-3}		
40	5.9	4.8	3.0	1.5	.8	.6		
50	5.8	4.6	2.8	1.4	.7	.6	0.5×10^{-3}	0.4×10^{-3}
60	5.6	4.5	2.7	1.3	.7	.6	.5	.4
70	5.5	4.4	2.6	1.2	.7	.5	.5	.4
80	5.3	4.3	2.5	1.1	.6	.5	.5	.4
90	5.2	4.2	2.4	1.0	.6	.5	.4	.4
100	5.1	4.1	2.3	0.9	.6	.5	.4	.4

[1] Minimum filtration is 1.5 mm of beryllium plus 119 cm of air.

TABLE 3. *Linear absorption coefficients for X rays of air under atmospheric conditions obtained with cerium glass-window X-ray tube*

Voltage	Absorption coefficient (μ)					
	Minimum filtration [1]	Added filtration				
		0.5 mm Al	1.0 mm Al	2.0 mm Al	4.0 mm Al	6.0 mm Al
kv	cm^{-1}	cm^{-1}	cm^{-1}	cm^{-1}	cm^{-1}	cm^{-1}
20	3.2×10^{-3}					
30	2.6	1.3×10^{-3}	0.9×10^{-3}	0.8×10^{-3}		
40	2.2	1.1	.8	.6		
50	2.1	1.0	.7	.6	0.5×10^{-3}	0.4×10^{-3}
60	2.0	.9	.7	.6	.5	.4
70	1.9	.9	.7	.5	.5	.4
80	1.8	.8	.6	.5	.5	.4
90	1.8	.8	.6	.5	.4	.4
100	1.7	.7	.6	.5	.4	.4
110	1.6	.7	.6	.5	.4	.4
120	1.5	.7	.6	.5	.4	.4

[1] Minimum filtration is 1.29 mm of cerium glass plus 119 cm of air.

in figures 4, 5, 6, and 7. For a parallel beam, the air absorption correction factor, C, is taken to be,

$$C=\frac{I_X}{I_0}.$$

In the case of a diverging beam, it may be defined as,

$$C=\frac{I'_X}{I'_0}\left(\frac{X_0+X}{X_0}\right)^2,$$

where I'_0 and I'_X are the intensities measured by r-meter [6] at distances X_0 and $X+X_0$ cm, respectively, from the tube target.

The correction factor, C, may be used in calculating intensities at various points, where a thimble chamber [6] measurement is made at one point only. Its application in field use is to determine the intensity at one position by air ionization measurement, calculate by inverse-square law the intensity to be expected at some distance farther from the

[6] John A. Victoreen, Medical physics, p. 1370–1382 (The Year Book Publishers, Inc., Chicago, Ill., 1944).

source, if it were operating alone as a reducing factor, then, multiply this intensity by the air absorption correction factor to determine the true intensity. If the intensity is to be determined at some point closer to the source than the ionization measurement is made, the reciprocal of the air absorption correction factor will be used as the multiplying factor.

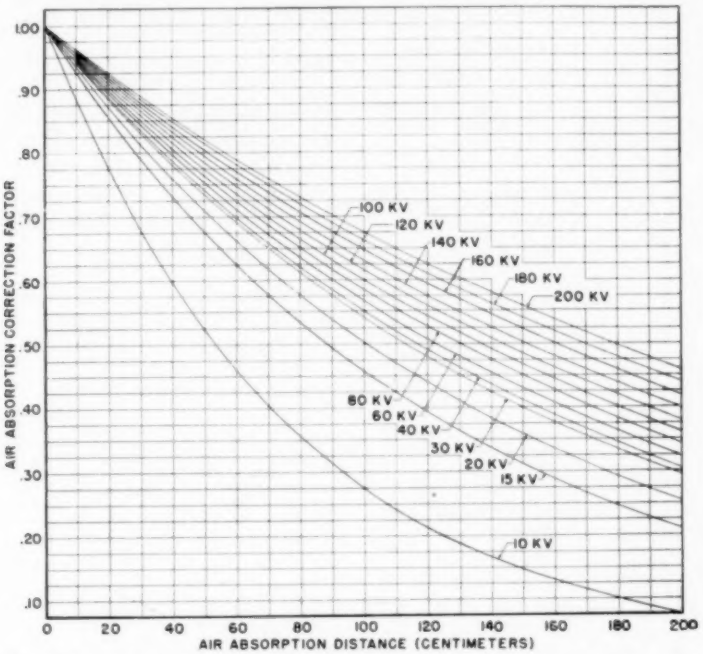

FIGURE 4. *Air-absorption reduction in intensity of minimum-filter X-ray beam from beryllium-window tube with inherent filtration 1.5 mm* Be.

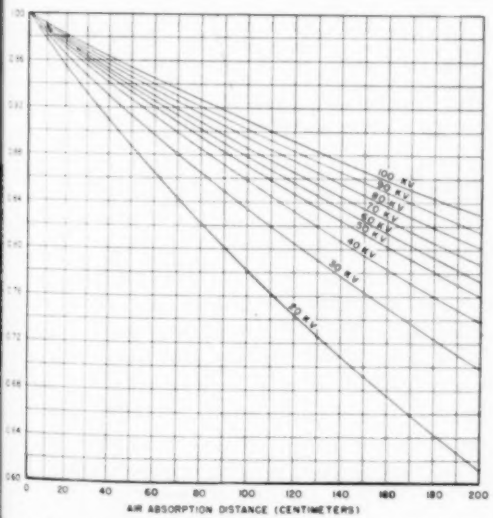

FIGURE 5. *Air-absorption reduction in intensity of X-ray beam filtered by 0.5 mm of* Al.

(Inherent filtration of X-ray tube used is 1.5 mm Be.)

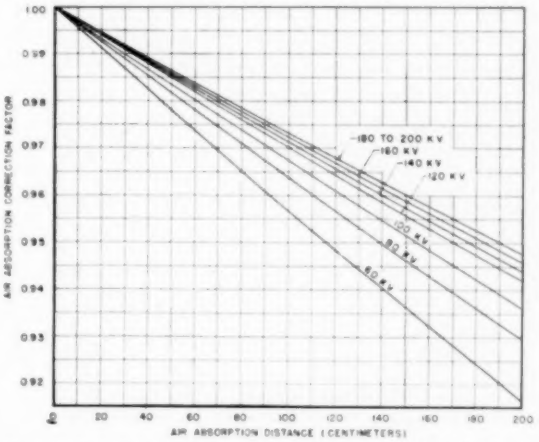

FIGURE 6. *Air-absorption reduction in intensity of X-ray beam filtered by 0.2 mm of* Cu.

(Inherent filtration of X-ray tube used is 1.5 mm Be.)

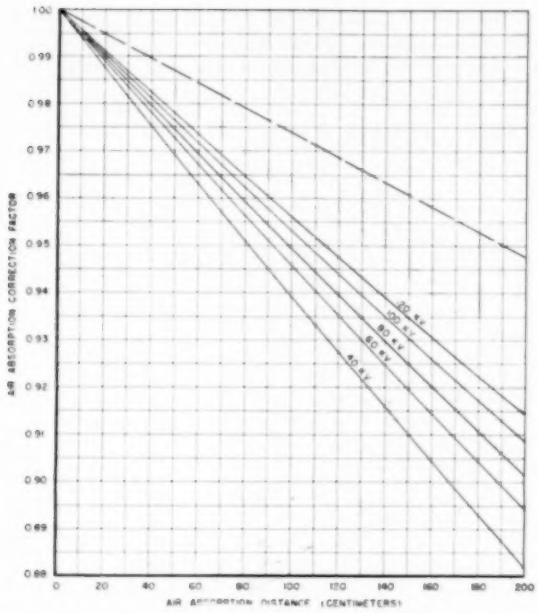

FIGURE 7. *Air-absorption reduction in intensity of X-ray beam filtered by 2.0 mm of* Al (*solid lines*).

Dashed line indicates reduction produced by 0.1 mm of Pb filter for X-rays of all qualities from 50 to 200 kv. (Inherent filtration of X-ray tube used is 1.5 mm Be.)

In cases where the graphs do not cover the conditions desired, the air absorption correction factor may be calculated, using the absorption coefficients given in tables 1, 2, and 3, and the equation, $C=e^{-\mu X}$. As an example of this calculation, table 3 indicates that μ for 40 kv with 1.0 mm Al of added filtration is 0.8×10^{-3} cm^{-1}. C is then defined for arbitrary values of X beyond 119 cm from the tube target. It is convenient to arrange the work in tabular form, as follows:

X	μX	$e^{-\mu X}$
cm		
25	0.02	0.98
50	.04	.96
100	.08	.92
150	.12	.89
200	.16	.85

IV. Free-Air Chamber Versus Thimble-Chamber Air-Absorption Data

That the air absorption factors determined with the free-air chamber are applicable also to thimble chamber use is indicated by reference to table 4. In this case, the limiting diaphragm is removed and a 25-r thimble chamber is placed at the midpoint of the collector plates of the free-air chamber, the latter chamber being here used only as a vehicle for transport of the thimble chamber. Data obtained are at 90 kv with no filtration other than 1.29 mm of cerium glass, the tube window thickness.

TABLE 4. *Comparison of air absorption data for 90-kv X-rays obtained by thimble ionization chamber with that obtained by free-air ionization chamber under minimum filter condition (1.29 mm of cerium glass)*

Distance, X, of air absorption [1]	Intensity, as measured by thimble chamber [2]	Thimble chamber intensity calculated to indicate air absorption only [3]	Intensity as measured by free-air chamber
cm	*percent*	*percent*	*percent*
0	100	100	100
25	64.9	95.1	94.9
50	44.9	90.7	91.0
75	32.5	86.4	87.0
100	24.5	83.1	83.1
125	18.9	79.4	80.3
150	15.0	76.7	77.7

[1] X is the ionization chamber travel distance, the zero position of which is 119 cm from the X-ray tube target.

[2] This includes inverse-square reduction in intensity superimposed upon air absorption reduction.

[3] The observed thimble chamber intensity times $(119+X/119)^2$ yields an intensity indicating the air absorption reduction only.

These data show reductions in intensity due both to the inverse-square law and to air absorption. The minimum target-to-thimble-chamber distance used is 119 cm. Multiplication of the thimble chamber readings by $(119+X/119)^2$, where X is the thimble-chamber travel distance, yields data indicating air absorption only. The data obtained in this manner with the thimble chamber agree within a percent with those using the free-air chamber as described in section III

In the case of soft X-rays, thimble-chamber measurement of the ratio of intensities between two points may be made without appreciable error, because there is no significant selective absorption of the soft components of the X-rays in traversing the amounts of air considered. The calibration of thimble chambers for soft X-rays, however, will be in error, the readings being less than those for hard X-rays, because there is appreciable absorption of the soft rays in the thimble chamber wall. The subject of such calibrations for soft X-rays will be discussed in another paper now in preparation.

The authors thank John H. Baltrukonis for obtaining much of the data reported above.

WASHINGTON, September 15, 1947.

U. S. Department of Commerce
National Bureau of Standards

Research Paper RP1884
Volume 40, May 1948

Part of the Journal of Research of the National Bureau of Standards

Location of the Galvanometer Branch for Maximum Sensitivity of the Wheatstone Bridge

By F. Ralph Kotter

The battery and galvanometer connections to a Wheatstone bridge may be interchanged without altering the condition for balance. One of the combinations will give a higher sensitivity than the other, but the calculation of the better arrangement is often somewhat tedious. This paper presents a "rule-of-thumb" method of determining the better arrangement, which requires only a knowledge of the resistance of the bridge arms and the value of the external critical damping resistance of the galvanometer.

The battery and galvanometer connections to the Wheatstone bridge may be interchanged without affecting the condition of balance of the bridge. One of the arrangements will usually be more sensitive than the other.

The question of which connection would give the higher sensitivity was investigated by Maxwell.[1] His conclusions, which have formed the basis for most subsequent treatments of the subject, were based on the assumption that the battery would be the limiting factor in the sensitivity, whereas now batteries that will supply more energy than can be dissipated as heat in the bridge arms are universally available. Wenner [2] has recently discussed the problem of the connection of the galvanometer branch under conditions of modern laboratory practice, considering the limiting power in the bridge arms and assuming that the galvanometer is always used critically damped or with the same percentage of critical damping.

It has been found that Wenner's analysis may be extended to give a simple rule of thumb method for determining the better position for the galvanometer branch. This method requires only a knowledge of the resistances of the bridge arms and the value of resistance required to produce critical damping of the galvanometer. As will be subsequently proved, the rule [3] to be followed is:

Calculate the resistance of the bridge between each pair of opposite branch points with galvanometer and battery circuits open. Compute the ratio or the reciprocal ratio, whichever is less than unity, of each of these "bridge resistances" to the external critical damping resistance of the galvanometer. Connect the galvanometer to the pair of branch points for which the ratio is nearer unity.

The rule given above assumes (1) that the galvanometer is to be used with critical damping, (2) that the limitation on the maximum power is the same for each arm of the bridge, and (3) that the voltage applied to the bridge is sufficient to dissipate this amount of power in one arm and no greater amount in any arm of the bridge. Under these conditions the rule is perfectly general, applying to all values of bridge ratios, bridge arm resistances, and galvanometer external critical damping resistances.

Perhaps more frequently than not, it is desirable to use the galvanometer slightly underdamped. In that event the above rule applies if the required calculations are made using the value of external damping resistance that has been found desirable rather than the critical damping resistance.

Proof.—The validity of the rule stated above will be established by determining, for all possible values of the galvanometer external critical damping resistance, the relative sensitivities and relative values of the ratios of bridge resistances to damping resistance for the two possible locations of the galvanometer branch in a Wheatstone bridge. Subject to the conditions of balance, the ratios

[1] J. C. Maxwell, A treatise on electricity and magnetism **1**, 400 (1873).
[2] F. Wenner, J. Research NBS **25**, 229 (1940) RP1323.
[3] The possibility that this rule is valid was suggested to the author by J. L. Thomas of this Bureau. A similar but less precise rule is given by H. B. Brooks in the section titled, *Measurements and measuring apparatus*, of Pender and Del Mar's Electrical engineer's handbook **4**, section 5, p. 5, 3d ed. (John Wiley & Sons, Inc., New York, N. Y., 1936).

781956—48——5

and the resistances of the bridge arms may have any desired values.

There is no loss in generality in assuming the bridge arms to have the values shown in figure 1 and requiring that $n>p\geqq 1$. (The case of $n=p$ is trivial, since the bridges (a) and (b) are then identical.)

The bridge resistances across the galvanometer for the two cases are

$$W_a=\frac{nR(1+p)}{1+n}, \tag{1}$$

and

$$W_b=\frac{pR(1+n)}{1+p}. \tag{2}$$

It may be readily shown that $W_b>W_a$ for all values of n and p subject to the condition $n>p\geqq 1$:

$$\frac{W_a}{W_b}=\frac{n(1+p)^2}{p(1+n)^2}.$$

Let $n=p+q$, $(q>0)$. Then

$$\frac{W_a}{W_b}=\frac{p^3+2p^2+p^2q+p+2pq+q}{p^3+2p^2+p^2q+p+2pq+q(p^2+pq)}.$$

As $q>0$ and $p\geqq 1$, the denominator is larger than the numerator and $W_b>W_a$.

The sensitivities and resistance ratios to be compared are continuous functions of the galvanometer critical damping resistance; however, the functions are each two joined straight lines, with different slopes for the two parts. This is illustrated in figure 2, where curve "bridge a" shows

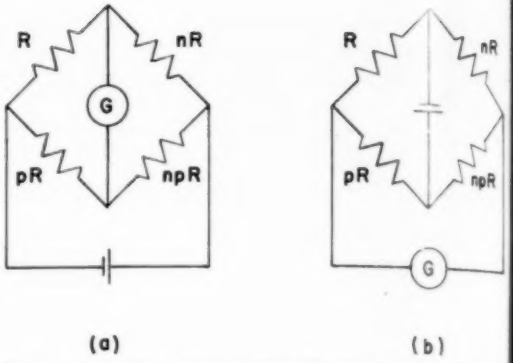

FIGURE 1. *Alternate connections of battery and galvanometer in the Wheatstone bridge.*

the variation of bridge sensitivity with galvanometer external critical damping resistance when the galvanometer is connected as shown in (a) of figure 1. Curve "bridge b" of figure 2 is the corresponding curve of sensitivity when the connection is that of (b) in figure 1. It is therefore necessary to carry out the proof in the following four cases:

Case 1, $V\leqq W_a$:

Let V represent the critical external damping resistance for the galvanometer and consider first $V\leqq W_a$. The ratios to be compared are V/W_a and V/W_b.

It has already been shown that $W_b>W_a$, therefore

$$\frac{V}{W_a}>\frac{V}{W_b}. \tag{3}$$

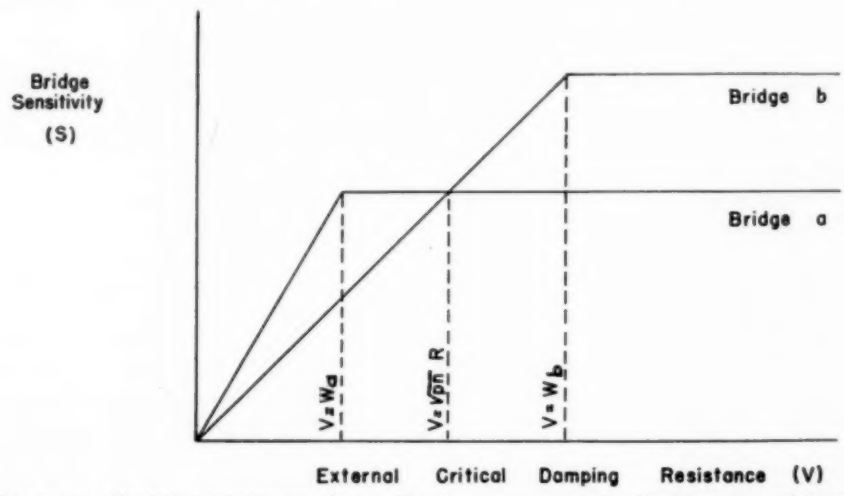

FIGURE 2. *Variation of bridge sensitivity with galvanometer external critical damping resistance.*

Case 2, $W_a < V \leqq \sqrt{pn}R$:

Now consider $W_a < V \leqq \sqrt{pn}R$. The ratios to be compared are W_a/V and V/W_b.

Dividing one ratio by the other and using eq. 1 and 2 gives

$$\frac{W_a/V}{V/W_b} = \frac{pnR^2}{V^2}. \tag{4}$$

This ratio is equal to unity for $V = \sqrt{pn}R$ and greater than unity for all values of V less than $\sqrt{pn}R$. Therefore,

$$\frac{W_a}{V} \geqq \frac{V}{W_b} \text{ for } V \leqq \sqrt{pn}R. \tag{5}$$

Case 3, $\sqrt{pn}R < V < W_b$:

Now consider $\sqrt{pn}R < V < W_b$. The ratios to be compared are again W_a/V and V/W_b, and eq. 4 shows that

$$\frac{W_a}{V} < \frac{V}{W_b} \text{ for } V > \sqrt{pn}R. \tag{6}$$

Case 4, $V \geqq W_b$:

In the range $V \geqq W_b$ the ratios to be compared are W_a/V and W_b/V.

It has already been shown that $W_b > W_a$, and consequently

$$\frac{W_a}{V} < \frac{W_b}{V}. \tag{7}$$

It has now been shown that the ratio involving W_a and V is larger than the ratio involving W_b and V for all values of $V < \sqrt{pn}\ R$, that the ratios are equal for $V = \sqrt{pn}\ R$ and that the ratio involving W_b and V is larger than the one involving W_a and V for $V > \sqrt{pn}\ R$. It remains then to be shown that the sensitivity of bridge *a* is greater than that of bridge *b* for $V < \sqrt{pn}\ R$, that the sensitivities are equal for $V = \sqrt{pn}\ R$, and that the sensitivity of *b* is greater than *a* for $V > \sqrt{pn}\ R$.

Since the power is greatest in the nR arm of the bridge of figure 1 a the resistance of this arm imposes the limitation on the voltage that may be applied to the bridge and Wenner's equation for the bridge sensitivity,[4] S_a, may be written

$$S_a = 2DE_{nR}\frac{R}{R+nR} \times \frac{V}{W_a},$$

where D is the voltage sensitivity of the galvanometer in scale divisions per unit electromotive force when the resistance in series with the galvanometer is V; E_{nR} is the maximum permissible potential drop in nR; and the other symbols have the meanings previously given them.

As is shown by Wenner, when the ratio V/W_a is less than or equal to unity its actual value is to be used in the equation for sensitivity; however, when the ratio V/W_a is greater than unity, it is to be replaced by unity in the equation. This assumes, as stated above, that the galvanometer damping is always adjusted to the same value either by series or parallel resistance as required.

Expressed in terms of the permissible power, P_{nR}, in the nR arm, the equation may be written

$$S_a = 2D\sqrt{P_{nR}}\sqrt{nR} \times \frac{R}{R+nR} \times \frac{V}{W_a}. \tag{8}$$

For the bridge in figure 1, b, the limitation is imposed by the pR arm, and in terms of the permissible power in it (P_{pR}) the sensitivity may be written

$$S_b = 2D\sqrt{P_{pR}}\sqrt{pR} \times \frac{R}{R+pR} \times \frac{V}{W_b}. \tag{9}$$

As it is assumed that the power limitations are the same for all arms of the bridge, $P_{pR} = P_{nR}$, and eq 8 and 9 may be rewritten

$$S_a = K\frac{\sqrt{nR}}{1+n} \times \frac{V}{W_a}, \tag{10}$$

$$S_b = K\frac{\sqrt{pR}}{1+p} \times \frac{V}{W_b}. \tag{11}$$

For values of V equal to or less than W_a, the ratio V/W_a is equal to or less than unity, V/W_b is less than unity, and the actual values are to be used in eq 10 and 11.

Then for $V \leqq W_a$, using values of W_a and W_b from eq 1 and 2,

$$S_a = \frac{KV}{\sqrt{nR}(1+p)},$$

$$S_b = \frac{KV}{\sqrt{pR}(1+n)},$$

$$\frac{S_a}{S_b} = \sqrt{\frac{p(1+n)^2}{n(1+p)^2}}.$$

The quantity under the radical has already been shown to be greater than unity; therefore,

$$S_a > S_b \text{ for } V \leqq W_a. \tag{12}$$

[4] F. Wenner, J. Research NBS **25**, 238 (1940) RP1323.

For $V=\sqrt{pn}R$, V/W_a is greater than unity, but V/W_b is less than unity, and the sensitivities are, from eq 10 and 11:

$$S_a=K\frac{\sqrt{nR}}{1+n}\times 1,$$

$$S_b=K\frac{\sqrt{pR}}{1+p}\times\frac{\sqrt{pn}R}{pR(1+n)}(1+p)=K\frac{\sqrt{nR}}{1+n}.$$

That is,

$$S_a=S_b \text{ for } V=\sqrt{pn}\,R. \tag{13}$$

Now it is evident that for any value of V less than $\sqrt{pn}\,R$, S_b will be less than $K\sqrt{nR}/1+n$, while for any value of V between W_a and $\sqrt{pn}\,R$, S_a is constant and equal to $K\sqrt{nR}/1+n$. Therefore,

$$S_a>S_b \text{ for } W_a<V<\sqrt{pn}\,R. \tag{14}$$

For values of V greater than $\sqrt{pn}\,R$, S_b will be greater than $K\sqrt{nR}/1+n$, while S_a remains constant at $K\sqrt{nR}/1+n$. Therefore,

$$S_b>S_a \text{ for } V>\sqrt{pn}\,R, \tag{15}$$

completing the proof.

WASHINGTON, January 2, 1948

U. S. Department of Commerce
National Bureau of Standards

Research Paper RP1885
Volume 40, May 1948

Part of the Journal of Research of the National Bureau of Standards

Second Dissociation Constant of Oxalic Acid from 0° to 50° C, and the pH of Certain Oxalate Buffer Solutions

By Gladys D. Pinching and Roger G. Bates

The second dissociation constant of oxalic acid was determined at intervals of 5 degrees from 0° to 50° C by measurement of the electromotive force of cells without liquid junction. Hydrogen and silver–silver-chloride electrodes were employed. The solutions were composed of potassium binoxalate, sodium oxalate, and sodium chloride. The value of the second dissociation constant, K_2, in the temperature range studied is given by the equation

$$-\log K_2 = \frac{1423.8}{T} - 6.5007 + 0.020095T,$$

where T is the absolute temperature. The thermodynamic quantities associated with the second dissociation step were calculated. The paH values of 8 solutions of potassium binoxalate and sodium oxalate in the ratio 1:5 were determined at 11 temperatures.

I. Introduction

As fixed points of reference on a standard scale of pH, it is desirable to have available several standard buffer solutions that differ not only in pH but in chemical character and ionic type. If these solutions are all of comparable stability and give rise to about the same liquid-junction potential when brought into contact with a saturated solution of potassium chloride, they will serve equally well for the calibration of the pH meter with glass electrode. For control purposes, however, some will be preferred on account of a higher buffer capacity. Others may be unsuitable for use with indicators or with the quinhydrone electrode because of specific unfavorable reactions or because the multivalent anions of which they are composed cause unusually large salt errors. Other buffer substances may poison the platinum-hydrogen electrode or may undergo catalytic reduction in contact with it. Hence, new standards of pH will usually find use. These may eventually be classified, on the basis of comparative studies, as either primary or secondary standards.

In the search for buffer mixtures that might partially bridge the gap in pH between acid potassium phthalate (pH 3.9 to 4.2 [1] [1]) and mixtures of primary and secondary alkali phosphates (pH 6.7 to 7.0 [2]), the oxalate system was considered. Aqueous mixtures of a primary and a secondary alkali oxalate in equal molal amounts have pH values near 4. If the same two salts are used in the molal ratio of 1:5, however, buffer solutions with pH from 4.5 to 4.8 can be obtained. These solutions are stable in contact with the platinum hydrogen electrode. Furthermore, pure sodium oxalate is available as an NBS Standard Sample. Although the relatively large concentration of bivalent anions may detract from the usefulness of these buffer solutions in some instances, oxalate mixtures can often be employed advantageously for control and standardization.

The second dissociation constant of oxalic acid at intervals of 5 degrees from 0° to 50° C was determined by the method of Harned and Ehlers [3] from the electromotive force of cells of the type

$$\mathrm{Pt;\ H_2}\ (g),\ \mathrm{KHC_2O_4}\ (m_1),\ \mathrm{Na_2C_2O_4}\ (m_2),\ \mathrm{NaCl}\ (m_3),\ \mathrm{AgCl}\ (s);\ \mathrm{Ag.} \qquad \text{(Cell A)}$$

[1] Figures in brackets indicate the literature references at the end of this paper.

The changes of free energy, heat content, entropy, and heat capacity that occur when the process

$$HC_2O_4^- = H^+ + C_2O_4^= \quad (1)$$

takes place in the standard state were computed from the dissociation constants and their temperature coefficients. The activity pH values (paH) of several buffer solutions composed of potassium binoxalate and sodium oxalate in the ratio of 1 to 5 moles were calculated. The activity coefficient of chloride ion in the chloride-free buffer solutions was evaluated by five different methods, all of which were found to yield nearly the same paH.

II. Experimental Procedures and Results

Oxalic acid, the neutral and acid oxalates of sodium and potassium, and potassium tetroxalate were compared in an effort to determine which were best suited to the preparation of standard buffer solutions. Solubility, drying characteristics, hygroscopicity, degree of hydration, thermal stability, and ease of purification were considered. Each of the salts, with the exception of potassium tetroxalate, was dried to constant weight at 105° C. The temperature was then raised in steps of 10 degrees and constant weight attained at each temperature. This procedure was continued until the increase of 10 degrees in temperature produced a loss in weight no greater than 0.01 percent of the weight of the sample, or until the substance decomposed. The dried samples were then exposed for 24 hours to air of 45-percent relative humidity at 25° C. The results of these experiments are listed in table 1, together with some other properties of these materials.

Potassium tetroxalate dihydrate could not be dried to constant weight, and when the temperature was raised sufficiently to drive off the water of hydration, the component oxalic acid began to sublime. Sodium oxalate is considerably less soluble than potassium oxalate. Nevertheless, sodium oxalate was selected because it is less hygroscopic and is available in pure form as an NBS Standard Sample. Inasmuch as sodium binoxalate could not be dried to constant weight, potassium binoxalate was chosen as the primary salt used in preparing the buffer solutions.

Reagent-grade potassium binoxalate was purified by two recrystallizations from water to which a small amount of potassium carbonate had been added [6]. Seven weight titrations of the product gave a mean of 100.03 percent, with an average departure from the mean of 0.03 percent. Phenolphthalein was used as indicator, and the endpoint was established by comparison with a buffer-indicator mixture adjusted to about pH 8.3. The sodium chloride used had been recrystallized from water. It was tested [7] and found to contain about 0.002 mole percent of bromide. The specific conductance of the water used to prepare the buffer solutions ranged from 0.4 to 0.7×10^{-6} mho.

TABLE 1. *Properties of oxalic acid and its sodium and potassium salts*

Material	Hydration	Decomposition temperature of anhydrous material	Drying temperature	[a] Moisture taken up by anhydrous material
		°C	°C	% of total weight
Oxalic acid	$2\ H_2O$	[b]	[b]	
Sodium oxalate	Anhydrous	350 [4]	105	
Potassium oxalate	H_2O	370 (vac.) [5]	105	2.6
Sodium binoxalate	H_2O	210 to 220 [4]	[c]	4.4
Potassium binoxalate	Anhydrous	300 [4]	130	0.02

[a] Exposed for 24 hr to air having 45-percent relative humidity.
[b] Sublimes.
[c] Does not come to constant weight.

An upward drift in the electromotive force of some of the earlier cells, most pronounced at temperatures above 25° C, was observed. It was discovered that this drift could be eliminated almost completely by guarding the buffer solutions from contact with the rubber stoppers. The intervening space was filled with pure hydrogen. The cause of the drift is as yet unexplained. Traces of sulfide, such as might be dissolved from the rubber, have been found not to have a large effect on the potential of the silver–silver-chloride electrode [7].

In view of the relatively low pH of the oxalate mixtures, no attempt was made to exclude atmospheric carbon dioxide while the solutions were being prepared. Dissolved air was subsequently removed, however, by passing pure hydrogen through the solutions. Other experimental details will be found in an earlier publication [8].

The electromotive force, in international volts, of cell (A) at 11 temperatures from 0° to 50° C is given in table 2. Each cell contained two hydrogen electrodes and two silver–silver-chloride

electrodes. Hence, each electromotive force value represents, in general, the mean of two results. The electromotive force has been corrected in the usual way to a partial pressure of 760 mm of hydrogen. In the first four series of solutions, the relative proportions of potassium binoxalate, sodium oxalate, and sodium chloride were 1 : 5 : 2.5. In the next two series, the molalities of sodium chloride were respectively the same as, and one-half of, the molalities of the acid salt. The solutions comprising the last series contained equal molal amounts of the three salts.

TABLE 2. *Electromotive force of cells of type (A) containing* KHC_2O_4 (m_1), $Na_2C_2O_4$ (m_2), *and* NaCl (m_3) *from 0° to 50° C*

m_1	Temperature, ° C										
	0	5	10	15	20	25	30	35	40	45	50
					$m_2=5m_1$; $m_3=2.5m_1$. Series 1						
0.03914	0.53738	0.54039	0.54344	0.54646	0.54953	0.55275	0.55624	0.55946	0.56276	0.56607	0.56942
.03910	.54469	.54785	.55110	.55427	.55755	.56113	.56479	.56825	.57171	.57521	.57871
.02019	.55606	.55952	.56302	.56644	.56999	.57372	.57780	.58153	.58529	.58912	.59295
.006545	.57643	.58038	.58420	.58818	.59233	.59655	.60081	.60491	.60910	.61334	.61757
.008654	.57933	.58336	.58741	.59136	.59544	.59963					
.007858	.58182	.58591	.59002	.59409	.59829	.60264	.60691	.61117	.61547	.61982	.62417
.006936	.58524	.58937	.59354	.59769	.60205	.60637	.61068	.61500	.61938	.62376	.62820
.005651	.59085	.59515	.59947	.60381	.60814	.61260	.61707	.62153	.62604	.63059	.63514
.004557	.59664	.60118	.60563	.60996	.61431	.61881	.62348	.62800	.63268	.63735	.64203
.003448	.60445	.60902	.61366	.61819	.62282	.62747	.63220	.63691	.64169	.64651	.65136
					$m_2=5m_1$; $m_3=2.5m_1$. Series 2						
0.04037	0.53654	0.53963	0.54268	0.54573	0.54889	0.55206	0.55515	0.55817	0.56164	0.56446	0.56778
.02989	.54549	.54879	.55209	.55547	.55893	.56236					
.02350						.56864					
.02192	.55354	.55704	.56048	.56400	.56755	.57117	.57469	.57827	.58178	.58544	.58914
.01733	.56001	.56363	.56723	.57093	.57466	.57843	.58211	.58585	.58966	.59348	.59735
.01113	.57229	.57616	.58005	.58401	.58793	.59192	.59582	.59987	.60389	.60797	.61204
.01032	.57438	.57826	.58221	.58622	.59023	.59427	.59839	.60237	.60625	.61064	.61482
.008392	.58010	.58411	.58816	.59228	.59646	.60073	.60479	.60900	.61325	.61749	.62181
.006037	.58939	.59357	.59783	.60217	.60652	.61081	.61537	.61970	.62417	.62865	.63318
.004162	.59927	.60373	.60816	.61269	.61722	.62180	.62638	.63095	.63561	.64026	.64500
					$m_2=5m_1$; $m_3=2.5m_1$. Series 3						
0.03866	0.53696	0.53992	0.54305	0.54619	0.54938	0.55262					
.02586	.54892	.55210	.55552	.55886	.56236	.56600	0.56921	0.57226	0.57606	0.57983	0.58338
.01955		.56020	.56380	.56732	.57091	.57473					
.01751	.55974	.56328	.56694	.57062	.57431	.57807	.58167	.58527	.58910	.59295	.59667
.01493		.56900	.57177	.57556	.57924	.58312	.58682	.59057	.59436	.59828	.60226
.01232	.56942	.57324	.57713	.58102	.58491	.58888	.59268	.59654	.60060	.60459	.60862
.008601	.57559	.57947	.58348	.58736	.59144	.59559	.59947	.60346	.60747	.61178	.61592
.007886	.58181	.58580	.58984	.59397	.59816	.60245	.60666	.61091	.61526	.61963	.62394
.003934	.60082	.60523	.60976	.61426	.61877	.62335	.62794	.63253	.63727	.64205	.64684

TABLE 2. *Electromotive force of cells of type (A) containing* KHC_2O_4 *(*m_1*),* $Na_2C_2O_4$ *(*m_2*), and* NaCl *(*m_3*) from 0° to 50° C—Continued*

m_1	Temperature, ° C										
	0	5	10	15	20	25	30	35	40	45	50
$m_2=5m_1$; $m_3=2.5m_1$. Series 4.											
0.03831	0.54476	0.54798	0.55118	0.55449	0.55782	0.56112	0.56452	0.56794	.....	.....	.....
.02527	.54978	.55312	.55646	.55984	.56326	.56677	.57020	.57374	0.57714	0.58092	0.58457
.02027	.55588	.55834	.56270	.56625	.56987	.57354	.57702	.58070	.58445	.58820	.59202
.01715	.56057	.56410	.56771	.57137	.57505	.57884	.58266	.58641	.59026	.59413	.59798
.01416	.56588	.56958	.57329	.57698	.58077	.58468	.58848	.59232	.59630	.60032	.60430
.01147	.57166	.57558	.57942	.58331	.58727	.59121	.59521	.59926	.60334	.60739	.61151
.009697	.57632	.58028	.58419	.58818	.59216	.59620	.60032	.60449	.60864	.61282	.61703
.007591	.58321	.58730	.59145	.59553	.59984	.60388	.60814	.61241	.61676	.62106	.62544
.005787	.59059	.59482	.59916	.60336	.60765	.61199	.61644	.62097	.62551	.63006	.63458
.003146	.60706	.61166	.61632	.62060	.62558	.63028	.63490	.63963	.64453	.64937	.65430
$m_2=5m_1$; $m_3=m_1$											
0.04392	0.55627	0.55964	0.56313	0.56660	0.57014	0.57376	0.57753	0.58096	0.58469	.....	0.59187
.04054	.....	.56220	.56554	.56911	.57272	.57627	.57978	.58343	.58718	0.59080	.59463
.02644	.....	.....	.....	.58197	.58577	.58965	.59390	.59783	.60185	.60580	.60977
.01330	.58943	.59367	.59776	.60212	.60641	.61062	.61508	.61939	.62380	.62831	.63262
$m_2=5m_1$; $m_3=0.5m_1$											
0.03982	0.57643	0.58025	0.58409	0.58800	0.59184	0.59574	0.59958	0.60347	0.60750	0.61162	0.61577
.02008	.58423	.58832	.59233	.59656	.60068	.60481	.60893	.61307	.61726	.62146	.62569
.01979	.59506	.59933	.60361	.60794	.61224	.61656	.62101	.62543	.62988	.63437	.63886
.01252	.60760	.61210	.61663	.62130	.62593	.63051	.63534	.64000	.64478	.64952	.65431
.01010	.61353	.61824	.62289	.62762	.63233	.63714	.64203	.64687	.65178	.65674	.66174
.008771	.61741	.62216	.62690	.63171	.63649	.64144	.64626	.65117	.65618	.66114	.66625
.007190	.62256	.62750	.63235	.63727	.64217	.64718	.65209	.65710	.66215	.66723	.67241
.006896	.....	.....	.....	.....	.....	.64874	.....	.....	.....	.....	.....
.006046	.....	.....	.....	.....	.....	.65230	.....	.....	.....	.....	.....
.005167	.63160	.63667	.64171	.64674	.65181	.65694	.66227	.66751	.67274	.67807	.68343
.004186	.63748	.64267	.64784	.65305	.65825	.66352	.66881	.67413	.67949	.68491	.69039
$m_1=m_2=m_3$											
0.09729	0.50111	0.50372	0.50622	0.50853	0.51112	0.51374	0.51625	0.51885	0.52150	0.52431	0.52707
.07340	.50911	.51182	.51452	.51716	.51992	.52262	.52539	.52842	.53107	.53399	.53685
.05902	.51519	.51800	.52083	.52357	.52632	.52935	.53232	.53528	.53830	.54135	.54448
.05485	.51716	.52006	.52295	.52575	.52864	.53156	.53455	.53755	.54060	.54365	.54678
.04188	.52487	.52791	.53096	.53392	.53702	.54016	.54319	.54634	.54952	.55282	.55611
.02945	.53457	.53787	.54112	.54428	.54751	.55076	.55437	.55773	.56110	.56460	.56813
.02065	.54419	.54767	.55114	.55452	.55779	.56128	.56514	.56871	.57231	.57599	.57973
.01039	.56326	.56704	.57085	.57463	.57846	.58226	.....	.....	.....	.....	.....

The most accurate and extensive results were obtained for the first four series, where the ratio of concentration of sodium chloride to that of potassium binoxalate was somewhat higher than in the other three series. For this reason, the second dissociation constant was evaluated from the electromotive force data for the first four series alone.

All of the cells were brought to initial equilibrium at 25° C. Another measurement at 25° C was made at the completion of the measurements at the lower temperatures and before the measurements at the higher temperatures were begun. In addition, a final value at 25° C was obtained. The initial and final values for the solutions of the first four series, from which the

dissociation constant was determined, differed on the average by about 0.10 mv. The electromotive-force values given for series 4 are the averages of two complete series of measurements, the mean deviations of which were about 0.10 mv.

III. Calculation of the Second Dissociation Constant

The dissociation constant is expressed in terms of the measured electromotive force, E, by the equation

$$pK_2' \equiv -\log K_2 - \beta^*\mu = \frac{(E-E^\circ)\,F}{2.3026RT} + \log m_{Cl^-} + \log \frac{m_{HC_2O_4^-}}{m_{C_2O_4^=}} + \frac{2A\sqrt{\mu}}{1+Ba^*\sqrt{\mu}}, \quad (2)$$

where E° is the standard potential of the cell [3,9], A and B are constants for the water medium at each temperature [10], a^* and β^* are adjustable parameters, and F, R, T, and μ have their usual significance. Equation 2 results from combining the equation for the electromotive force of the cell with the mass-law expression for the dissociation of binoxalate ion and with the Hückel formula [11] for the activity coefficients. The activity-coefficient term, for convenience designated $\log f_r$, takes the form

$$\log f_r \equiv \log \frac{f_{HC_2O_4^-} f_{Cl^-}}{f_{C_2O_4^=}} = \frac{2A\sqrt{\mu}}{1+Ba^*\sqrt{\mu}} + \beta^*\mu. \quad (3)$$

As a result of the appreciable acidic dissociation of the binoxalate ion, the penultimate term of eq 2 is not given with sufficient accuracy by $\log (m_1/m_2)$. Consideration of the equilibrium represented by eq 1 leads to the equality,

$$\frac{m_{HC_2O_4^-}}{m_{C_2O_4^=}} = \frac{m_1 - m_H}{m_2 + m_H}. \quad (4)$$

The hydrogen-ion concentration, m_H, was computed in one of two ways: from the electromotive force by the expression

$$-\log m_H = \frac{(E-E^\circ)F}{2.3026RT} + \log m_{Cl^-} - \frac{2A\sqrt{\mu}}{1+5B\sqrt{\mu}}, \quad (5)$$

or from the mass-law expression with the aid of a first estimate of pK_2,

$$-\log m_H = pK_2 - \log \frac{m_{HC_2O_4^-}}{m_{C_2O_4^=}} - \frac{4A\sqrt{\mu}}{1+5B\sqrt{\mu}}. \quad (6)$$

The value of m_H obviously depends upon the choice of a^* (that is, 5) in the last terms of eq 5 and 6. The error in m_H from this cause diminishes as the ionic strength decreases and disappears in the extrapolation to infinite dilution. Hence both methods were found to yield the same value of pK_2.

When the right side of eq 2 at 25° C was plotted as a function of ionic strength, the three curves of figure 1 were obtained. From top to bottom, these

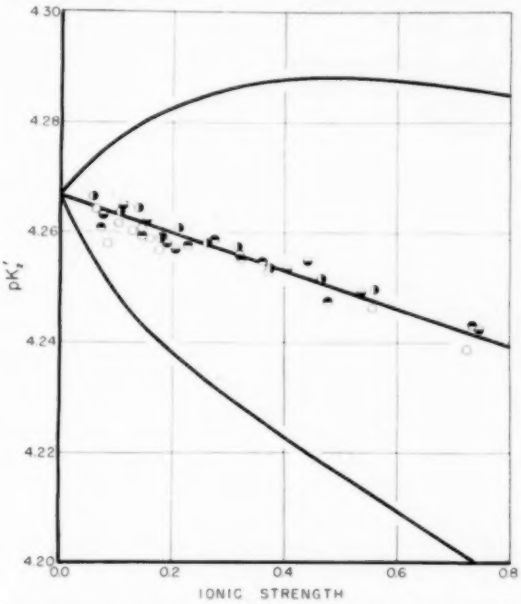

FIGURE 1. *pK'_2 at 25° C as a function of ionic strength for solutions in which $m_2 = 5m_1$ and $m_3 = 2.5m_1$.*

○, Series 1; ◒, series 2; ◓ series 3; and ◑, series 4.

three curves correspond to a^* values of 4.0, 5.0, and 6.0. An a^* value of 5.0 was found to yield values of $-\log K_2 - \beta^*\mu$ that were a linear function of ionic strength at each temperature studied. The slope, $-\beta^*$, of these straight lines was determined, and hence $-\log K_2$ (pK_2). The values of β^* are summarized in table 3, and those of $-\log K_2$ and K_2 are found in table 4. The dotted line in the figure represents pK_2' obtained for $a^* = 5.0$ when the acidic dissociation of the binoxalate ion was disregarded and m_1/m_2 employed as the ratio of the oxalate anions in eq 2. The last column of table 3 lists β°, the limit of β^* for 1:5 oxalate buffer solutions without sodium chloride. These values were obtained by linear extrapolation of β^* plotted with respect to m_{NaCl}/μ, the fractional contribution of sodium chloride to the total ionic strength [2]. No

TABLE 3. *Values of β^* from 0° to 50° C.*

Temperature	Relative proportions of KHC_2O_4, $Na_2C_2O_4$, and NaCl							
	1:1:1	1:5:2.5				1:5:1	1:5:0.5	1:5:0 (β°)
		Series 1	Series 2	Series 3	Series 4			
°C								
0	0.023	0.006	0.010	0.009	0.006	0.005	−0.002	−0.002
5	.027	.013	.013	.015	.012	.012	+.001	+.002
10	.032	.021	.018	.023	.026	.015	.008	.006
15	.038	.026	.024	.022	.026	.017	.009	.006
20	.042	.035	.026	.030	.031	.018	.009	.008
25	.051	.038	.032	.034	.037	.024	.018	.014
30	.056	.031	.038	.045	.041	.031	.024	.021
35	.064	.041	.045	.054	.046	.035	.032	.029
40	.070	.044	.054	.059	.056	.037	.036	.028
45	.074	.046	.058	.058	.064	.042	.042	.032
50	.078	.050	.062	.070	.063	.049	.045	.038

TABLE 4. *Values of pK_2 and K_2 from 0° to 50° C.*

Temperature	Series 1		Series 2		Series 3		Series 4		Average pK_2	$K_2 \times 10^4$
	pK_2	Average deviation	pK_2	Average deviation	pK_2	Average deviation	pK_2	Average deviation		
°C										
0	4.1987	0.0017	4.2006	0.0013	4.1999	0.0006	4.2037	0.0007	4.201	6.30
5	4.2057	.0014	4.2067	.0012	4.2062	.0009	4.2093	.0011	4.207	6.21
10	4.2164	.0018	4.2164	.0011	4.2176	.0012	4.2220	.0013	4.218	6.05
15	4.2292	.0015	4.2313	.0009	4.2298	.0011	4.2339	.0011	4.231	5.87
20	4.2456	.0012	4.2460	.0009	4.2457	.0012	4.2489	.0012	4.247	5.67
25	4.2654	.0013	4.2663	.0012	4.2657	.0014	4.2683	.0011	4.266	5.41
30	4.2863	.0015	4.2870	.0011	4.2861	.0010	4.2889	.0016	4.287	5.16
35	4.3124	.0021	4.3115	.0111	4.3094	.0018	4.3136	.0019	4.312	4.88
40	4.3385	.0017	4.3383	.0029	4.3360	.0012	4.3410	.0018	4.338	4.59
45	4.3690	.0022	4.3675	.0015	4.3656	.0015	4.3721	.0015	4.369	4.28
50	4.3993	.0020	4.3978	.0019	4.3973	.0021	4.4013	.0015	4.399	3.99

significant trend of a^* with ratio of chloride to oxalate was detected. The uncertainty in β° appears to be about ± 0.005.

These values of pK_2 are compared in table 5 with previous determinations of the second constant. It will be seen that the values of pK_2 given by Harned and Fallon [17] are higher by 0.02 to 0.03 than the results reported here. The same method and type of cell were employed in both investigations. Sodium binoxalate was used instead of the potassium salt, and the buffer solutions were composed of the three salts in the approximate molal proportions 1.9:1:1.5. In an effort to explain this discrepancy, two oxalate-chloride mixtures of the same compositions as two of the solutions used by Harned and Fallon were prepared. The electromotive force of cells of type (A) containing these solutions was measured at 25° C and found to agree fairly well with the results given in their paper. Furthermore, calculation of $pK_2 - \beta^*\mu$ at 25° C from the data of Harned and Fallon without consideration of the dissociation of binoxalate ion led to values apparently identical, when $a^* = 4.3$ was used, with those obtained by Harned and Fallon without a correction for hydrogen ion. As these authors have pointed out, their "uncorrected" pK_2 also agrees with the results of Parton and Gibbons [16] whose data were not corrected for acidic dissociation.

The discrepancy therefore seems to have arisen in the correction applied for the acidic dissociation

TABLE 5. *Comparison of values for the second dissociation constant*

Year	Observer	Temperature	Method	$K_2 \times 10^3$	pK_2
		° C.			
1908	Chandler [12]		Partition	4.1	4.39
			Conductance	4.9	4.31
1920	Drucker [13]	18	Emf conductance freezing point	6.9	4.16
1925	Britton [14]	18	H_2 calomel cells	13.4	3.87
1929	Dawson and Smith [15]		Catalysis of acetone-iodine reaction	7.2	4.14
1929	Parton and Gibbons [16]	25	Emf of cells without liquid junction, quinhydrone and Ag-AgCl electrodes.	5.012	4.300
			Recalculated[a]	5.41	4.267
1939	Harned and Fallon [17]	25	Emf of cells without liquid junction, H_2 and Ag-AgCl electrodes.	5.18	4.286
			Recalculated[a]	5.41	4.267
1941	Darken [18]	25	Conductance	5.3	4.28
1947	Present investigation	25	Emf of cells without liquid junction, H_2 and Ag-AgCl electrodes.	5.42	4.266

[a] Computed from the earlier data by the authors of this paper.

of the primary anion. Harned and Fallon state that the correction amounts to 0.007 in pK_2' for their lowest concentration (m_1=0.004516, m_2=0.008589) and is negligible for the highest (m_1=0.04945, m_2=0.02600). The corresponding corrections from the present calculation are 0.0253 and 0.0081. When pK_2 is calculated by the same procedure from the data of Harned and Fallon, of Parton and Gibbons, and of this investigation, substantially the same result is obtained.

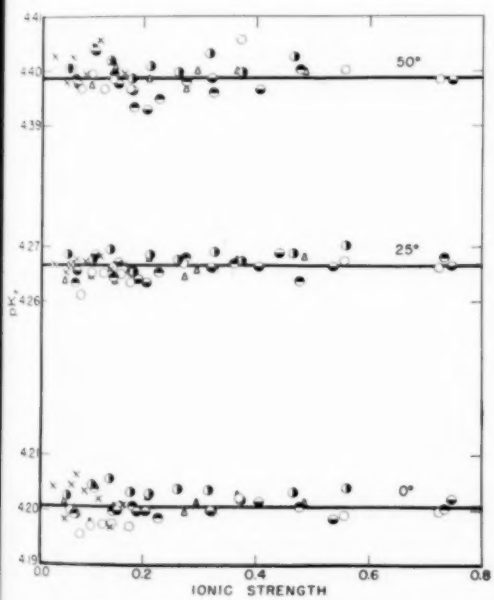

FIGURE 2. *pK_2 as a function of ionic strength.*

△, m_2=5m_1; m_3=2.5m_1; series 1. ◒, m_2=5m_1; m_3=2.5m_1; series 2. ◓, m_2=5m_1; m_3=2.5m_1; series 3; ◑, m_2=5m_1; m_3=2.5m_1; series 4. △, m_1=m_2=m_3. Data of Harned and Fallon [17].

The pK_2 value obtained in this investigation is plotted in figure 2 as a function of ionic strength and compared with corresponding values (crosses) computed from the data of Harned and Fallon [17]. The triangles indicate pK_2 computed from the electromotive force of the 1:1:1 series of solutions (see table 2). It is apparent that substantially the same dissociation constant is obtained from the three series of measurements, although the buffer ratio changes tenfold. The horizontal lines represent the average value of pK_2 listed in the next to the last column of table 4.

The variation of the dissociation constant with absolute temperature, T, is represented, with an average deviation of 0.0004, by

$$pK_2 = \frac{1423.8}{T} - 6.5007 + 0.020095\,T. \qquad (7)$$

The use of an equation of this form was suggested by Harned and Robinson [19]. The change of $-\log K_2$ with change of temperature is illustrated in figure 3.

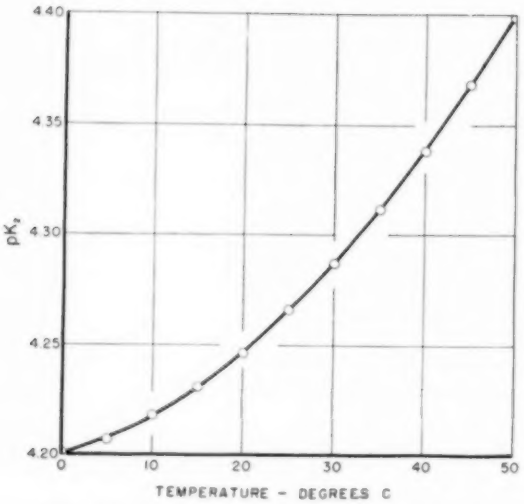

FIGURE 3. *Plot of pK_2 with respect to temperature.*

IV. Thermodynamic Quantities

From the parameters of eq 7, a calculation was made of the changes of free energy, of heat content, of entropy, and of heat capacity that accompany the process $HC_2O_4^- = H^+ + C_2O_4^=$ in the standard state. The equations relating these quantities to A, B, and C (which are respectively 1423.8, −6.5007, and 0.020095; compare eq 7 are given in an earlier paper [8]. The results of the calculation are listed in table 6.

V. Activity Coefficients and paH Values

It is evident from eq 3 that an expression for $\log f_{\prime}^{\circ}$, that is, the limit of $\log (f_{HC_2O_4} f_{C_2O_4})$ in 1:1 oxalate buffer solutions without chloride, can be

TABLE 6. *Thermodynamic quantities for the process* $HC_2O_4^- = H^+ + C_2O_4^=$

Temperature	ΔF°		ΔH°		ΔS°		ΔC°_p	
°C	*int j*	*cal*	*int j*	*cal*	*int j/deg*	*cal/deg*	*int j/deg*	*cal/deg*
0	21, 964	5, 250	−1, 447	−346	−85. 7	−20. 5	−210	−50
5	22, 403	5, 355	−2, 508	−600	−89. 6	−21. 4	−214	−51
10	22, 859	5, 464	−3, 587	−857	−93. 4	−22. 3	−218	−52
15	23, 336	5, 578	−4, 686	−1, 120	−97. 2	−23. 2	−222	−53
20	23, 832	5, 697	−5, 804	−1, 387	−101. 1	−24. 2	−226	−54
25	24, 347	5, 820	−6, 941	−1, 659	−104. 9	−25. 1	−229	−55
30	24, 882	5, 948	−8, 098	−1, 936	−108. 8	−26. 0	−233	−56
35	25, 436	6, 080	−9, 274	−2, 217	−112. 6	−26. 9	−237	−57
40	26, 008	6, 217	−10, 468	−2, 502	−116. 5	−27. 8	−241	−58
45	26, 600	6, 359	−11, 683	−2, 793	−120. 3	−28. 8	−245	−58
50	27, 211	6, 505	−12, 916	−3, 088	−124. 2	−29. 7	−249	−59

TABLE 7. *Log $f_{\prime}^{\circ}$ for solutions of* KHC_2O_4 *(m) and* $Na_2C_2O_4$ *(5m) from 0° to 50° C*

Temperature	Molality of potassium binoxalate							
	0.001	0.002	0.004	0.005	0.006	0.008	0.010	0.015
°C								
0	0. 103	0. 135	0. 175	0. 189	0. 201	0. 221	0. 237	0. 266
5	. 103	. 136	. 177	. 191	. 203	. 223	. 239	. 269
10	. 104	. 138	. 178	. 193	. 205	. 225	. 241	. 272
15	. 105	. 139	. 180	. 194	. 206	. 227	. 243	. 274
20	. 106	. 140	. 181	. 196	. 208	. 229	. 245	. 276
25	. 107	. 141	. 183	. 198	. 210	. 231	. 248	. 280
30	. 108	. 142	. 185	. 200	. 212	. 234	. 251	. 283
35	. 109	. 144	. 186	. 202	. 215	. 236	. 254	. 287
40	. 110	. 145	. 188	. 203	. 217	. 238	. 256	. 289
45	. 111	. 146	. 190	. 205	. 219	. 241	. 259	. 293
50	. 112	. 148	. 192	. 208	. 221	. 244	. 262	. 296

written in terms of the limiting values of a^* and β^*, namely, 5.0 and β°:

$$\log f_{\mathrm{C_2O_4}}^{\prime} \equiv \log \frac{f_{\mathrm{HC_2O_4}} f_{\mathrm{Cl}}}{f_{\mathrm{C_2O_4}}} = \frac{2A\sqrt{\mu}}{1+5B\sqrt{\mu}} + \beta^\circ \mu. \quad (8)$$

$\log f_{\mathrm{C_2O_4}}^{\prime}$ for eight oxalate buffer solutions is listed in table 7.

The quantity $-\log (f_{\mathrm{H}} f_{\mathrm{Cl}} m_{\mathrm{H}})$, readily obtainable from the electromotive force of cells of type A, has been proposed by Guggenheim [20] and by Hitchcock [21] as a unit of acidity. Its value for eight 1:5 oxalate buffer solutions without chloride was computed from a combination of eq 8 with the mass-law expression:

$$\mathrm{pwH} \equiv -\log (f_{\mathrm{H}} f_{\mathrm{Cl}} m_{\mathrm{H}})^\circ = -\log K_2 - \log \frac{m_{\mathrm{HC_2O_4}}}{m_{\mathrm{C_2O_4}}} - \frac{2A\sqrt{\mu}}{1+5B\sqrt{\mu}} - \beta^\circ \mu, \quad (9)$$

where the superscript zero indicates that chloride is absent. It should be noted that $-\log (f_{\mathrm{H}} f_{\mathrm{Cl}} m_{\mathrm{H}})^\circ$, which will be called pwH whether chloride is present or not, is a quantity with exact thermodynamic meaning. Its value in the oxalate buffer solutions is summarized in table 8.

TABLE 8. pwH *for solutions of* KHC_2O_4 *(m) and* $Na_2C_2O_4$ *(5m) in the absence of chloride from 0° to 50° C*

Temperature	Molality of potassium binoxalate							
	0.001	0.002	0.004	0.005	0.006	0.008	0.010	0.015
°C								
0	4.808	4.770	4.728	4.714	4.701	4.681	4.665	4.634
5	4.813	4.775	4.732	4.718	4.706	4.685	4.669	4.638
10	4.823	4.786	4.743	4.727	4.715	4.694	4.678	4.646
15	4.835	4.796	4.754	4.739	4.726	4.705	4.689	4.657
20	4.848	4.810	4.768	4.752	4.739	4.718	4.702	4.670
25	4.869	4.830	4.786	4.771	4.758	4.737	4.720	4.688
30	4.888	4.849	4.806	4.789	4.779	4.754	4.737	4.703
35	4.910	4.872	4.828	4.812	4.798	4.776	4.760	4.725
40	4.936	4.896	4.853	4.834	4.822	4.800	4.782	4.748
45	4.963	4.925	4.881	4.863	4.850	4.828	4.810	4.775
50	4.992	4.953	4.908	4.892	4.878	4.855	4.837	4.802

The definition of pH and the relative advantages of several possible scales of acidity have been discussed recently [22]. The pwH differs from paH by the logarithm of the activity coefficient of a single ionic species, a quantity that cannot be measured:

$$\mathrm{paH} = \mathrm{pwH} + \log f_{\mathrm{Cl}}. \quad (10)$$

Hence, some assumption must be made in order to relate f_{Cl} to measurable combinations of activity coefficients or to theoretical equations. Since no single assumption has as yet been assimilated into a generally accepted definition of paH, five scales based upon five different assumptions have been considered.[2] For the 1:5 oxalate buffers, these scales are defined by the following equations:

$$\mathrm{p_1H} = \mathrm{pwH} - \frac{A\sqrt{\mu}}{1+Ba_i\sqrt{\mu}}, \quad (11)$$

where the value for a_i is arbitrarily chosen;

$$\mathrm{p_2H} = \mathrm{pwH} + \log f_{\mathrm{HCl}}, \quad (12)$$

where f_{HCl} is the mean activity coefficient of hydrochloric acid;

$$\mathrm{p_3H} = \mathrm{pwH} - \frac{A\sqrt{\mu}}{1+5B\sqrt{\mu}} - \tfrac{1}{2}\beta^\circ \mu; \quad (13)$$

$$\mathrm{p_4H} = \mathrm{pwH} - \frac{A\sqrt{\mu}}{1+5B\sqrt{\mu}} + \beta^\circ \mu; \quad (14)$$

and

$$\mathrm{p_5H} = \mathrm{pwH} - \frac{A\sqrt{\mu}}{1+5B\sqrt{\mu}}. \quad (15)$$

In table 9, pwH and the five paH values, all at 25° C, are compared with the paH determined with a pH meter of the glass-electrode type calibrated at 4.01 with a 0.05-*m* solution of acid potassium phthalate [1]. For the computation of $\mathrm{p_2H}$, the average of f_{HCl} in pure solutions of sodium chloride and potassium chloride of the appropriate ionic strength was chosen in preference to its value in solutions of hydrochloric acid, in recognition of the probable specific influences of different cations

[2] These five assumptions have been discussed elsewhere [22, 23].

upon f_{Cl} in the buffer medium. This activity coefficient was computed from published electromotive force data [24, 25] with the use of Harned's equations for the activity coefficient of hydrochloric acid in mixtures with alkali chlorides [25]. A graphical comparison of p_2H, p_3H, p_4H, and p_5H as a function of ionic strength is made in figure 4. The upper and lower dotted lines locate p_1H when a_i is respectively 6 and 4. It is evident from table 9 and figure 4 that the five assumptions yield equivalent results at low concentrations and that the scales diverge to the extent of only 0.02 unit at an ionic strength of 0.24.

Tables 10 and 11 list the values of p_3H and p_5H for eight 1:5 oxalate buffer solutions at 11 temperatures from 0° to 50° C. The change of paH (taken as the mean of the closely agreeing p_3H and p_5H) with change of temperature is shown in figure 5.

The densities of three solutions of potassium binoxalate (m) and sodium oxalate ($5m$), in which m had the values 0.002, 0.008, and 0.015, were determined at 25° C with a picnometer that had a volume of approximately 57 ml. The ratio of the molar concentration of binoxalate, M, to molality,

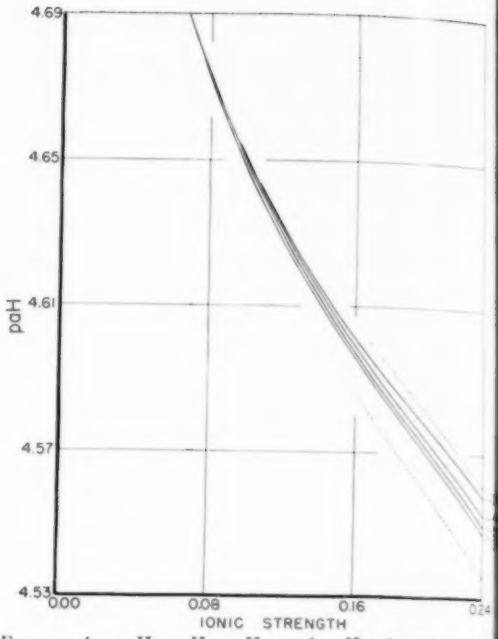

FIGURE 4. p_2H, p_3H, p_4H, *and* p_5H *of oxalate buffer solutions as a function of ionic strength.*

Dotted lines represent p_1H for $a_i=4$ (lower curve) and $a_i=6$ (upper curve).

TABLE 9. pH *at 25° C of solutions of* KHC_2O_4 (m) *and* $Na_2C_2O_4$ ($5m$) *on several scales*

m	pwH	p_1H		p_2H	p_3H	p_4H	p_5H	paH (glass electrode[a])
		$a_i=4$	$a_i=6$					
0.001	4.869	4.814	4.817	4.812	4.815	4.816	4.815	4.81
.002	4.830	4.757	4.763	4.758	4.760	4.760	4.760	4.77
.004	4.786	4.690	4.701	4.695	4.695	4.696	4.696	4.68
.005	4.771	4.666	4.679	4.673	4.673	4.674	4.673	4.67
.006	4.758	4.646	4.660	4.654	4.653	4.655	4.654	4.64
.008	4.737	4.613	4.630	4.625	4.621	4.624	4.622	4.59
.010	4.720	4.586	4.606	4.601	4.596	4.599	4.597	4.54
.015	4.688	4.536	4.561	4.558	4.548	4.553	4.550	4.54

[a] Calibrated at pH 4.01 with 0.05-m acid potassium phthalate.

m, is expressed with an average deviation of 0.00002 by

$$M/m=0.99707-0.1708m, \qquad (16)$$

when m is equal to or less than 0.015. Molality and molarity therefore differ by only 0.5 percent for the most concentrated of the buffer solutions whose paH is given in tables 10 and 11. Hence, the paH listed differs by less than 0.0008 from that for solutions of molarity numerically equal to the molality given at the head of each column, and the two scales of concentration can be used interchangeably below $m=0.015$.

TABLE 10. p_5H *of solutions of* KHC_2O_4 (m) *and* $Na_2C_2O_4$ $(5m)$ *from 0° to 50° C*

Temperature	Molality of potassium binoxalate							
	0.001	0.002	0.004	0.005	0.006	0.008	0.010	0.015
°C								
0	4.756	4.703	4.640	4.619	4.601	4.570	4.547	4.502
5	4.761	4.707	4.644	4.623	4.605	4.574	4.550	4.504
10	4.771	4.717	4.654	4.631	4.613	4.582	4.558	4.510
15	4.783	4.727	4.665	4.642	4.623	4.592	4.568	4.520
20	4.795	4.740	4.678	4.655	4.635	4.604	4.579	4.532
25	4.815	4.760	4.695	4.673	4.653	4.621	4.596	4.548
30	4.834	4.778	4.713	4.689	4.677	4.638	4.612	4.563
35	4.856	4.801	4.735	4.711	4.691	4.659	4.633	4.582
40	4.881	4.824	4.759	4.734	4.714	4.681	4.654	4.604
45	4.908	4.852	4.786	4.761	4.740	4.708	4.680	4.629
50	4.937	4.880	4.812	4.788	4.768	4.734	4.706	4.674

TABLE 11. p_5H *of solutions of* KHC_2O_4 (m) *and* $Na_2C_2O_4$ $(5m)$ *from 0° to 50° C*

Temperature	Molality of potassium binoxalate							
	0.001	0.002	0.004	0.005	0.006	0.008	0.010	0.015
°C								
0	4.756	4.703	4.640	4.619	4.600	4.570	4.546	4.501
5	4.761	4.707	4.644	4.623	4.605	4.574	4.550	4.504
10	4.771	4.717	4.654	4.631	4.613	4.582	4.558	4.511
15	4.783	4.727	4.665	4.642	4.623	4.592	4.568	4.521
20	4.795	4.740	4.678	4.655	4.635	4.604	4.580	4.533
25	4.815	4.760	4.696	4.673	4.654	4.622	4.597	4.550
30	4.834	4.778	4.714	4.690	4.678	4.639	4.613	4.564
35	4.856	4.801	4.736	4.712	4.692	4.660	4.635	4.585
40	4.881	4.824	4.760	4.735	4.715	4.683	4.656	4.607
45	4.908	4.852	4.787	4.762	4.742	4.710	4.683	4.633
50	4.937	4.880	4.813	4.790	4.770	4.736	4.709	4.658

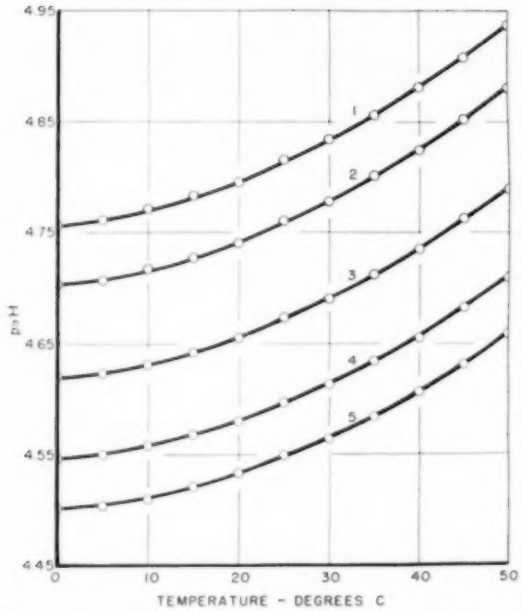

FIGURE 5. paH *of oxalate buffer solutions:* KHC_2O_4 (m), $Na_2C_2O_4$ ($5m$), *as a function of temperature.*

Curves 1 to 5 represent solutions for which m has the values 0.001, 0.002, 0.005, 0.01, and 0.015, respectively.

VI. References

[1] W. J. Hamer, G. D. Pinching, and S. F. Acree, J. Research NBS **36,** 47 (1946) RP1690.

[2] R. G. Bates and S. F. Acree, J. Research NBS **34,** 373 (1945) RP1648.

[3] H. S. Harned and R. W. Ehlers, J. Am. Chem. Soc. **55,** 2179 (1933).

[3] G. Calcagni, Gazz. chim. ital. **50,** [I], 245 (1920).

[5] Gmelins Handbuch der anorganischen Chemie, 8th ed., edited by E. Pietsch, p. K 937. (Verlag Chemie, Berlin, 1938).

[6] J. Koppel and M. Cahn, Z. anorg. Chem. **60,** 53 (1908).

[7] G. D. Pinching and R. G. Bates, J. Research NBS **37,** 311 (1946) RP1749.

[8] R. G. Bates and S. F. Acree, J. Research NBS **30,** 129 (1943) RP1524.

[9] W. J. Hamer, J. O. Burton, and S. F. Acree, J. Research NBS **24,** 269 (1940) RP1284.

[10] G. G. Manov, R. G. Bates, W. J. Hamer, and S. F. Acree, J. Am. Chem. Soc. **65,** 1765 (1943).

[11] E. Hückel, Physik. Z. **26,** 93 (1925).

[12] E. E. Chandler, J. Am. Chem. Soc. **30,** 694 (1908).

[13] C. Drucker, Z. physik. Chem. **96,** 381 (1920).

[14] H. T. S. Britton, J. Chem. Soc. **127,** 1896 (1925).

[15] H. M. Dawson and J. E. Smith, J. Chem. Soc. 2330 (1929).

[16] H. N. Parton and R. C. Gibbons, Trans. Faraday Soc. **35,** 542 (1939).

[17] H. S. Harned and L. D. Fallon, J. Am. Chem. Soc. **61,** 3111 (1939).

[18] L. S. Darken, J. Am. Chem. Soc. **63,** 1007 (1941).

[19] H. S. Harned and R. A. Robinson, Trans. Faraday Soc. **36,** 973 (1940).

[20] E. A. Guggenheim, J. Phys. Chem. **34,** 1758 (1930).

[21] D. I. Hitchcock, J. Am. Chem. Soc. **58,** 855 (1936); **59,** 2753 (1937).

[22] R. G. Bates, Chem. Rev. **42,** 1 (1948).

[23] R. G. Bates and E. R. Smith, J. Wash. Acad. Sci. **38,** 61 (1948).

[24] H. S. Harned and W. J. Hamer, J. Am. Chem. Soc. **55,** 2194 (1933).

[25] H. S. Harned, J. Am. Chem. Soc. **57,** 1865 (1935).

WASHINGTON, January 9, 1948.

U. S. Department of Commerce
National Bureau of Standards

Research Paper RP1886
Volume 40, May 1948

Part of the Journal of Research of the National Bureau of Standards

Pyrolytic Fractionation of Polystyrene in a High Vacuum and Mass Spectrometer Analysis of Some of the Fractions[1,2]

By Samuel L. Madorsky and Sidney Straus

Samples of polystyrene of an average molecular weight of about 230,000 and weighing 25 to 50 mg, were pyrolyzed in a vacuum of 10^{-6} mm of mercury at 350° to 420° C. Time of pyrolysis varied from 0.5 to 4 hours. The following fractions were obtained: (1) A solid residue having an average molecular weight of 2,182, (2) a wax-like fraction consisting of a mixture of a dimer, trimer, and tetramer of styrene, with an average molecular weight of 264, (3) a liquid fraction consisting of 94.3 mole percent of styrene, 5.6 mole percent of toluene, and traces of ethyl benzene and methyl styrene, (4) a gaseous fraction consisting mainly of carbon monoxide. Composition of all fractions and relative amounts of the wax-like and liquid fractions were found to be independent of time and temperature of pyrolysis, or of the amount of the original sample of polystyrene. A maximum yield of styrene, amounting to 42 weight percent of the original sample of polystyrene, was obtained at 420° C. The fact that only small fragments, not larger than the tetramer, were volatilized, leads to the conclusion that the larger fragments remain entangled in the mass of macromolecules and break up into smaller fragments, which then volatilize.

I. Introduction

Pyrolytic fragmentation and fractionation of polymers and identification of the fragments can serve as an effective means of studying structure and properties of the polymers under investigation. Pyrolysis of polymers results in fragments whose molecular weights and vapor pressures vary through a wide range. In order to facilitate the identification of these fragments, it is imperative to separate the mixture into fractions and apply suitable analytical methods to identify the various fractions. This paper describes a method and an apparatus for carrying out pyrolysis of polymers and fractionation of the products of pyrolysis under conditions of molecular distillation. Polystyrene was selected as the subject of this investigation because of the simplicity of its structure and the ease with which some of its fractions can be analyzed by means of the mass spectrometer.

Staudinger and Steinhofer[3] pyrolyzed 208 g samples of polystyrene in glass retorts by external heating and obtained a complex mixture of hydrocarbons. They used atmospheric pressure in one instance and a pressure of 0.1 mm of Hg in another. Fractional distillation of the products yielded a monomer, dimer, trimer, and some tetramer of styrene, and other compounds. They report that at atmospheric pressure and at a temperature of 400° to 500° C, rapid decomposition of polystyrene takes place resulting in the formation mostly of the monomer and some dimer. At 310° to 350° C and atmospheric pressure, slow decomposition takes place with the formation mostly of the monomer, a good deal of the dimer, and some trimer. At a pressure of 0.1 mm, where the fragments are more easily removed from the hot zone by distillation, the products of pyrolysis at 290° to 320° C are the monomer, dimer, trimer, and some tetramer.

However, thermal decomposition, when carried

[1] This paper was presented at the High Polymer Forum during the New York meeting of the American Chemical Society, Sept. 15 to 19, 1947.
[2] This paper is also appearing in the May issue of Industrial and Engineering Chemistry.

[3] H. Staudinger and A. Steinhofer, Ann. 517, 35 (1935).

781956—48——6

out in a high vacuum, could be interpreted more easily for the following reasons: The products of pyrolysis remain free from admixtures from the atmosphere; fractions of higher molecular weight could be distilled off without secondary pyrolysis; and separation of the products of pyrolysis into fractions could be carried out most effectively under conditions of molecular distillation.

The method was investigated in a series of experiments using temperature, time, and size of sample as variables. In each case, a weighed amount, 25 to 50 mg, of pure polystyrene, of an average molecular weight of about 230,000,[4] was spread as a thin layer in a platinum tray having an evaporating surface of about 12 cm^2. The tray was then heated in a vacuum of about 10^{-6} mm of Hg for periods of time ranging from 0.5 to 4 hr and at temperatures varying between 350° and 420° C. The distillate was first collected on a liquid-air cooled condenser placed at a distance of 1.7 cm from the evaporating surface, then separated into fractions by redistillation and the fractions weighed. All the weighings were made on a microbalance to an accuracy of about 0.05 mg.

[4] Molecular weight determination was made by Samuel G. Weissberg of the National Bureau of Standards, by the osmotic pressure method.

II. Apparatus and Experimental Procedure

The apparatus is shown diagrammatically in figure 1. It is made of glass and resembles a Dewar flask except for a ground joint at the upper end for the purpose of introducing or removing the platinum tray from the apparatus. The tray is heated by means of a platinum-wire heating element incased in the form of a fine helix in short lengths of glass tubing and held together between two stainless steel disks. An oil pump and a Hg diffusion pump, not shown in the figure, serve to evacuate the system to a sticking vacuum, preliminary to pyrolysis. Another Hg diffusion pump

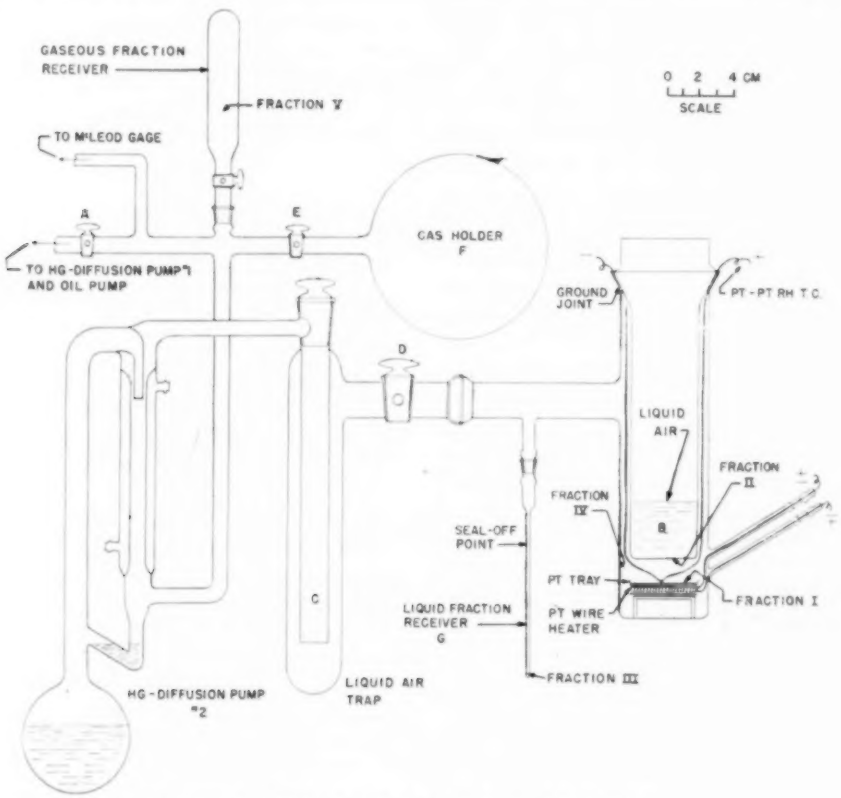

FIGURE 1. *Molecular still for pyrolysis of high polymers.*

capable of operating against a pressure of several centimeters of Hg, serves to collect the gaseous fraction during pyrolysis. Difficulties due to desorption of gases from the heater and the inner surface of the outer jacket in the hot zone were overcome by a preliminary heat treatment of the apparatus. This treatment consisted in maintaining the heater and tray at about 200° C for 1½ hr, and at the same time flaming gently the outer jacket. After this preliminary heating, the outer jacket was kept cool during pyrolysis of the sample by means of a water-cooled coiled tube surrounding the jacket. A blank experiment, without polystyrene in the tray, showed that by following such a procedure the total amount of air desorbed in 1 hr of heating from 200° to 400° C, followed by 1 hr of heating at 400° C, was 0.007 ml at normal temperature and pressure. Temperature of pyrolysis was measured by means of a Pt-PtRh thermocouple spotwelded to the tray at its center.

The following procedure was employed. A sample of polystyrene,[5] in the form of a 0.5 percent solution in benzene, was placed in the platinum tray, and the benzene evaporated at 100° to 110° C, followed by evacuation for about 1 hr to a constant weight. The tray was then placed on the heater in the apparatus and the pressure reduced to a sticking vacuum. After a preliminary heating at 200° C, as described above, the system was shut off from the oil pump and Hg diffusion pump 1 by means of stopcock *A*. Liquid air was then placed in the inner cup *B* of the Dewar-like apparatus, also around the liquid-air trap *C*, and Hg diffusion pump 2 was turned on. Temperature of the tray was then raised to the required point and then kept constant for the required time. All the products of pyrolysis, except those not condensable at the temperature of liquid air, collected on the liquid-air condenser *B*. A gaseous fraction V, not condensable at the temperature of liquid air, was collected in the space between the Hg diffusion pump 2 and stopcocks *A* and *E*. At the end of pyrolytic operation, stopcock *D* was closed, diffusion pump 2 turned off and the gas allowed to expand to stopcock *D*. The volume between stopcocks *A*, *E*, and *D*, as calibrated by means of the gas holder *F*, was about 2 liters. Pressure was measured by means of a McLeod gage not shown in the figure. A sample of gas in the receiver was used for analysis in the mass spectrometer. The weight of the gaseous fraction could then be determined from a knowledge of its volume, pressure, and composition.

To separate the other fractions, the liquid air was removed from condenser *B*, and a liquid air container placed under liquid fraction receiver *G*. Fraction III, volatile at room temperature, was thus collected in the small receiving tube *G*. This tube was then sealed without melting it off and later weighed. Instead of collecting only one fraction III, it would be possible to collect fractions III_a, III_b, etc., by maintaining the condenser *B* at various temperatures between that of liquid air and room temperature.

Part of the condensate on *B*, volatile at the temperature of pyrolysis but nonvolatile at room temperature, was collected as fraction II by dissolving it in benzene in a platinum crucible, vaporizing the benzene, and weighing the residue. The residue in the tray itself was weighed as fraction I.

Evaporation from a liquid or solid surface into a vacuum follows Lambert's cosine law, and, therefore, a part of the products of pyrolysis failed to condense on *B* and deposited on the inner wall of the outer jacket in the neighborhood of the platinum tray. As the jacket was maintained at the temperature of tap water during pyrolysis, that part of the deposit on its wall that was volatile at room temperature, reevaporated and condensed on the liquid-air condenser *B*. The nonvolatile residue on the jacket, designated as fraction IV, was not collected, and its weight is assumed to be equal to the difference obtained by subtracting the sum of the weights of fractions I, II, III, and V from the weight of polystyrene used. It is safe to assume that fraction IV has approximately the same composition as fraction II.

III. Pyrolytic Fractionation of Polystyrene

Results of 20 fractionation experiments are shown in table 1. In experiments 1 to 14, inclusive, temperature of pyrolysis was varied from 350° to 420° C, and the duration of each experiment was 0.5 hr. Pyrolysis of polystyrene, according to these data, begins at about 350° C and is practically complete at 400° C. In experiments 3, 5, 6, 12, and 13, the amount of sample used was about twice as much as in the other

[5] We are indebted to Arthur Roche, Dow Chemical Co., for this polystyrene. It was prepared by polymerizing pure styrene, without a catalyst, in an atmosphere of nitrogen, for 48 hours at 120° C.

TABLE 1. *Pyrolytic fractionation of polystyrene*

Experiment number	Weight of sample	Temperature	Duration	In weight percent of original sample				
				I	II	III	IV	V
				Residue	Nonvolatile at room temperature	Volatile at room temperature	On wall of apparatus	Gaseous fraction
	mg	*°C*	*hr*					
1	25.50	350	0.5	95.76	3.41	0.20	0.53	0.10
2	23.91	350	.5	96.36	1.76	1.04	0.77	.07
3	48.33	361	.5	86.44	3.50	4.68	5.31	.07
4	24.66	379	.5	52.80	14.36	23.56	9.17	.11
5	40.56	387	.5	50.86	17.08	22.85	9.04	.17
6	47.85	390	.5	41.19	20.83	27.06	10.81	.11
7	23.98	397.5	.5	8.92	30.90	41.82	18.20	.16
8	24.16	400	.5	2.56	32.78	43.58	20.72	.16
9	23.32	400	.5	11.53	31.64	38.84	17.86	.13
10	25.52	400	.5	5.25	37.34	40.32	16.96	.13
11	24.86	401	.5	5.27	31.94	42.72	19.84	.13
12	56.88	401	.5	0.04	34.48	36.41	29.00	.07
13	55.15	405	.5	1.67	35.71	36.80	25.77	.05
14	21.73	420	.5	0.83	34.01	44.59	20.45	.12
15	47.69	361	1.0	77.88	8.62	9.29	4.11	.10
16	48.54	361	2.0	59.35	16.30	16.75	7.45	.15
17	63.22	364	3.0	21.53	35.25	30.61	12.53	.08
18	48.55	364	4.0	8.36	29.22	33.63	18.71	.06
19	54.79	376	1.0	19.64	32.62	26.19	21.51	.04
20	56.85	378	1.0	14.08	34.53	37.70	13.65	.04

experiments of this series. In experiments 3, 15, and 16 the temperature was the same 361° C, and the time was varied from 0.5 to 2 hr. In experiments 17 and 18 the temperature was the same, 364° C, and the time was 3 and 4 hr, respectively. Fractions I to V are listed in table 1. In general, gradual decrease of fraction I and a gradual increase of fraction III, II, and IV with temperature and time, are indicated in this table. As to the gaseous fraction V, it is about the same in all experiments, the average being 0.10 percent by weight of the sample of polystyrene used.

In table 2, fractions II and IV for each experiment are shown combined as one fraction, nonvolatile at room temperature. Ratios of volatile fraction (III) to the nonvolatile fraction (II+IV) are shown in the last column of this table. With a few exceptions, this ratio is about the same for all experiments, the average for experiments 3 to 20, inclusive, being 0.74. Staudinger and Steinhofer obtained in one experiment, carried out at a pressure of 0.1 mm and a temperature of 290° to 320° C, a ratio of 0.83.

In figure 2, fractions I (residues), fractions II+IV (nonvolatile at room temperature), and

TABLE 2. *Ratio of volatile (III) to nonvolatile (II+IV) fraction in the pyrolysis of polystyrene*

Experiment number	Temperature	Time	III volatile at room temperature	II+IV nonvolatile at room temperature	Ratio III/II+IV
	°C	*hr*	*Percent*	*Percent*	
1	350	0.5	0.20	3.94	0.05
2	350	.5	1.04	2.53	.41
3	361	.5	4.68	8.81	.53
4	379	.5	23.56	23.53	1.00
5	387	.5	22.85	26.12	.87
6	390	.5	27.06	31.64	.85
7	397.5	.5	41.82	49.10	.85
8	400	.5	43.58	53.50	.82
9	400	.5	38.84	49.50	.78
10	400	.5	40.32	54.30	.74
11	401	.5	42.72	51.78	.82
12	401	.5	36.41	63.48	.57
13	405	.5	36.80	61.48	.60
14	420	.5	44.59	54.46	.82
15	361	1	9.29	12.73	.73
16	361	2	16.75	23.75	.71
17	364	3	30.61	47.78	.64
18	364	4	33.63	47.93	.70
19	376	1	26.19	54.13	.48
20	378	1	37.70	48.18	.78
Average ratio for experiments 3 to 20 incl					0.74
Staudinger and Steinhofer					.83

fractions III (volatile at room temperature), are plotted in weight percent of original samples of polystrene against temperature of pyroly s. Only experiments 1 to 14, inclusive, where the time of pyrolysis was the same, 0.5 hr., are shown in this figure.

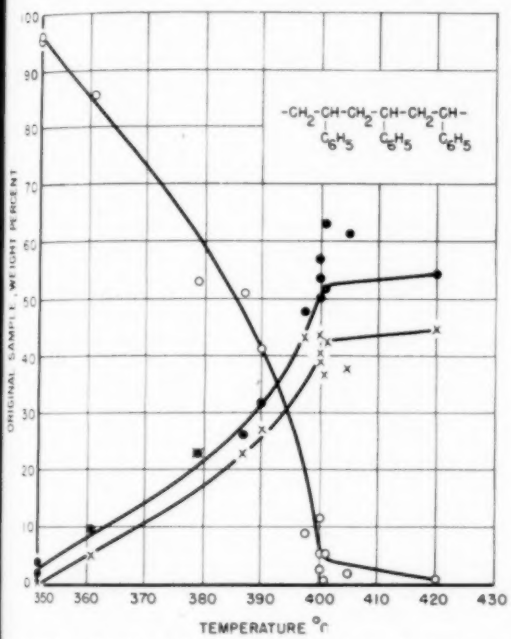

FIGURE 2. *Fractions obtained in the pyrolysis of polystyrene.*

○, Residue; ●, nonvolatile at room temperature; X, volatile at room temperature.

IV. Analysis of Fractions

Only the gaseous fraction (V) and the fraction volatile at room temperature (III), could be analyzed in the Consolidated mass spectrometer used in this work. Fraction V was found to consist chiefly of CO. The CO was probably due to the reaction of polystyrene with oxygen held in the original polystyrene in dissolved or combined form. Weight of the gaseous fraction was determined in each case from its volume, pressure, and mass spectrometer analysis. It amounted, on the average, to 0.1 percent of the original weight of polystyrene.

Fraction III was collected as a clear colorless liquid in a small tube, about 1.7-mm inside diameter and 7 cm long. Its weight was determined by weighing the tube before and after the experiment, allowing for the air removed in the evacuation. This fraction weighed anywhere between a fraction of a milligram and 20 mg. As the expansion chamber of the mass spectrometer could hold only a few milligrams of this fraction in gaseous form at the vapor pressure of the components of this fraction, it was found necessary to use a special expansion apparatus in preparing a sample for analysis. This expansion apparatus is shown in figure 3. It consists of a chamber that can be

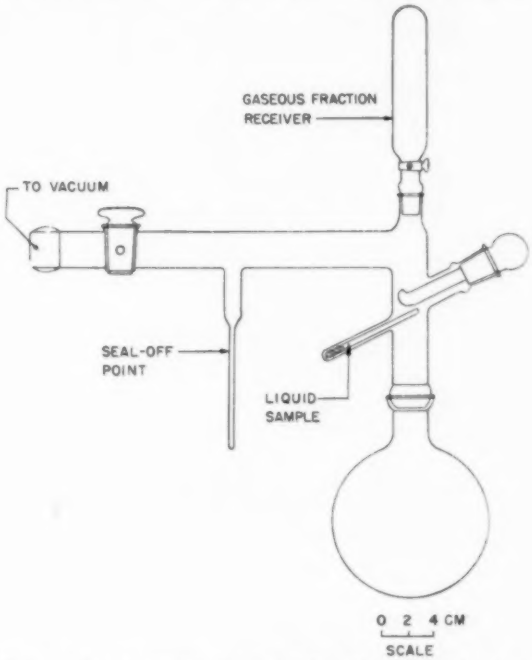

FIGURE 3. *Apparatus for expanding liquid samples in a vacuum.*

evacuated to a sticking vacuum. The volume of this chamber could be varied to suit the size of fraction III, by means of a removable bulb varying in size from 25 to 500 ml. The apparatus is provided with a break-off valve and a sample tube in which a gaseous sample was collected for analysis in the mass spectrometer. After collecting the sample, the rest of the expanded material was collected in a small tube by means of liquid air and the tube sealed off. Fragments of the broken tube that held fraction III were collected and weighed before and after washing thoroughly with benzene to see whether it contained a nonexpanded residue. The residue varied from zero to a few percent of the total weight of fraction III.

The Consolidated mass spectrometer has a range of analysis of molecular weight up to about 130 to 150. This range includes the monomer, styrene, and other fragments having one benzene ring. If fraction III contained any fragments with more than one benzene ring, say, a dimer, these fragments would not show up in the mass spectrometer analysis. In order to check on this, two sample tubes containing fraction III from experiments 5 and 6, were broken in the open air and the contents allowed to expand at room temperature. Figure 4 shows loss of weight in percent of original weight of fraction III plotted against time in days. In both cases expansion leveled off at 95.5 percent loss, indicating that fraction III contained 4.5 percent in polymerized form. Sample 6 expanded more slowly because the tube in which it was contained was bent sharply in the form of a U. The fact that styrene polymerizes slowly even at room temperature was confirmed by a molecular weight determination of fraction III by the method of freezing point lowering in cyclohexane. The molecular weight varied from about 100 to 114, depending on age of fraction.

Results of mass spectrometer analysis of fraction III are shown in the case of nine experiments in table 3. Relative composition of this fraction seems to be independent of the original amount of polystyrene used or of duration or temperature of pyrolysis. The results are given in mole percent and indicate that this fraction consists on the average of 94.3 percent of styrene, 5.6 percent of toluene, and traces of ethyl benzene and methyl styrene. Styrene yield in weight percent of the original weight of polystyrene used is also shown in this table. At 400° C, the average yield of styrene (in experiments 7, 9, and 10) is 36.8 percent.

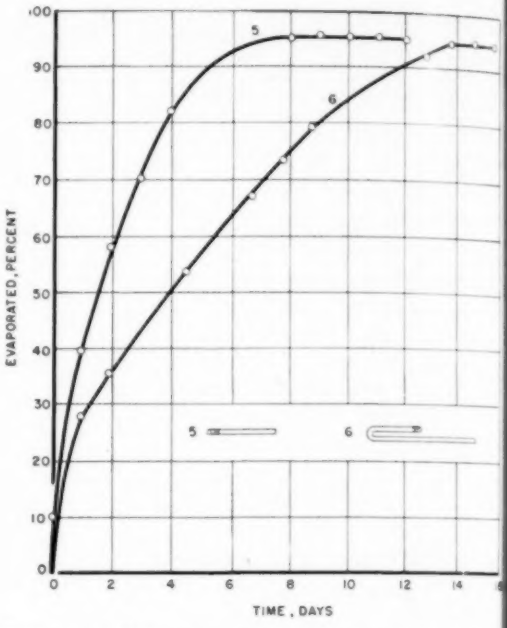

FIGURE 4. *Evaporation at atmospheric pressure and room temperature of the liquid fraction from pyrolysis of polystyrene.*

Fraction I is a light-brown horny solid and fraction II a tan-colored wax-like material. These fractions, being nonvolatile at room temperature, could not be analyzed in the mass spectrometer. The average molecular weight of these fractions

TABLE 3. *Mass spectrometer analysis of fraction III, volatile at room temperature*

Experiment number	Weight of sample	Time	Temperature	Styrene (yield in percent of sample)	Fraction III			
					Styrene	Toluene	Ethyl benzene	Methyl styrene
	mg	*hr*	*° C*		*Mole %*	*Mole %*	*Mole %*	*Mole %*
2	23.91	0.5	350	0.96	91.8	8.0	0.1	0.1
15	47.69	1.0	361	8.56	92.2	7.8	0	0
16	48.54	2.0	361	15.88	94.1	5.9	0	0
17	63.22	3.0	364	29.63	96.1	3.9	0	0.04
18	48.55	4.0	364	31.85	94.0	6.0	0	.02
4	24.66	0.5	379	22.67	95.5	4.4	0.06	.03
7	23.98	.5	397.5	40.32	95.7	4.2	.06	0
9	23.32	.5	400	37.00	94.7	5.2	.1	0
10	25.52	.5	400	38.58	95.0	5.0	0	0
Average values					94.3	5.6		

was determined with a Beckman thermometer by the method of freezing point lowering in a solution of cyclohexane. In case of fraction II, the freezing point lowering was about 2° to 2.5° C. and in the case of fraction I, the lowering was about 0.2° C. The molecular weight was calculated by means of formula

$$M=\frac{F\times 1{,}000\times w}{\Delta F\times W},$$

where

F = molar freezing point lowering; 20° C. for cyclohexane
w = weight of solute in g
W = weight of solvent in g
ΔF = actual freezing point lowering.

The results are shown in table 4.

TABLE 4. *Average molecular weight of fractions I and II by the method of freezing point lowering in cyclohexane*

Experiment number	Temperature	Time	Average molecular weight	
			Fraction I	Fraction II
	°C.	hr.		
15	361	1	.....	266
16	361	2	.....	263
17	364	3	2,078	265
19	376	1	2,214	261
20	378	1	2,255	259
12	401	0.5	.....	266
13	405	.5	.....	266
	.....	.....	2,182±70	264±2
Staudinger and Steinhofer	.....	.....	.....	263

The average molecular weight of fraction I, based on three determinations, is 2,182±70. For fraction II, the average of seven determinations is 264±2. If fraction II were to consist of equal amounts of the dimer, molecular weight 208, and trimer, molecular weight 312, the average molecular weight would be 250. A slight preponderance of the trimer, or the presence of a small amount of the tetramer, molecular weight 416, or both, could account for the actual average molecular weight of 264. Staudinger and Steinhofer pyrolyzed a 208-g sample of polystyrene at a pressure of 0.1 mm and temperature of 290° to 320° C and obtained, in addition to styrene, 19.32 percent of dimer, 23.08 percent of trimer, and 3.85 percent of tetramer. The average molecular weight of a mixture of dimer, trimer, and tetramer in the above proportions is 263.

V. Discussion of Results

Pyrolysis of polystyrene was carried out in this work under most favorable conditions of molecular distillation, where fragments of high molecular weight, if formed, would have a chance to escape into the gaseous phase and collect on the condenser. The fact that the condensate consisted of small fragments, i. e., the monomer, dimer, trimer, and perhaps some tetramer, indicates that we are not dealing here with a simple case of molecular distillation, but that distillation here is subservient to conditions of pyrolytic decomposition.

Let us first consider rate of pyrolysis as compared with rate of vaporization of the fragments. It took about 30 minutes to pyrolyze 25 to 50 mg of polystyrene at 400° C. Rate of vaporization of a similar amount of material, under conditions of molecular distillation can be calculated by means of Langmuir's equation [6] for evaporation from a liquid or solid surface:

$$m=P\sqrt{\frac{M}{2\pi RT}}, \text{ where}$$

m = grams of material evaporated per square centimeter of surface per second.
P = vapor pressure in dynes per square centimeter.
M = molecular weight of the material.
R = gas constant in ergs per degree C.
T = absolute temperature.

The vapor pressure of a mixture of the monomer, dimer, trimer, and tetramer in contact with polystyrene, is not known, but it can safely be assumed to be at least 50 mm at, say, 350° to 400° C. Molecular weight of the mixture will be assumed as 200. Then, since total evaporating surface is 12 cm², we have

$$m=50\times 1333.22\times 12\times\sqrt{\frac{200}{2\pi\times 8.3\times 10^7\times 623}}=20\ g.$$

per second. Thus it would take a small fraction of a second to vaporize 25 to 50 mg of material involved in the pyrolysis.

In the work of Staudinger and Steinhofer, external pressure of 1 atmosphere was used in one

[6] I. Langmuir, Phys. Rev. **2**, 329 (1913).

case and of 0.1 mm Hg in another. In either case, the pressures were too high for molecular distillation and it might be expected that large fragments would be returned to the hot zone by kinetic agitation and be pyrolyzed further into smaller fragments. However, in our case, where the external pressure was 10^{-6} mm of Hg fragments greater than the trimer or tetramer, once formed, would have a vapor pressure sufficient to remove it from the hot zone and bring it to the condenser. It is, therefore, surprising that the fragments collected in our work were no greater than those obtained by Staudinger and Steinhofer in their pyrolysis at a pressure of 0.1 mm Hg. In fact, there is a close agreement between our results and those of Staudinger and Steinhofer carried out at 0.1 mm pressure, as shown in table 5. In this table two experiments of Staudinger and Steinhofer, (1), at atmospheric pressure and (2) at 0.1 mm, are compared with our experiments 7, 9, and 10. In experiments (1) the amounts of monomer, dimer, and trimer collected were 62.5, 19.32, and 3.85 percent, respectively, of the original weight of polystyrene used. In experiment (2), the fractions collected were a monomer, dimer, trimer, and tetramer in amounts of 38.46, 19.32, 23.08, and 3.85 percent, respectively. Total of the dimer, trimer, and tetramer in the latter case was 46.15 percent. In the case of the present work, the averages for experiments 7, 9, and 10, were 40.32 percent for the monomer and 50.97 percent for the sum of the dimer, trimer, and tetramer. In addition to this, the average molecular weight of fraction II of our work is 264 as compared with the mean molecular weight of 263 for the dimer, trimer, and tetramer in experiment (2) of Staudinger and Steinhofer.

The fact that only small fragments, no larger than the tetramer were obtained in the present work, in spite of the favorable conditions for

TABLE 5. *Pyrolytic fractionation of polystyrene*

Experimental conditions	Staudinger and Steinhofer		Present work for experiment—			Average for experiments 7, 9, 10
			7	9	10	
Weight of sample, g	208	208	0.02398	0.02332	0.02552	
Pressure, mm Hg	760	10^{-1}	10^{-6}	10^{-6}	10^{-6}	
Temperature, °C	310 to 350	280 to 320	397.5	400	400	
Duration, hr	6	12	0.5	0.5	0.5	
GASEOUS FRACTION (V)						
Component	In weight percent of original sample					
CO			0.16	0.13	0.13	0.14
FRACTION VOLATILE AT ROOM TEMPERATURE (III)						
Styrene	62.5	38.46	40.32	37.00	38.58	38.64
Ethyl benzene			0.02	0.04	0.00	0.02
Toluene			1.48	1.80	1.74	1.68
Total	62.5	38.46	41.82	38.84	40.32	40.34
FRACTION NONVOLATILE AT ROOM TEMPERATURE (II+IV)						
Dimer	19.32	19.32				
Trimer	3.85	23.08				
Tetramer	0	3.85				
Total	23.17	46.25	49.10	49.50	54.40	50.97
FRACTION (I)						
Residue	9.62	11.54	8.92	11.53	5.25	8.57

molecular distillation, is in qualitative agreement with the view expressed by Frenkel,[7] who states that: Linear or chain-like macromolecules cannot exist in the gas phase, for, instead of evaporating, they must be disintegrated or depolymerized into smaller units, mainly monomeric or dimeric. Frenkel further points out that the vapor phase will consist of fragments in which the number of units is equal to W_1/U_1, where W_1 is dissociation energy and U_1 is evaporation energy of the monomer. In the case of polystyrene, W_1, the energy required to rupture a C to C bond, is approximately 80 kcal, and U_1, latent heat of vaporization of styrene, is about 9 kcal. Therefore, $W_1/U_1 = 80/9 = 9$. Since the polystyrene chain has a uniform structure throughout its length (except for the ends), fragments from a monomer to a nonamer should be equally possible. The average molecular weight of the mixture of all the fragments, except the monomer, should, therefore, be much higher than 264. The fact that the average molecular weight of fraction II was only 264 could be explained by assuming that larger fragments split off along with the smaller fragments, but that the former remain entangled in the macromolecules and split further into smaller fragments. This assumption could explain the fact that pyrolysis of polystrene is a slow process.

VI. Summary

Pyrolysis of small samples of polystyrene, of molecular weight of about 230,000, was carried out in a vacuum of 10^{-6} mm of Hg and at temperatures between 350° and 420° C. Time of pyrolysis was varied from 0.5 to 4 hr. Results indicate that pyrolysis begins at about 350° C and is almost complete at 400° C. The volatile products of pyrolysis were separated into one gaseous fraction, one liquid fraction, volatile at room temperature, one wax-like fraction, nonvolatile at room temperature, and a horny-like residue. The gaseous fraction amounted on the average to 0.1 percent by weight of the original sample of polystyrene and consisted chiefly of CO. The liquid fraction consisted of 94.3 mole percent of styrene and 5.6 mole percent of toluene. The wax-like fraction consisted of a mixture of dimer, trimer, and some tetramer, with an average molecular weight of 264 ± 2. A hard tan-colored residue, which was obtained in the experiments at lower temperatures, was found to have an average molecular weight of $2{,}182 \pm 70$. Weight ratio of the liquid fraction to the wax-like fraction in all the experiments above 350° C is close to a constant, independent of amount of original polystyrene used, of duration or temperature of pyrolysis. Composition of each fraction is also independent of these variables. Maximum yield of styrene was obtained at 420° C and amounted to 42 percent by weight of the original polystyrene. A comparison of this work, which was carried out under most favorable conditions of molecular distillation, with the work of Staudinger and Steinhofer, who pyrolyzed a 208-g sample of polystyrene at a pressure of 0.1 mm Hg and at a temperature of 290° to 320° C, shows a remarkable similarity of results.

The authors wish to thank Robert M. Reese, who made the mass spectrometric analyses, and Dorothy Thompson and Laura Williamson, who made the computations of these analyses in connection with this work.

Washington, September 5, 1947.

[7] Frenkel, Kinetic theory of liquids, p. 451 (Oxford at the Clarendon Press, 1946).